

Electronic Theses and Dissertations, 2020-

2021

Multi-functional Fluorescence Microscopy via PSF Engineering for High-throughput Super-resolution Imaging

Jinhan Ren
University of Central Florida

 Part of the [Electromagnetics and Photonics Commons](#), and the [Optics Commons](#)
Find similar works at: <https://stars.library.ucf.edu/etd2020>
University of Central Florida Libraries <http://library.ucf.edu>

This Doctoral Dissertation (Open Access) is brought to you for free and open access by STARS. It has been accepted for inclusion in Electronic Theses and Dissertations, 2020- by an authorized administrator of STARS. For more information, please contact STARS@ucf.edu.

STARS Citation

Ren, Jinhan, "Multi-functional Fluorescence Microscopy via PSF Engineering for High-throughput Super-resolution Imaging" (2021). *Electronic Theses and Dissertations, 2020-*. 748.
<https://stars.library.ucf.edu/etd2020/748>

MULTI-FUNCTIONAL FLUORESCENCE MICROSCOPY VIA PSF
ENGINEERING FOR HIGH-THROUGHPUT SUPER-RESOLUTION
IMAGING

by

JINHAN REN

B.S. Harbin Institute of Technology, 2012

M.S. Harbin Institute of Technology, 2014

A dissertation submitted in partial fulfilment of the requirements
for the degree of Doctor of Philosophy
in the College of Optics and Photonics
at the University of Central Florida
Orlando, Florida

Summer Term
2021

Major Professor: Kyu Young Han

© 2021 Jinhan Ren

ABSTRACT

Image-based single cell analysis is essential to study gene expression levels and subcellular functions with preserving the native spatial locations of biomolecules. However, its low throughput has prevented its wide use to fundamental biology and biomedical applications which require large cellular populations in a rapid and efficient fashion. Here, we report a 2.5D microcopy (2.5DM) that significantly improves the image acquisition rate while maintaining high-resolution and single molecule sensitivity. Unlike serial z-scanning in conventional approaches, volumetric information is simultaneously projected onto a 2D image plane in a single shot by engineering the fluorescence light using a novel phase pattern. The imaging depth can be flexibly adjusted and multiple fluorescent markers can be readily visualized. We further enhance the transmission efficiency of 2.5DM by ~ 2 -fold via configuring the spatial light modulator used for the phase modulation in a polarization-insensitive manner. Our approach provides a uniform focal response within a specific imaging depth, allowing to perform quantitative high-throughput single-molecule RNA measurements for mammalian cells over a $2 \times 2 \text{ mm}^2$ region within an imaging depth of $\sim 5 \text{ }\mu\text{m}$ in less than 10 min and immunofluorescence imaging at a volumetric imaging rate of $>30 \text{ Hz}$ with significantly reduced light exposure. With implementation of an adaptive element, our microscope provides an extra degree of freedom in correcting aberrations induced by specimens and optical components, showing its capability of imaging thick specimens with high-fidelity of preserving volumetric information with fast imaging speed. We also demonstrate multimodal imaging that can be switched from 2.5DM to a 3D single-molecule localization imaging platform by encoding the depth information of each emitter into the shape of point spread function, which

enables us to obtain a resolution of <50 nm. Our microscope offers multi-functional capability from fast volumetric high-throughput imaging, multi-color imaging to super-resolution imaging.

Key words: fluorescence microscopy; high-throughput; extended depth of field; adaptive optics; super-resolution

ACKNOWLEDGEMENTS

During my PhD program, I have received a lot of support and assistance. First and foremost, I would like to thank my supervisor, Prof. Kyu Young Han, who was always supportive and gave invaluable advice for my research. I am extremely grateful that you provided me such a great opportunity to join this lab and to continuously gain knowledge and experience from you. You are not only a great mentor but also a great colleague and friend. I cannot appreciate more about your patience to listen to any problem I had in the research and always gave valuable suggestions. I would also like to acknowledge my committee, Prof. Shintson Wu, Prof. Aristide Dogariu and Prof. Yoon-Seong Kim for their valuable advices through my thesis. In addition, I would like to thank all the members from our lab: Dr. Jialei Tang, Ben Croop, Chun Hung Weng, Vahid Ebrahimi and Dr. Chenyi Zhang. They are always kind and generous to help. I enjoyed every moment to work with them in the same lab. Finally, I would like to thank my parents and my brother from the bottom of my heart. Without their warmest love and support, it would be impossible to go through every good/bad moment in the past few years. Besides, I would also like to thank my friend, Guanzhi Wang, who provided a lot of encouragement and relaxed experience outside my research.

TABLE OF CONTENTS

LIST OF FIGURES	ix
LIST OF ACRONYMS (or) ABBREBIATIONS	xii
CHAPTER 1 INTRODUCTION	1
CHAPTER 2 PRINCIPLE OF 2.5DM.....	10
2.1 Vectorial Diffraction Theory.....	10
2.2 Design of 2.5D Phase Pattern.....	13
2.3 Characterization of 2.5DM by Simulation	18
2.3.1 Comparison with Other PSF Engineering Methods.....	18
2.3.2 Tunability of Imaging Depth	20
2.3.3 Focal Response to Broadband Light	23
CHAPTER 3 HIGH-THROUGHPUT IMAGING BY 2.5DM	25
3.1 Overview	25
3.2 Experimental Characterization of 2.5DM	28
3.3 Application of 2.5DM to smFISH.....	35
3.3.1 Quantitative Imaging of mRNAs in Mammalian Cells by 2.5DM.....	36
3.3.2 High-throughput smFISH Imaging by 2.5DM.....	45
3.3.3 Multi-color smFISH Imaging by 2.5DM.....	50
3.4 Immunofluorescence Imaging by 2.5DM	54
CHAPTER 4 2.5DM WITH IMPROVED DETECTION EFFICIENCY AND DEPTH ABERRATION CORRECTION	62
4.1 Overview	62

4.2 Polarization-insensitive 2.5DM.....	65
4.2.1 Microscope Design	65
4.2.2 Minimizing Off-axis Aberration	66
4.2.3 PSF Measurement	69
4.2.4 smFISH Imaging.....	71
4.3 Depth Aberration Correction.....	73
4.3.1 Characterization of Depth Aberration by Simulation	74
4.3.2 Characterization of Depth Aberration by Experiments	75
4.3.3 Fluorescent Labeled Collagen Imaging	79
CHAPTER 5 3D SUPER-RESOLUTION IMAGING BY SINGLE-MOLECULE	
LOCALIZATION	84
5.1 Overview	84
5.2 Methods for 3D Localization via PSF Engineering	87
5.3 dSTORM Imaging using DH-PSF	89
5.3.1 Calibration of Imaging System by DH-PSF	89
5.3.2 Localization Precision of Single Molecules	91
5.3.3 3D Super-resolution Imaging in Mammalian Cells	94
CHAPTER 6 CONCLUSION.....	96
APPENDIX A: METHODS	99
APPENDIX B: MATLAB SCRIPT	104
LIST OF REFERENCES	108

LIST OF FIGURES

Figure 1 Four different approaches to volumetric imaging.	3
Figure 2 Schematic of a simplified imaging system.	10
Figure 3 Working principle of 2.5DM by simulation.	15
Figure 4 Focal responses by scalar and vectorial diffraction theory for 2.5D imaging.	17
Figure 5 Comparison of focal responses by 2.5D phase pattern and cubic phase pattern.	18
Figure 6 Focal responses by multi-annular mask, 2.5D phase pattern without/with dithering. ...	20
Figure 7 Tunable depth of field generated by controlling the spherical aberration strength.	21
Figure 8 Log-log plot of FWHM of the axial PSF (Δz) as a function of the lateral PSF (Δx)	22
Figure 9 Response of 2.5D image to the broadband light.	23
Figure 10 Volumetric imaging in a conventional microscopy and 2.5DM.	26
Figure 11 Experimental scheme of 2.5D microscopy.	30
Figure 12 PSF measurements using 80 nm gold nanoparticles.	31
Figure 13 PSF measurement using 200 nm fluorescent beads.	32
Figure 14 Experimental characterization of a low NA imaging system.	33
Figure 15 Single-molecule fluorescence intensity measurements.	34
Figure 16 Schematic of mRNA with multiple probes labeled with fluorescent dyes.	36
Figure 17 Single molecule mRNA FISH imaging of <i>EEF2</i> on U2OS cells using 2.5DM.	41
Figure 18 Co-localization of smFISH spots obtained by two methods.	42
Figure 19 Quantification of mRNAs by 2.5DM and WF given the same exposure time.	43
Figure 20 smFISH images of <i>TOP2A</i> labeled with AF647 on U2OS cells.	44
Figure 21 High-throughput smFISH imaging.	45

Figure 22 Copy number per cell as a function of nuclear size.....	47
Figure 23 Scheme of highly multiplexed error-robust FISH (MERFISH) approach.	50
Figure 24 Focal responses of 2.5DM under two distinct wavelengths.	51
Figure 25 3D hydrogel fluorescence beads images with the peak emission wavelength 605 nm.	53
Figure 26 Two color smFISH imaging on <i>EEF2</i> and <i>TOP2A</i> on U2OS cells.....	54
Figure 27 Immunofluorescence imaging of vimentin by 2.5DM.	56
Figure 28 Post-processing of 2.5D image based on SRRF.....	58
Figure 29 Immunofluorescence imaging of microtubules labeled with AF488 by 2.5DM.....	59
Figure 30 Measurement of the photobleaching effect on 2.5DM and WF.	60
Figure 31 Schematics of two polarization non-sensitive SLMs.	63
Figure 32 Microscope design with improved transmission efficiency.	67
Figure 33 Characterization of fluorescence light divergence in the detection path.....	68
Figure 34 Focal responses of WF before and after off-axis aberration correction.	69
Figure 35 PSF measurements using 200-nm fluorescent beads.....	70
Figure 36 Single-molecule FISH images of <i>EEF2</i> on U2OS cells by double-pass 2.5DM.	72
Figure 37 Ray trace of a point source through a lens	73
Figure 38 Simulation of focal responses by WF with depth aberration induced.....	74
Figure 39 Simulation of focal responses by 2.5D phase with depth aberration induced.....	75
Figure 40 Measurement of depth aberrations by WF using 3D fluorescent beads.	77
Figure 41 Measurement of depth aberrations by 2.5DM using 3D fluorescent beads.	78
Figure 42 Fluorescent-labeled collagen images by 2.5DM with depth aberration correction.....	80
Figure 43 Focal responses of 2.5DM with depth aberration correction at the middle z-position.	81

Figure 44 Schematic of Epi- and highly inclined swept tile illumination.	82
Figure 45 Super-resolution microscopies categorized in three mechanisms.	86
Figure 46 3D SMLM by PSF engineering.	88
Figure 47 Calibration of DH-PSF imaging system.	90
Figure 48 Focal responses of DH-PSFs at different axial positions with varying spiral zones....	91
Figure 49 Experimental characterization of 3D localization precision for single fluorophore. ...	93
Figure 50 3D <i>d</i> STORM imaging of microtubules in U2OS cells.	95

LIST OF ACRONYMS (or) ABBREBIATIONS

AF647	Alexa Fluor 647
AIP	average intensity projection
BFP	back focal plane
CCD	charge-coupled device
DM	deformable mirror
DOF.....	depth of field
DH-PSF.....	double helix point spread function
EDOF	extended depth of field
EEF2	eukaryotic translation elongation factor 2
EM.....	electron microscope
EMCCD	electron multiplying charged-coupled device
ETL	electrically tunable lens
FOV.....	field of view
FWHM	full width at half maximum
LoG	Laplacian of Gaussian
MERFISH	multiplexed error-robust fluorescence in situ hybridization
MIP	maximum intensity projection
NA.....	numerical aperture
PALM	photoactivated localization microscopy
PBS	polarized beam splitter
PSF	point spread function

qPCR.....quantitative polymerase chain reaction

smFISHsingle-molecule fluorescent in situ hybridization

SBR.....signal to background ratio

sCMOS.....scientific complementary metal–oxide–semiconductor

SIMstructured illumination microscopy

SLMspatial light modulator

SMLM.....single-molecule localization microscopy

SNR.....signal to noise ratio

SRRF..... super-resolution radial fluctuation

STED.....stimulated emission depletion

STORM.....stochastic optical reconstruction microscopy

TOP2A..... topoisomerase 2- α

WF.....wide field

CHAPTER 1 INTRODUCTION

High-throughput and high-content imaging is a powerful tool in cell biology for studying cellular disease mechanism¹ and addressing many biological questions of interest in single cell levels². High-throughput microscopy has played an important role for the screening and profiling of cellular features by conducting a large number of experiments in a large cellular population with automated image acquisition. Biological information is then quantitatively extracted using automated image analysis at the level of molecules, single cell or even whole organism. High-content screening has been used for many applications including the identification of genes involved in a particular biological process¹ or required for cell differentiation², the exploration of cellular disease mechanisms³, the examination of proteome-wide changes induced by the genetic perturbation⁴, to name a few. High-throughput fluorescent microscopy has long been highly demanded attributed to its high spatial/temporal resolution⁵, allowing time-lapse studies⁶ and versatile to examine biological phenomena and cellular functions⁷⁻¹⁰ in cells as well as tissues.

In particular, single-cell transcriptomics, powered by the development of high-throughput technologies, such as quantitative polymerase chain reaction (qPCR)¹¹, next generation RNA sequencing (RNA-seq)^{12,13}, and single-molecule RNA fluorescence in situ hybridization (smFISH)¹⁴, allows hundreds to thousands of transcripts to be measured simultaneously in individual cells. Compared to bulk transcriptome, in which information from individual cells are generally averaged out, single-cell transcriptomics allows one to examine biological phenomena and study complex disease in sub-cellular vision. Although single-cell qPCR and mRNA-seq, as sensitive tools, have shown their capability to measure multiple gene expression in an accurate and high-speed manner with recent advances in the development of automated handling systems¹⁵⁻¹⁷,

subcellular localization of mRNA molecules is excluded due to the extraction of genes from individual cells. However, the spatial information plays an important role in understanding many biological activities. For example, in different gene expression levels, distinct cell types have been shown within the tissues and the spatial localization of those cell types provides a critical insight to reveal how tissue function and dysfunction arising from the responses of individual cells to the microenvironment. In addition, a recent study has shown a strong correlation between mRNA localization and the spatial organization of cellular architecture and function¹⁸. Therefore, it's essential to measure not only transcript abundance but also the spatial localization within the cell^{7,8}.

To this end, imaging-based single-cell transcriptomics using smFISH has become an invaluable method to reveal the spatial localization and quantify the abundance of specific transcripts in single cells by using fluorescent-labeled FISH probes to target transcripts that have complementary sequence with the designed probes. Thus, single-molecule mRNAs can be directly visualized as bright diffraction-limited spots under a microscope. Owing to numerous developments in different types of FISH probes and continuously improved smFISH techniques, such as increased sensitivity of single-molecule detection by using either few FISH probes heavily labeled with fluorophores^{19,20} or a large number of singly labeled probes¹⁴ and increased capability of imaging different RNA species simultaneously by using combinatorial labeling with multi-color-based barcodes or sequential hybridization²¹⁻²³, smFISH has been widely used for studying subcellular gene expression in biological science²⁴. Remarkably, a recent achievement done by Zhuang et al. has shown a simultaneous image of 100 to 1000 distinct RNA species in hundreds of individual cells by developing a multiplexed error-robust fluorescence *in situ* hybridization (MERFISH) technique²⁵.

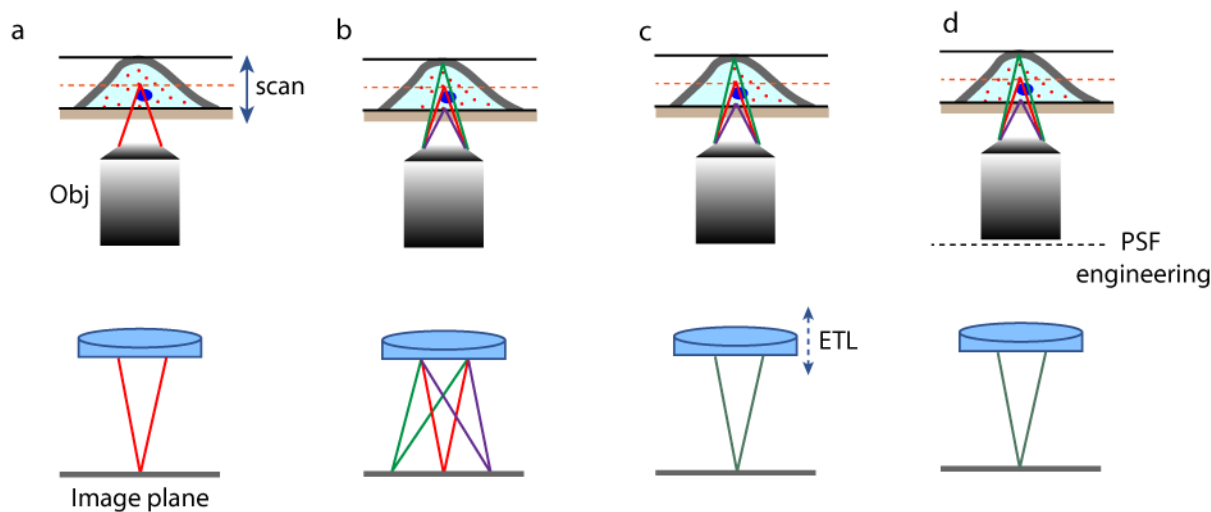


Figure 1 Four different approaches to volumetric imaging. (a) 3D stacks of images acquisition by mechanically moving the specimen or the objective lens. (b) Multiple focal plane can be simultaneously refocused onto different areas of a single exposure camera by using a distorted diffraction grating combine with other aberration correction elements. (c) The imaging lens in front of the camera can be replaced with electronically tunable lens (ETL) or deformable mirror¹³. By rapidly changing the focal length driven by electronical source, 3D information can be simultaneously imaged on the single exposure camera. (d) Extended depth of field can be achieved by encoding the wavefront at the back focal plane using a transmitted phase plate or spatial light modulator (SLM). An invariant point spread function within a specific range projects 3D information onto a single snapshot image.

To visualize subcellular features, large numerical aperture (NA) imaging systems are necessary for achieving high-resolution images while improving the light collection efficiency, especially, for photon-limited applications, such as single molecule imaging. However, the fact that the focal volume is inversely proportional to the cubic of numerical aperture (NA^3) of the imaging system makes it necessitated to serially scanning through the cell volume to obtain the three-dimensional (3D) images which in general are achieved by mechanically moving the samples

using a piezo-stage (Figure 1a). This process is not only very time-consuming, but also wastes photons²⁶ emitted from fluorophores residing in out-of-focus regions under the epi-illumination. For some specific applications, such as monitoring the dynamic behaviors of living cells, the mechanical movement may also introduce unexpected perturbation during the image acquisition. As a result, current high-throughput microscopy shows a severe drawback in the imaging speed compared to other imaging-based techniques such as imaging flow cytometry^{27,28} that is 2-3 order of magnitude faster than fluorescent microscopy.

To overcome these issues and further improve the speed of throughput measurements, various approaches have been developed to extend the depth of field (DOF) for fast volumetric imaging, particularly toward less or no serial z-scanning^{29,30}. For instance, it was proposed that multiple focal planes can be simultaneously imaged onto different areas of a camera in a single snapshot²⁶ by using a distorted diffraction grating^{31,32} (Figure 1b). whereas this approach enables up to nine focal planes to be imaged simultaneously, the effective field of view (FOV) and SNR³² are significantly limited because of channel splitting. More importantly, to compensate the chromatic aberration induced by the diffraction grating, chromatic corrected grating combined with prism are required, further increasing the complexity and alignment difficulty of the imaging system. By rapidly scanning the focal plane (Figure 1c) using an electrically tunable lens³³, or tunable acoustic gradient index of refraction lens³⁴, remote focusing³⁵ or a deformable mirror^{36,37}, the effective DOF can be further extended with a projected image in a single camera exposure. In these methods, a near-uniform focal response with diffraction-limited lateral resolution is typically generated over an extended axial range, they exhibit a poor signal to noise ratio (SNR) owing to a short detection duty cycle, which in turn makes them unsuitable for photon-limited applications.

Given the extent of DOF of an imaging system is tightly related to the point spread function (PSF) representing the resolution of the system, i.e. a larger DOF is equivalent to a longer PSF along the axial direction, a variety of PSF engineering methods have been reported to extend DOF by encoding the wavefront at the back focal plane (BFP) of an objective lens^{38,39} (Figure 1d). Compared to other approaches, PSF engineering method exhibits many merits, such as the compatibility with high NA objectives, flexibility of adjusting DOF and the ability of aberration correction with implementing an adaptive element. For example, by intentionally introducing common aberrations, such as a combination of coma and trefoil⁴⁰, or primary spherical aberration^{41,42}, extended DOF has been theoretically and experimentally demonstrated for fast volumetric imaging. Another typical PSF engineering method is to generate an Airy-beam shaped PSF using a cubic phase mask³⁸. However, they are either restricted for use in low NA systems^{43,44} or suffer from a considerable amount of side lobes in the resulting images, requiring a careful deconvolution to reconstruct the original images⁴⁵.

Phase modulation can be conducted by using a deformable mirror^{13,46} or a liquid crystal spatial light modulator⁴⁷ (SLM). Whereas DMs exhibit high light efficiency owing to their reflective nature, the relatively small number of actuators (ranging from several tens to hundreds) and the control mechanism of each actuator make them unsuitable for generating some certain phase patterns such as binary phase with sharp variation or phase vortices requiring high-resolution³⁰. Moreover, some coupling effects are also inevitable arising from the position control of adjacent actuators⁴⁸. In contrast, SLMs with a large number of pixels could display sophisticated phase patterns more faithfully, but are not commonly used in engineering the detection PSF due to its inherent response to only linearly polarized light, resulting in an inevitable loss of

fluorescence light (~50%) after a polarization selection. Whereas the transmission efficiency can be improved by simply replacing the SLM with a well-designed passive phase plate³⁰, it loses the additional degree of freedom arising from an adaptive element, such as correcting sample^{49,50} or imaging system induced aberrations⁵¹.

To overcome the loss issue from an SLM, several approaches have been suggested for polarization-insensitive SLM⁵¹⁻⁵⁵ via a specific designed geometries. For example, by using a birefringent beam displacer⁵² or a polarized beam splitter^{53,54}, two orthogonal polarized beams can be separated and rotated by a half-wave plate such that each component is oriented in the correct polarization before reaching onto the SLM. A double-pass SLM configuration^{51,55} has also been reported to achieve 3D-donut beam shaping using a single SLM, where orthogonal polarized beams share the same optical path and their wavefronts are modulated independently by specific phase patterns imprinted at adjacent areas of an SLM. However, these techniques have only been successfully demonstrated for laser beam shaping, such as excitation beam in fluorescence microscopy. EDOF via PSF engineering still suffers significantly light loss when an SLM is used for manipulating the wavefront of the emission light^{38,56}. Whereas several techniques have been proposed to mitigate this problem via first splitting two orthogonal polarized components and modulating each one independently and then imaging them onto different areas of a camera^{57,58}, the SNR of each polarized image is still inherently limited by the physical separation of two polarizations.

When imaging thick biological samples, one may have to deal with aberration from the specimen and a strong autofluorescence background. Both would significantly reduce the signal to background ratio (SBR) of images, resulting in a difficulty in faithfully resolving subcellular

structures. To suppress the autofluorescence⁵⁹, specific sample treatments including signal amplification⁶⁰ and tissue clearing⁶¹, and/or tailing the excitation beam using a highly inclined beam^{62,63} or light-sheet microscopy^{33,43} have been suggested for background reduction. An adaptive element, such as SLM, used for extended PSF engineering can be easily applied for aberration correction by superposing phase patterns aimed for each purpose together onto the single SLM.

In cell biology, not only fast high-throughput volumetric imaging is highly demanding, but also a super-resolution imaging is desirable to visualize nanometer-scale biomolecules or proteins⁶⁴. In this regard, a multi-functional microscope allowing fast volumetric imaging as well as super-resolution imaging would be a powerful tool for biological studies. However, an increased spatial resolution using a high NA objective generally would reduce the DOF, lowering the volumetric imaging speed, vice versa. Fortunately, SLM-based imaging systems could well integrate two types of microscopies together by simply switching the phase patterns without introducing additional add-on modules. Owing to numerous studies of photo-switching mechanism⁶⁵⁻⁶⁷ of various organic dyes, molecules located within the diffraction-limited volume can still be distinguished with nanometer resolution by stochastically switching-on a sparse set of fluorophores at each time frame and accurately localizing the 3D position of each emitter by PSF engineering methods^{47,68-70}, categorized as single-molecule localization microscopy (SMLM). Therefore, with an adaptive element, such as SLM, the wavefront at the BFP of an objective can be easily manipulated to either extend the DOF for fast volumetric imaging or encode the depth information for 3D super-resolution imaging.

The thesis is organized as follows:

In Chapter 2, we presented a theoretical model for generating an elongated PSF by encoding the wavefront at back focal plane of the objective lens using a binary phase pattern (2.5D phase). Focal responses with a high NA imaging system were simulated based on vectorial Debye diffraction theory. We demonstrated the tunability of imaging depth using our approach. The focal response of this phase pattern to the broadband light and Comparisons with one typical PSF engineering method and with a low NA imaging system were further discussed.

In Chapter 3, we first characterized the 2.5D imaging system with $NA = 1.4$ by measuring the PSF of the system using gold nanoparticles and Strehl ratio of the peak intensity with 2.5D microscopy (2.5DM) and a clear aperture by single molecule DNA imaging. Then, we demonstrated the potential advantages of 2.5DM by performing quantitative high-throughput smFISH mRNA imaging over a $2 \times 2 \text{ mm}^2$ region in mammalian cells with less than 10 min. Multi-color imaging with two mRNA species labeled with different dyes was also demonstrated. Finally, this approach has also been applied to immunofluorescence imaging at a $>30 \text{ Hz}$ frame rate with much reduced photobleaching.

In Chapter 4, we demonstrated a polarization-insensitive SLM-based 2.5D imaging system that substantially overcomes the loss issue of an SLM, improving the transmission efficiency in the detection path from 41% to 77%. We also demonstrated the capability of the SLM-based imaging system for correcting aberrations from the system and the specimen. By combining 2.5D phase mask with the phase pattern for correcting aberrations, we further showed the advantages of our imaging system used for fast volumetric imaging of thick specimens with depth aberration correction correspondingly.

In Chapter 5, we demonstrated a 3D SMLM using PSF engineering methods which encode the depth information into the shape of the PSF. We first characterized the imaging system by extracting an essential parameter of the PSF and creating the calibration curve of the distinct parameter as a function of the defocusing depth using fluorescent beads. 3D localization precision of single molecules was then characterized by analyzing $\sim 2,000$ localization events from well-isolated molecules. Finally, we validated the 3D SMLM by performing immunostaining imaging of microtubules in mammalian cells with a measured resolution of ~ 48 nm.

In the last chapter, we summarized important results of current work and discussed about different prospects in the future work.

CHAPTER 2 PRINCIPLE OF 2.5DM

The 2.5D microscope is based on one of four categorized approaches for extending the depth of field as described in Figure 1, called PSF engineering methods in which the wavefront at the BFP of the objective lens^{38,71} is modulated via an adaptive optics, such as SLMs, DMs, or passive phase plate. As a result, a tightly focused PSF in a conventional microscope becomes elongated along the axial direction and volumetric information within a specific imaging thickness (determined by the elongated PSF) could be directly encoded onto a 2D projected image plane. An image post-processing may be required depending on the complexity of generated PSFs⁴⁵ by different phase functions. Compared to other approaches shown in Figure 1, PSF engineering techniques exhibit several merits in terms of compatibility with high NA imaging systems, tunability of the imaging depth and flexibility of correcting aberrations from the system with the implementation of adaptive optics.

2.1 Vectorial Diffraction Theory

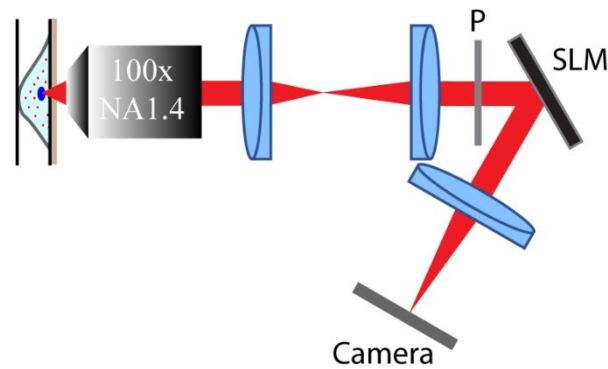


Figure 2 Schematic of a simplified imaging system. Obj, Objective; L1-3, lens; BFP, back focal plane.

As shown in Figure 2, a typical microscope is composed of an objective lens and a tube lens as a 4f imaging system. Another 4f system composed of two lenses relays the BFP on a conjugated BFP, where an adaptive optics, such as SLM, is placed to effectively manipulate the wavefront. Here, to maintain the axis-symmetry of the resulting PSF, we intentionally seek for a circularly symmetric phase function as the modulation, which can be expressed as

$$P(\rho) = \exp [j\phi(\rho)] \quad (1)$$

where ρ is a normalized radial coordinate at BFP, $\phi(\rho)$ represents the phase function, and a constant amplitude of the electrical field is assumed at BFP. To simplify the system, we can start with a scalar diffraction theory, in which the complex amplitude in the focal region can be written as⁷²

$$U(v, u) = 2 \int_0^1 P(\rho) J_0(v\rho) \exp(ju\rho^2/2) \rho d\rho \quad (2)$$

where v and u are radial and axial optical coordinates at the image plane: $v = kr\sin(\alpha)$, $u = 4kz\sin^2(\alpha/2)$, respectively, and the numerical aperture of $\sin(\alpha)$. Correspondingly, the intensity response in the focal region is

$$I(v, u) = 4 \left| \int_0^1 P(\rho) J_0(v\rho) \exp(ju\rho^2/2) \rho d\rho \right|^2 \quad (3)$$

As one can see that the intensity distribution along the optical axis is

$$I(0, u) = 4 \left| \int_0^1 P(\rho) \exp(ju\rho^2/2) \rho d\rho \right|^2 \quad (4)$$

With a change of variable $t = \rho^2$, Equation 4 can be rewritten as

$$I(0, u) = \left| \int_0^1 \Phi(t) \exp(jut/2) dt \right|^2 \quad (5)$$

Thus, the axial amplitude is the Fourier transform of the pupil function $\Phi(t)$. Based on Parseval theorem, the integral of the axial intensity function is calculated as

$$\int_{-\infty}^{\infty} I(0, u) du = \int_{-\infty}^{\infty} \left| \int_0^1 \Phi(t) \exp\left(\frac{jut}{2}\right) dt \right|^2 du = \int_0^1 |\Phi(t)|^2 dt = \text{constant} \quad (6)$$

which indicates that a larger depth of field results in a lower mean value of the axial intensity. One should be aware of a trade-off of the extent of DOF and SNR, in particular, applying EDOF methods for photon-limited applications.

Typically, an optical imaging system implemented with a high NA objective lens is necessitated for imaging subcellular structures, such as single molecule imaging that requires a high spatial resolution and light collection efficiency. In such scenario, the approximation based on scalar diffraction theory, i.e., paraxial approximation, Fresnel and Fraunhofer approximation are no longer satisfied⁷³. vector properties of electromagnetic (EM) field should be taken into consideration, the electrical field around the focal region can be written based on vectorial Debye diffraction theory as⁷⁴:

$$E(x, y, z) = -\frac{ic}{\lambda} \int_0^\alpha \int_0^{2\pi} \sin\theta A(\theta, \varphi) B(\theta, \varphi) P(\theta, \varphi) \exp[ikn(z\cos\theta + x\sin\theta\cos\varphi + y\sin\theta\sin\varphi)] d\theta d\varphi \quad (7)$$

where θ is the angle of the light exiting from the pupil plane toward the focal plane, α is the maximum focusing angle of the objective lens. $A(\theta, \varphi)$ represents the complex amplitude of the electrical field at the pupil plane. Without amplitude or phase engineering, $A(\theta, \varphi) = 1$. If a mask is placed at BFP, this term will be modified accordingly. $B(\theta, \varphi)$ is the apodization factor, indicating the energy conservation before and after lens aperture, here is referred as $B(\theta, \varphi) = \sqrt{\cos\theta}$. $P(\theta, \varphi)$ indicates the polarization effect of the electrical field in the focal region, which can be expressed as:

$$P(\theta, \varphi) = \begin{bmatrix} 1 + (\cos\theta - 1)\cos^2\varphi & (\cos\theta - 1)\cos\varphi\sin\varphi & -\sin\theta\cos\varphi \\ (\cos\theta - 1)\cos\varphi\sin\varphi & 1 + (\cos\theta - 1)\sin^2\varphi & -\sin\theta\sin\varphi \\ \sin\theta\cos\varphi & -\sin\theta\sin\varphi & \cos\theta \end{bmatrix} \begin{bmatrix} p_x \\ p_y \\ p_z \end{bmatrix} \quad (8)$$

Based on the vectorial Debye theory, in a high NA imaging system, EM field distribution in the focal region is subject to various parameters, i.e., complex amplitude, the polarization of the incident light, and NA of the objective lens. All simulations about focal response performed in our work were based on the integral formula of Equation 7.

2.2 Design of 2.5D Phase Pattern

Circularly symmetric phase function has been proposed to achieve extended DOF literally^{42,75-77} and experimentally⁴¹. For instance, by combining spherical aberration and defocus, named quartic phase mask, an axial invariant PSF can be generated over a certain distance with a relatively sharp focus. The lateral shape of the PSF is circularly symmetric in contrast to a cubic phase mask⁴⁵ and the phase modulation ensures a high transmission efficiency compared to an amplitude mask⁷⁸. However, there are two main problems for this approach. Firstly, the intensity of PSF along the axial direction rapidly oscillates, which may cause a loss in the depth information when projecting volumetric information onto a 2D image plane. Secondly, the lateral resolution is not constantly preserved within the extended DOF. To overcome these issues, instead of using a circularly symmetric phase function in a continuous manner, a binary phase function⁷⁹ attracted our attention because it shows an outstanding uniformity of axial intensity of the PSF over a designed EDOF with a relatively sharp focus and well-preserved circularly symmetrical intensity distribution around the focal region. Unlike other approaches showing a rapid variation⁴¹ or a Gaussian-shaped response⁸⁰, high-uniform PSF generated by a binary phase function is desirable for performing

quantitative intensity analysis. However, this has only been proposed theoretically in a low NA imaging system.

To design a binary phase function that generates a uniform PSF over a certain distance. We first introduce two circularly symmetric phase functions, i.e. a combination of spherical aberration (P_{sp}) and defocus (P_{df}) at the BFP of the objective lens, which can be written as

$$P_{\text{sp}}(\rho) = \exp(2\pi i \gamma \rho^4) \quad (9)$$

$$P_{\text{df}}(\rho) = \exp(2\pi i \psi \rho^2) \quad (10)$$

Where ρ is the normalized radial coordinate with respect to the maximum radius of the pupil aperture. γ represents the strength of the spherical aberration and determines the extension of the axial PSF. ψ is a parameter used to control the position of the focus plane. a binarization of the circularly symmetric phase function was induced to convert a continuous phase function to a binary phase mask with only 0 and π phase value. The binary phase function composed of two axisymmetric aberration terms can be expressed as

$$P_{\text{bin}}(\rho) = \text{Binary}[\exp(2\pi i(\gamma \rho^4 + \psi \rho^2))] \quad (11)$$

where the binarization criterion is defined as⁷⁹:

$$\text{Binary}[P(\rho)] = \begin{cases} 1 & \text{Re}[P(\rho)] \geq 0 \\ -1 & \text{Re}[P(\rho)] < 0 \end{cases} \quad (12)$$

Once one parameter γ was fixed for a specific depth-extension, another parameter ψ was optimized until a defocus-invariant PSF was attained within the designed depth range. All simulations regarding the intensity distribution of the PSF were conducted under an imaging system where the NA of the objective lens is 1.4, the wavelength is 670 nm which is close to the emission peak of a common red-emitting fluorophore Alexa Fluor 647 (AF647), and the refractive index of the medium between the objective lens and sample is 1.518, unless specified otherwise.

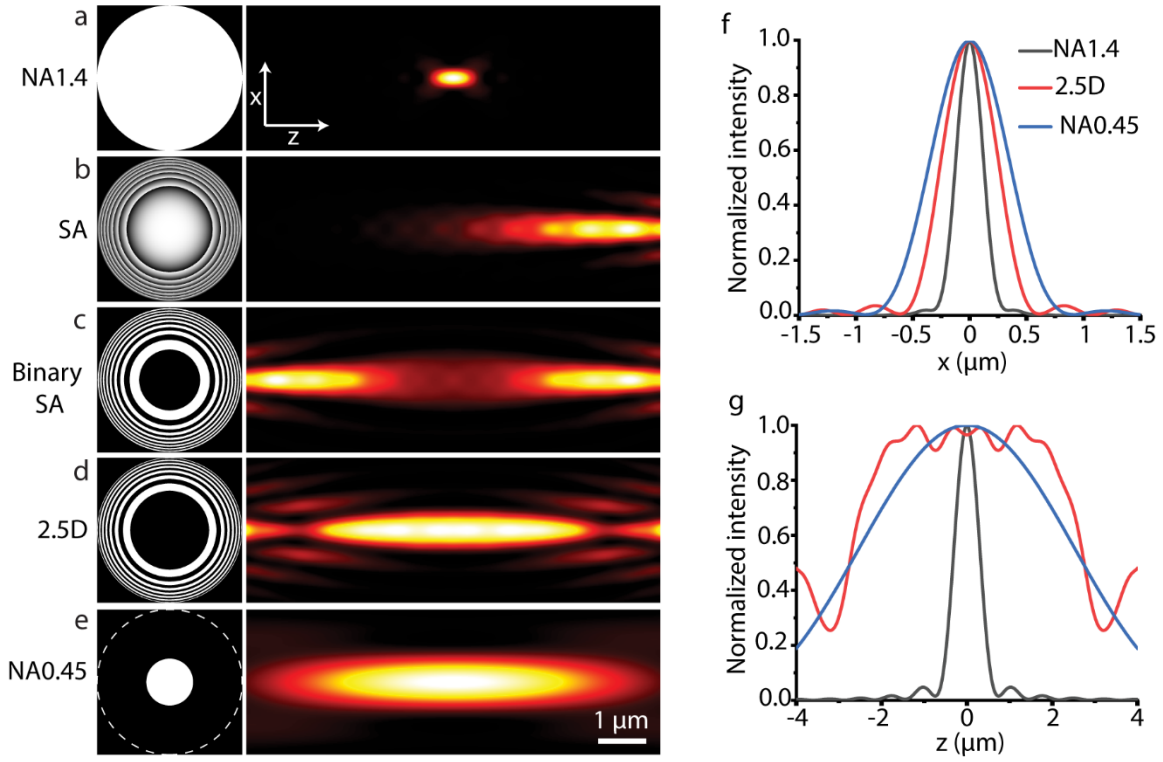


Figure 3 Working principle of 2.5DM by simulation. (a-e) Focal responses at the x-z plane by implementing different phase functions at BFP: (a) a clear aperture with $\text{NA} = 1.4$, (b) a phase pattern with spherical aberration (SA), (c) a binarized spherical aberration pattern (binary SA), (d) a 2.5D phase created by binarizing a combined phase functions composed of spherical aberration and defocus term and (e) a clear aperture with $\text{NA} = 0.45$. (f-g) Intensity profiles along the lateral (f) and axial (g) direction for three different cases: a clear aperture with $\text{NA} = 1.4$ (black), 2.5D phase (red) and a clear aperture with $\text{NA} = 0.45$ (blue). The wavelength is 670 nm, the refractive index of the sample is 1.518.

To design the binary phase function that satisfies our needs, 3D focal responses of a high NA imaging system ($\text{NA} = 1.4$) were simulated under different phase modulation at the BFP of the objective lens as shown in Figure 3. First, a spherical aberration ($\gamma = 8$) was applied on a pupil plane (Figure 3b). The resulting PSF was elongated along the axial direction but the centroid of

the focus was no longer located in the original plane compared to a tightly focused spot with a clear aperture (Figure 3a). Binarization of the spherical phase function using Equation 12 generated two focal spots that were symmetric with respect to the focal plane and further effectively extended the PSF (Figure 3c). As one can see that the binarization recovered the symmetry of the intensity distribution with relatively preserved PSF shape as that in Figure 3b. However, its axial intensity distribution was not uniform. More severely, low intensity was exhibited around the focal plane. To remedy this problem, we intentionally induced a defocus term by multiplying it with the spherical aberration and the combined phase function was binarized and optimized via adjusting the parameter ψ until a defocus-invariant PSF was obtained with a moderately uniform intensity distribution within a specific depth, for instance, $5.5\ \mu\text{m}$ in Figure 3d. Hereinafter, we would call this phase function as 2.5D phase pattern, while referring a clear aperture with $\text{NA} = 1.4$ to as widefield (WF).

The intensity profiles of PSFs along the lateral (Figure 3f) and axial (Figure 3g) direction were further compared for three representative cases, i.e., a clear aperture ($\text{NA} = 1.4$), 2.5D phase pattern ($\text{NA} = 1.4$) and a clear aperture with a low NA imaging system ($\text{NA} = 0.45$) in Figure 3f and 3g. The low NA system aims to generate a same DOF as achieved by a 2.5D phase pattern. Compared to a clear aperture, the resulting PSF generated by the 2.5D phase pattern showed an extension of depth of field by 8-fold with the broadening of the lateral width by only a factor of 1.8. However, the low NA system increased the lateral width by 2.8-fold given the same axial focal depth obtained by the 2.5D phase. Notably, compared to a Gaussian-shaped intensity distribution in the low NA system, the 2.5D PSF showed a remarkably uniform axial intensity distribution. To quantitatively characterize this, the full-width at 90% of maximum (FW90M), commonly used in

analyzing a flat-field illumination⁸¹, was calculated, showing a 1.8-fold larger FW90M by the 2.5D phase pattern than that in the low NA system. More importantly, the light collection efficiency of 2.5DM was 9.7-fold higher than the low NA system as it is proportional to the square of NA, which becomes more critical for photon-limited applications. When the 2.5D phase function optimized via scalar diffraction theory is applied directly to a high NA imaging system, axial intensity of the PSF exhibited a stronger variation than the optimized case via vectorial diffraction theory within the designed axial depth (Figure 4).

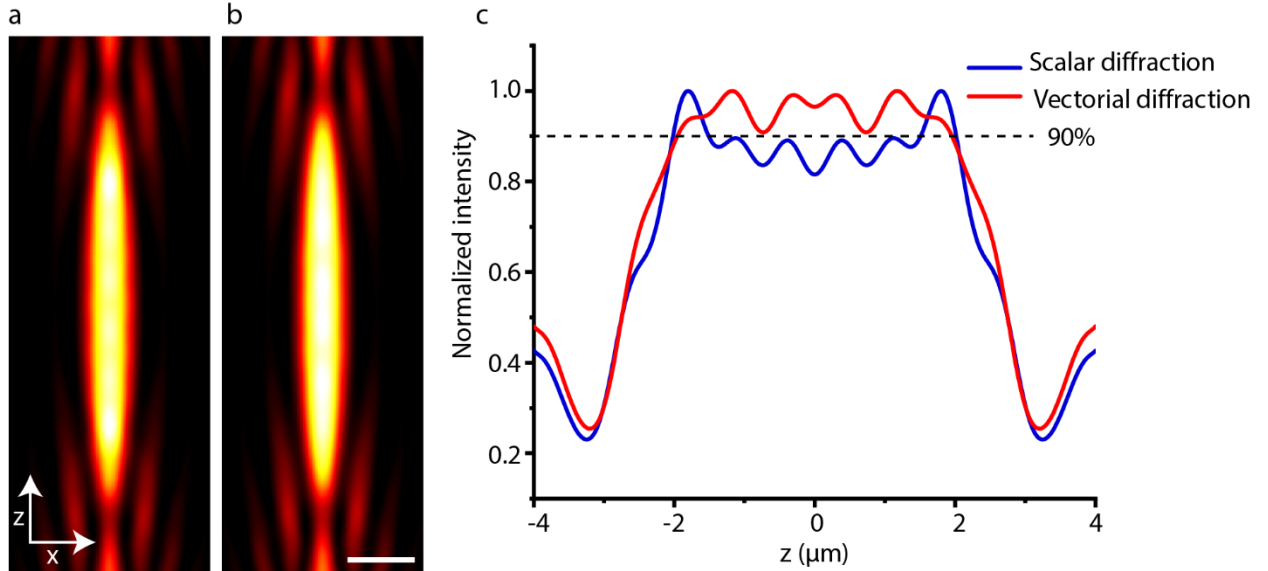


Figure 4 Focal responses by scalar and vectorial diffraction theory for 2.5D imaging. (a-b) Intensity distributions of the PSFs generated using scalar (a) and vectorial (b) diffraction theory at the x - z plane. (c) Axial intensity profiles of PSFs for the corresponding cases. A black dashed line indicates 90% of the normalized peak intensity.

2.3 Characterization of 2.5DM by Simulation

2.3.1 Comparison with Other PSF Engineering Methods

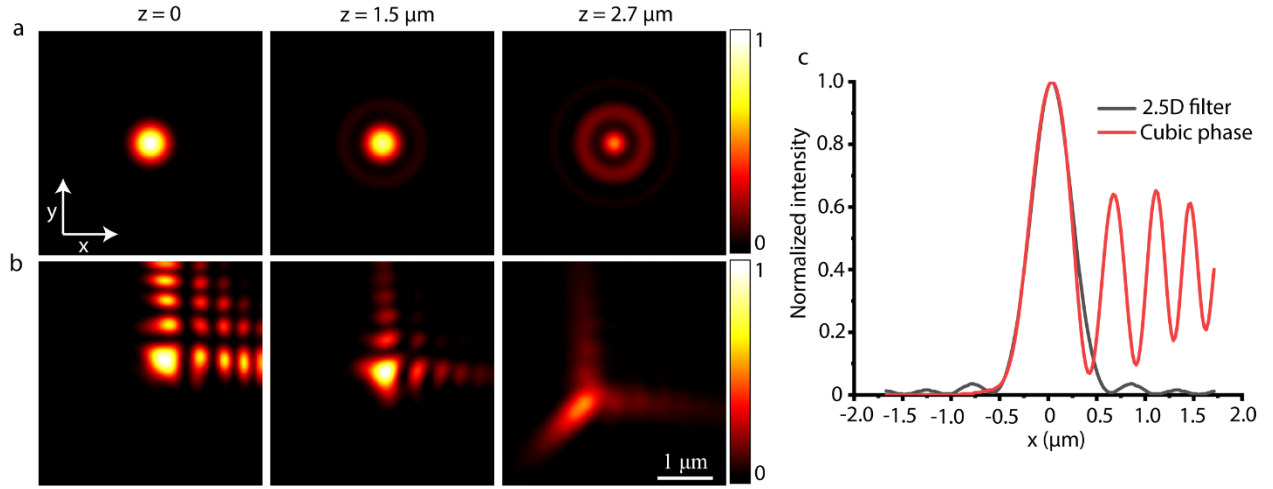


Figure 5 Comparison of focal responses by 2.5D phase pattern and cubic phase pattern. (a-b) Intensity distributions of the PSFs generated by the 2.5D phase pattern (a) and the cubic phase pattern (b) at the x - y plane. (c) The intensity profiles along the x -axis where $z = 0$. The same EDOF was generated by both two patterns. For both cases, the intensity was normalized to the peak intensity value where $z = 0$, respectively. the wavelength used in the simulation was 670 nm with $\text{NA} = 1.4$.

One typical EDOF imaging method, which has been reported theoretically⁸² and experimentally applied for fluorescence microscopy^{45,83}, is to generate an Airy-beam shaped PSF using a cubic phase mask, which can be expressed as $\Phi_{cubic}(x, y) = 2\pi\alpha(\frac{x^3+y^3}{\rho_{max}^3})$, where α represents a design parameter to determine the strength of extension of DOF. ρ_{max} is the largest radius of the pupil aperture. To fairly compare the focal responses by a cubic phase and our 2.5D phase, a parameter $\alpha = 2.4$ was used in the simulation to achieve a same axial full width at half maximum (FWHM) as shown in Figure 3d. As shown in Figure 5, the resulting PSF generated by

a cubic phase mask exhibited a considerable amount of side lobes and their peak intensities showed more than 60% of the maximal peak value (Figure 5c). To reconstruct a reliably original image, it requires a careful deconvolution, which may introduce artificial errors when a low-quality raw image was recorded. Furthermore, the multiple side-lobes at the transverse plane highly limits the structure density of a volumetric sample that can be imaged by this method. On the contrary, PSF generated by the 2.5D phase mask has shown neglectable side-lobe effect in the focal region with a circularly symmetric shape. It can be readily interpreted with a single snapshot image.

In contrast to EDOF methods via wavefront coding, the depth of focus can be also extended by manipulating the amplitude at the BFP, such as using an annular aperture, which generates a greatly elongated PSF while maintaining a diffraction-limited lateral resolution. However, the main issue limiting the annular aperture in fluorescence microscopy, in particular, in the detection path, is that only a small fraction of the emission light can be transmitted through the aperture and utilized for imaging. One method has been reported to achieve a similar PSF without scarifying the transmission efficiency by designing a multiple concentric annular mask⁸⁰, in which each sub-aperture would generate an elongated PSF with the designed DOF and the light passing through each sub-region becomes incoherent. The resulting PSF is an incoherent superposition of each PSF generated by the sub-aperture. The incoherence is achieved by introducing a phase-delay that is larger than the coherent length of the light between different annular apertures. Compared to the PSF generated by a multi-annular mask (Figure 6a), 2.5D phase pattern generated a defocus-invariant PSF (Figure 6b) with more uniformly axial distribution given the same FWHM whereas multi-annular mask exhibits a better lateral resolution. In addition, the adaptive optics used in 2.5DM enables us to imprint different phase functions, such as defocus, to further smooth the

intensity distribution along the axial direction by dithering over a depth of 1 μm along the z -axis (Figure 6c) without compromising the image acquisition rate.

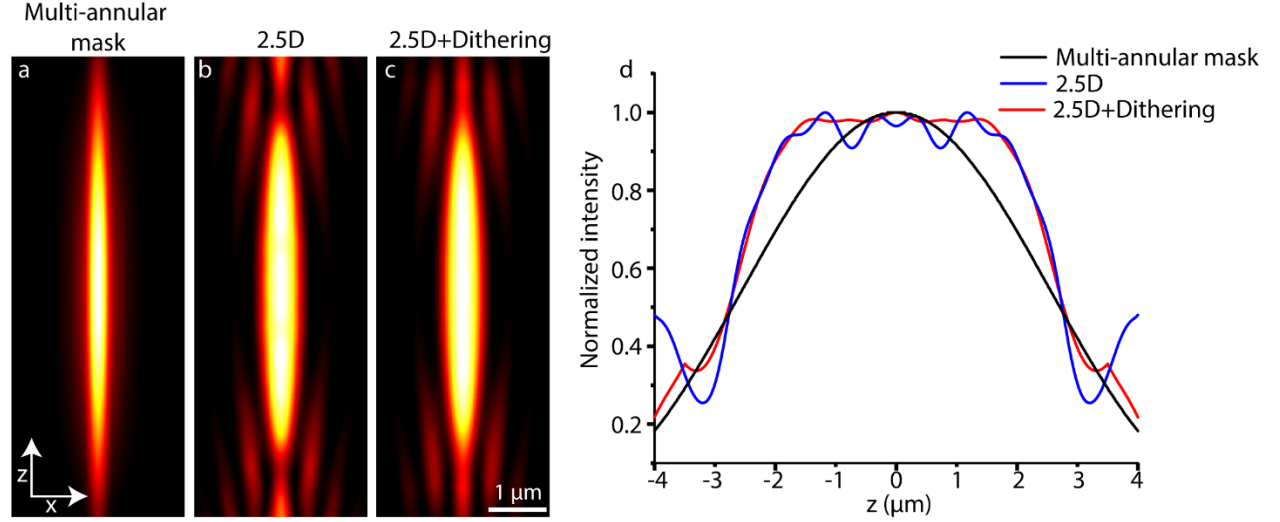


Figure 6 Focal responses by multi-annular mask, 2.5D phase pattern without/with dithering. (a-c) Intensity distributions of the PSFs generated by the multiple annular mask (a), 2.5D phase pattern without (b) and with (c) dithering over a depth of 1 μm at the x-z plane. (d) The intensity profiles along the z-axis for three corresponding cases.

2.3.2 Tunability of Imaging Depth

The fact that the 2.5D phase pattern is optimized via a combination of spherical aberration and defocusing enables our approach to adjust the DOF by simply controlling the strength of the spherical aberration term (γ). Correspondingly, for a given amount of the spherical aberration, the defocusing term (ψ) needs to be optimized until a moderately uniform intensity distribution is observed along the z -axis. By using an adaptive optics, such as SLM, different phase functions can be imprinted at the BFP accordingly based on the specific requirement for the imaging depth.

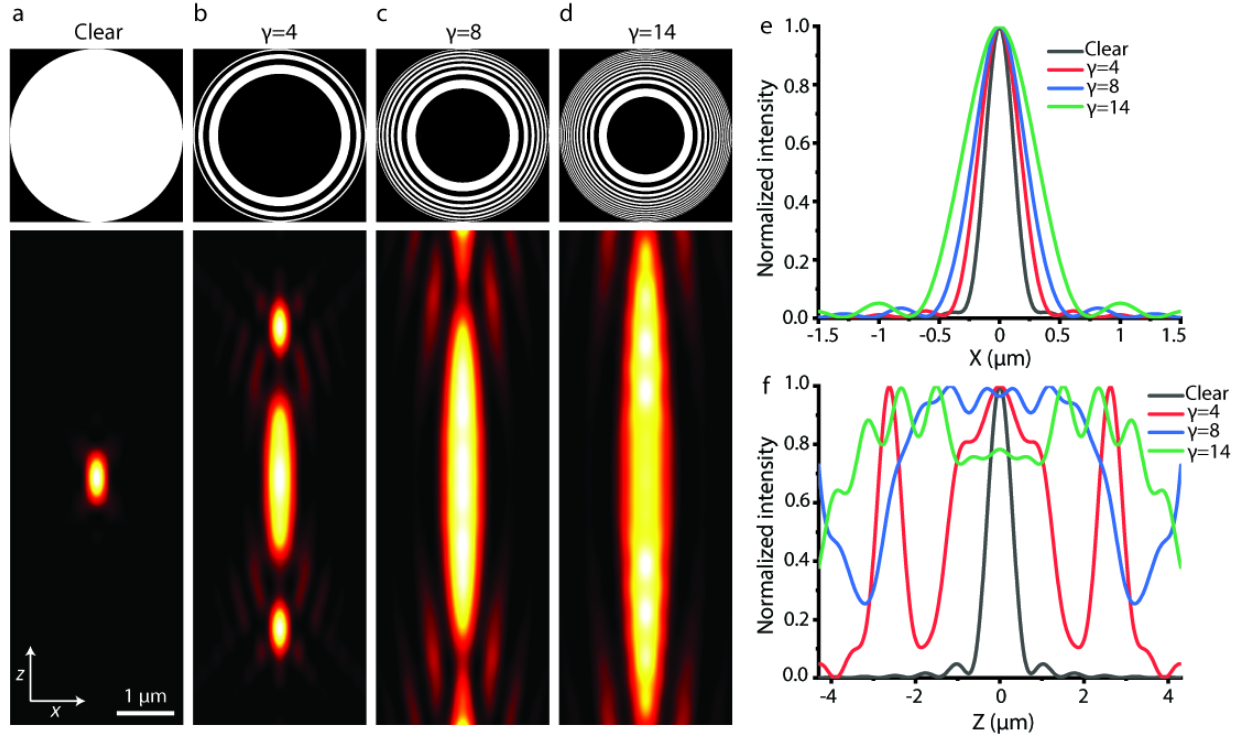


Figure 7 Tunable depth of field generated by controlling the spherical aberration strength. (a)-(d) Intensity distribution of the PSFs at the x - z plane by a clear aperture (a), an optimized 2.5D phase pattern with the spherical aberration strength $\gamma = 4$ (b), $\gamma = 8$ (c), $\gamma = 14$ (d). (e)-(f) Intensity profiles along the lateral and axial directions for the corresponding cases. Compared to the clear aperture, 2.5D phase mask increases the DOF by 12.6-fold, while broadening the lateral width by only a factor of 2.5 when $\gamma = 14$.

Figure 7 demonstrated that with different strengths of spherical aberration (γ), one can achieve variable DOF with uniform intensity distribution over a specific depth. As γ increased, the intensity ripple along the axial direction was observed (Figure 7f) attributed to the interference of two aberrated long foci. Compared to the tight focal spot with a clear aperture, the binary phase filter (when $\gamma = 14$) increased the DOF by 12.6-fold with broadening the lateral width by only a factor of 2.5. To clearly elucidate the advantage of the 2.5D phase pattern, we plotted FWHM of the axial PSF (Δz) as a function of the lateral FWHM (Δx) in a log-log scale (Figure 8). As we

know, with a clear aperture, an extended DOF is achieved by reducing the value of NA and the lateral and axial FWHMs follow a linear relation theoretically under the log-log scale with a slope efficiency of 2 which corresponds well with the fitted data in the simulation. Given the same DOF, compared to the clear aperture, 2.5D phase pattern minimized the broadening effect of the lateral resolution while providing a uniform axial intensity distribution over the designed depth. It should be noted that as shown in the plot (Figure 8), the slope efficiency of the 2.5D phase pattern started from a slope of ~ 3.3 and then decreased to ~ 0.83 at the DOF $\Delta z > 7 \mu\text{m}$. This may be explained by two possibilities: one is that as the strength of the spherical aberration increases, the growth rate of the EDOF generated by the aberration decreases above a certain threshold DOF. Secondly, the interference of two elongated foci reduces the extension of the PSF as they are highly overlapped with each other.

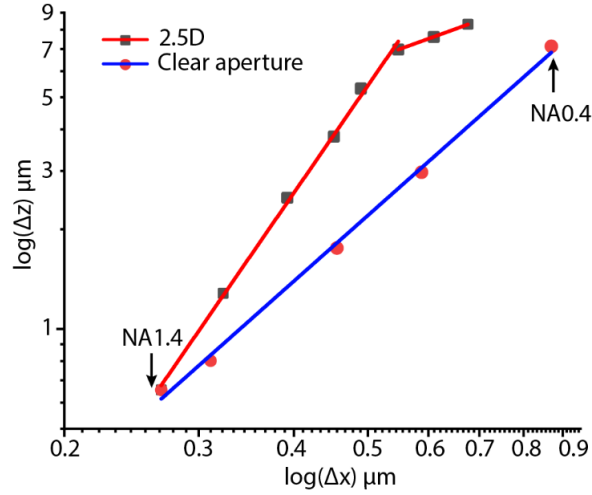


Figure 8 Log-log plot of FWHM of the axial PSF (Δz) as a function of the lateral PSF (Δx). The strength of spherical aberration in the 2.5D phase pattern and the value of NA in the clear aperture were adjusted to achieve different DOF. Both were linearly fitted where the clear aperture gave a slope efficiency of ~ 2 and 2.5D phase pattern showed a slope of efficiency ~ 3.3 at $\Delta z < 7 \mu\text{m}$ then reduced to ~ 0.83 .

2.3.3 Focal Response to Broadband Light

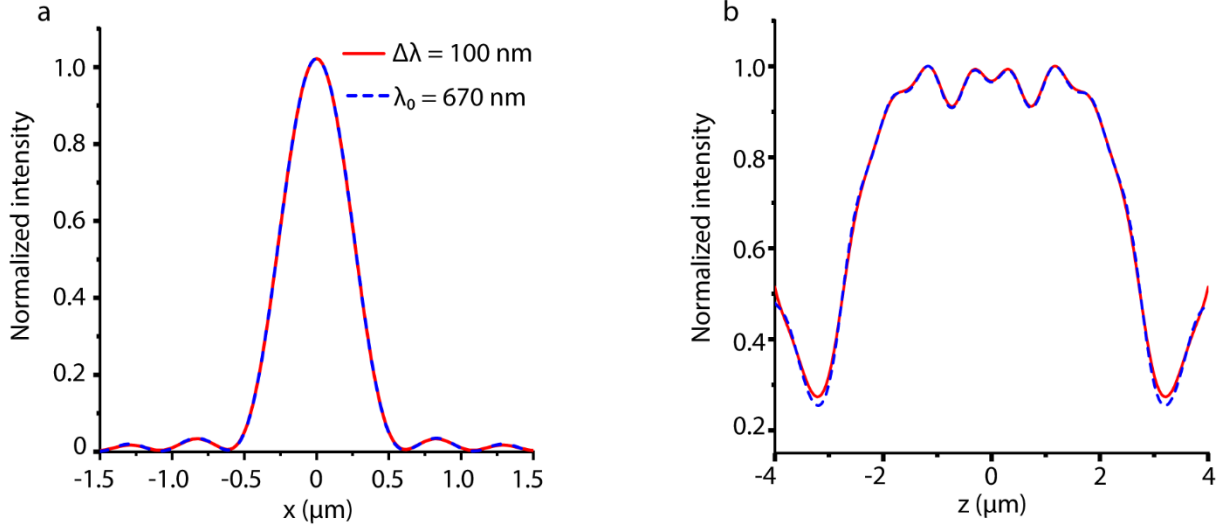


Figure 9 Response of 2.5D image to the broadband light. (a-b) Lateral (a) and axial (b) focal responses of the designed phase function under the emission of the monochromatic (dotted blue) and the broadband light (solid red) with the effect of weighting factors determined by the fluorescence emission power spectrum. A Gaussian-distributed fluorescence emission spectrum was assumed with FWHM of 100 nm.

The simulations conducted above was using a wavelength $\lambda = 670$ nm, which is the peak emission wavelength of a typical fluorescence dye, AF647. However, in fluorescence microscopy, the light emission is not monochromatic. In order to assess the feasibility of the 2.5D phase pattern to polychromatic systems, the focal response of the broadband light was examined using the same phase pattern ($\gamma = 8$, $\psi = -1.525$) designed for a monochromatic wavelength ($\lambda = 670$ nm). In our simulation (Figure 9), a broadband emission, centered at 670 nm and spanning 100 nm with Gaussian spectral distribution, was assumed. The spectral distribution provides a weighting factor for each wavelength and the focal response of the broaden emission was obtained by incoherently summing the intensity response of the PSFs at each wavelength with multiplication of a

corresponding weighting factor determined by the emission power spectrum. Compared to the PSF for the monochromatic light, the degradation of the intensity profiles along the lateral (Figure 9a) and axial direction (Figure 9b) was almost negligible for the broadband emission, confirming that the 2.5D phase pattern is tolerant to the wavelength variation and can be directly employed in the fluorescence microscopy.

CHAPTER 3 HIGH-THROUGHPUT IMAGING BY 2.5DM

3.1 Overview

High-throughput and high-content analysis is of utmost importance in studying subcellular features at a large number of cell populations in a systematic and unbiased manner^{84,85}. To understand biological response of each cell to different stimulation⁸⁶ and cell cycles⁸⁷, biomarkers such as proteins, RNAs and organelles could be labeled with fluorescent probes and analyzed in a single-cell level. Imaging-based approaches in single-cell analysis have been powerful for studying gene expression levels, spatial distribution of cellular proteins and the interaction network and molecular mechanism of biological processes⁸⁸⁻⁹⁰. These thorough studying for cell biology has been effectively performed by high-throughput fluorescence microscopy^{84,91} in an automated fashion, which provides direct visualization of subcellular features in diffraction-limited resolution in wide-field microscopy or super-resolution at tens of nm levels^{5,92}. It also shows powerful capability in studying dynamic behaviors of biological phenomena in live-cell imaging⁶ and versatility⁹³ to image tissues as well. In particular, imaging-based transcriptomics via single-molecule fluorescence in situ hybridization (smFISH)^{14,94} to directly visualize the spatial distribution of hundreds to thousands of transcripts simply as fluorescence spots under a microscope and immunofluorescence imaging using specific fluorescent probes (antibodies) to target different molecules or proteins have exhibited their tremendous power in studying fundamental biological phenomena and understanding subcellular functions⁷⁻¹⁰.

In conventional fluorescence microscopy, the imaging speed is 2-3 orders of magnitude slower than other techniques such as imaging flow cytometry^{27,28,95}, resulting in a significantly limited adoption of imaging-based high-through techniques. For traditional fluorescence

microscopy, 3D cell images are captured by serial z -scanning via mechanically moving the sample mounted onto a piezo-stage (Figure 10), which is the most time-consuming process in a high-throughput imaging system. The mechanical movement of the specimen not only limits the speed of image acquisition, but also perturbs the sample during the image acquisition. As a result, the perturbation may cause a measurement error or even be harmful to some specimens. Moreover, under the wide-field epi-illumination, fluorophores residing at out-of-focus regions are inevitably excited and easily photobleached, resulting in photodamage and waste of photons, particularly detrimental for photon-limited applications.

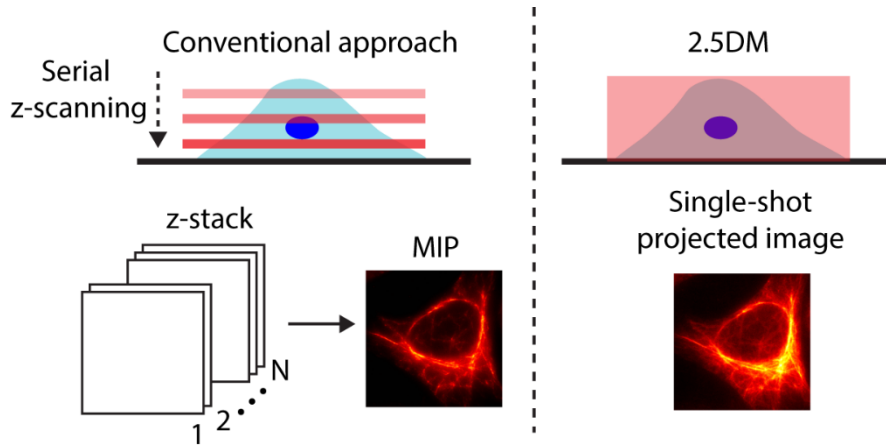


Figure 10 Volumetric imaging in a conventional microscopy and 2.5DM. Volumetric information is obtained by either serial z -scanning (left) or a single-shot projection (right).

To overcome issues occurring in serial z -scanning imaging systems, a large number of techniques have been suggested to achieve fast, volumetric imaging with less or no mechanically z -scanning^{22,23}. Among these approaches, one typical technique is to rapidly scan the focal plane through the cell volume to obtain either a 3D image stack with a high frame rate or a projected image within a single exposure time. This has been demonstrated by using either an electrically

tunable lens^{33,96}, tunable acoustic gradient index of refraction lens (TAG lens)³⁴, remote focusing³⁵ or a deformable mirror^{28,29}. In these approaches, while a near-uniform focal response with nearly diffraction-limited spatial resolution can be generated over a specific axial range, one has to deal with a poor SNR, resulting from a low detection duty cycle. Other techniques have also been proposed, such as instantaneous 3D imaging by projecting multiple image planes onto different areas of a camera⁹⁷ or via light-field microscopy⁹⁸, which either exhibits a low SNR³² or limited spatial resolution. Worthy to note that the severe degradation of SNR among these approaches makes them unsuitable to photon-limited applications, such as single-molecule imaging. In this chapter, we characterized an elongated PSF with high numerical aperture by encoding the wavefront in the pupil plane using the designed phase pattern described in chapter 2. The extended depth of field of the elongated PSF aims to cover the entire volume of a typical mammalian cell with a thickness of $\sim 4\text{-}6\text{ }\mu\text{m}$ and the volumetric information can be simultaneously projected onto 2D image plane in a single-shot camera exposure. The high uniformity of axial intensity profile and minimal side-lobes enable us to readily interpret the raw images without complicated image post-processing. Compared to WF microscopy, the peak intensity reduction by 2.5DM was quantitatively characterized. Based on the characterization of the detection PSF, high-throughput single molecule mRNA FISH imaging over a $2\times 2\text{ mm}^2$ was performed in mammalian cells in less than 10 min. Quantitative analysis of the copy number of mRNAs in individual cells and SBR were examined. To elucidate the capability of this approach in studying transcriptional abundance in cells, another species of mRNA species has been labeled with the same probes and imaged as well. Multi-color imaging and immunofluorescence imaging by 2.5DM were also demonstrated to show its versatile use.

3.2 Experimental Characterization of 2.5DM

To experimentally demonstrate 2.5D imaging with extended depth of field, a schematic of the customized microscope system is shown in Figure 11. Four continuous-wave (CW) lasers (638 nm, 532 nm, 488 nm and 405 nm; Colbolt) were coupled into a single mode fiber (P5-405BPM-FC-2, Thorlabs), and their powers were controlled by a combination of a half-wave plate and a polarized beam splitter. The laser beam from the fiber output was collimated by a lens (L1, $f = 100$ mm) and further expanded by a telescope composed of two lens (L2, $f = 50$ mm; L3, $f = 150$ mm) to obtain more uniform epi-illumination. an iris was placed after L3 to control the excitation beam size. The beam was then passed through a lens (L4, $f = 400$ mm) and reflected by a dichroic mirror (Di03-R405/488/532/635-t1-25×36, Semrock) and relayed an epi-illumination onto the sample plane through an objective (UPlanSApo, 100×/1.4, Olympus). A three-axis piezo stage (MAX311D, Thorlabs) controlled by an analog output board (PCI-6733, National Instruments) was used for holding samples and acquiring z stack images. Fluorescence emission was collected by the same objective and passed through an emission filter (FF01-446/523/600/677, Semrock). The emission fluorescence was focused by a tube lens (L5, $f = 180$ mm). Another 4f relay system composed of two lenses (L6, $f = 200$ mm; L7, $f = 200$ mm) were placed after the tube lens, giving a magnification of 100× in the imaging system. A spatial light modulator (SLM) (PLUTO-2-VIS-097, Holoeye) with resolution 1920×1080 pixels was placed at the conjugated back focal plane to generate the desired phase pattern. A polarized beam splitter was inserted before SLM to filter out the orthogonally polarized light which cannot be responded by SLM, avoiding the noisy effect added into the final image. A knife-edge mirror was used to redirect the light on the SLM, allowing a small incident angle limited by the performance

of the SLM (within $\pm 5^\circ$) in a compact configuration. The emission light was finally focused on a sCMOS camera (Zyla 4.2 sCMOS, Andor). An automated xy -stage (SCAN IM 120 \times 80, Marzhauser) and a piezo z -stage (Z-insert.100, Piezoconcept) were used for acquiring z -stack images and high-throughput images. In addition, a customized z -drift module was inserted in the illumination path to correct z -drift of the sample stage during the high-throughput imaging acquisition. Briefly, a collimated NIR beam (85-2302, Edmund Optics) was passed through a lens (L8, $f = 300$ mm), then reflected by another dichroic mirror (DM2, FF750-SDi02-25 \times 36, Semrock) and directed onto the sample through the same objective lens. The beam reflected from a coverglass was collected by a 50:50 beam splitter and focused onto a camera (DMK 23U618, The Imaging Source) by a lens (L9, $f = 60$ mm). The camera continuously monitored a shift of the NIR beam during the movement of the xy -stage and a feedback signal was sent to the piezo z -stage to correct the drift using pre-calibrated data controlled by a MATLAB script. To sequentially record multi-color images, an Arduino board (UNO R3; Elegoo) was used to digitally modulate on-off states of multiple lasers. All images were 2×2 binned and the FOV was $\sim 100 \times 100 \mu\text{m}^2$. The imaging acquisition was controlled by MicroManager.

In order to experimentally demonstrate the focal response by the 2.5D phase mask, we measured the PSF of the 2.5D imaging system using 80 nm gold nanoparticles embedded in immersion oil which aims to match the refractive index of the sample with that of an oil immersion objective lens ($\text{NA} = 1.4$). Gold nanoparticles, serving as point emitters, scatter the illumination light ($\lambda = 638$ nm), which then was collected through the detection path. The measured PSFs by the clear aperture (WF) and the 2.5D imaging system were shown in Figure 12a and 12b. Compared to WF, 2.5DM achieved an elongated focal spot along the axial direction with a

moderately uniform intensity distribution. The shape of the resulting PSF by 2.5DM corresponds well with the simulation demonstrated in Chapter 2. The intensity profiles along the lateral and axial direction were plotted in Figure 12c and 12d. One can see that 2.5DM extends the FWHM of the PSF along the z -axis from $0.63\ \mu\text{m}$ to $4.5\ \mu\text{m}$ while the FWHM along the x -axis increases from $0.32\ \mu\text{m}$ to $0.51\ \mu\text{m}$. Therefore, the 2.5D approach achieves an DOF extension of ~ 7.2 -fold but only broadens the lateral width by a factor of ~ 1.6 .

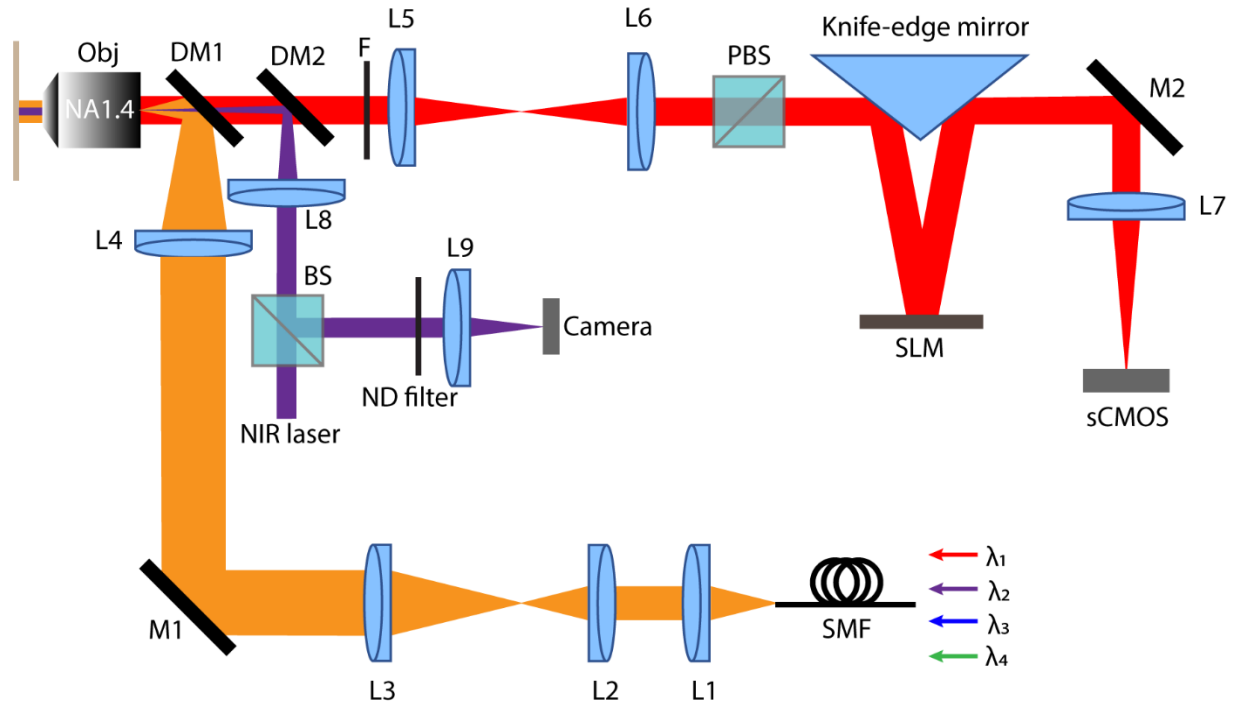


Figure 11 Experimental scheme of 2.5D microscopy. $\lambda_1 = 638\ \text{nm}$, $\lambda_2 = 405\ \text{nm}$, $\lambda_3 = 488\ \text{nm}$; $\lambda_4 = 532\ \text{nm}$; L1-7, lenses; M1-2, mirrors; SMF, single mode fiber; Obj, objective lens; DM1-2, dichroic mirror; PBS, polarized beam splitter; BS, beam splitter; SLM, spatial light modulator.

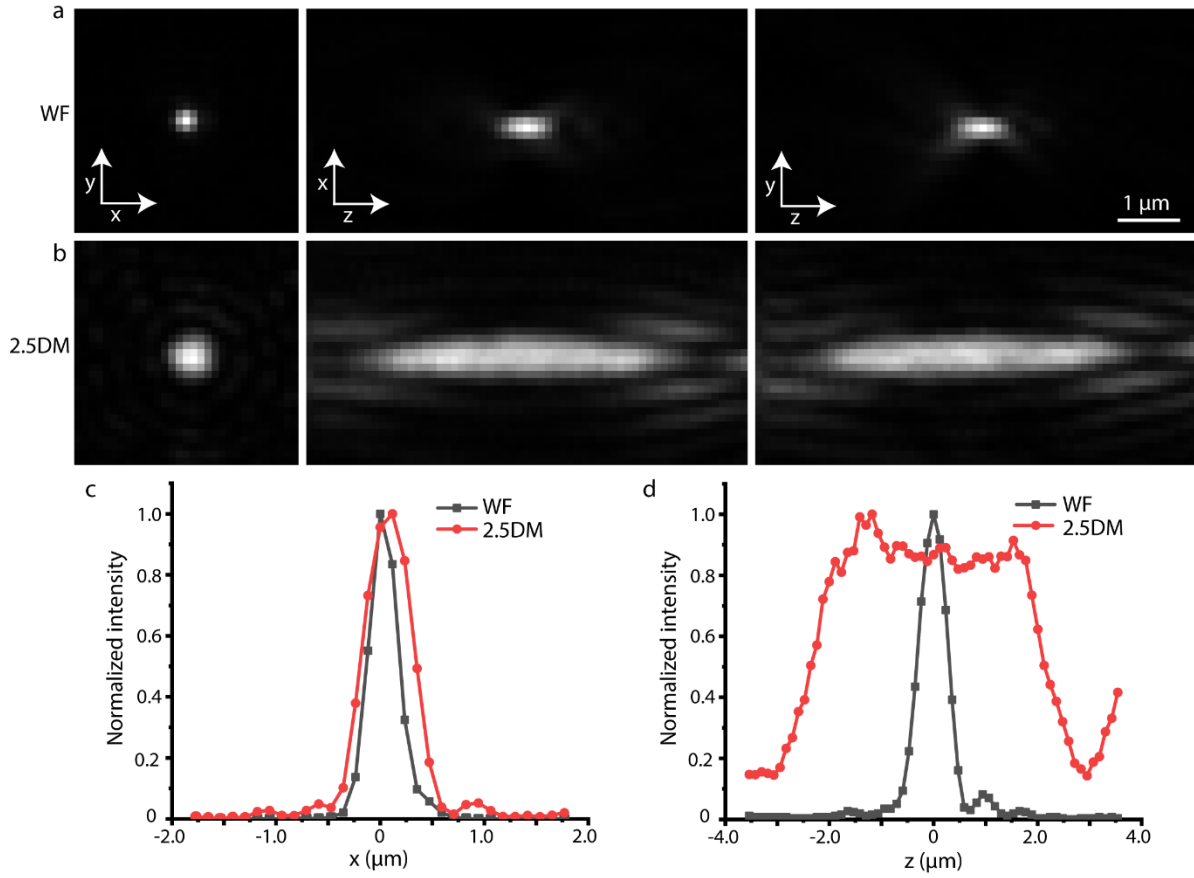


Figure 12 PSF measurements using 80 nm gold nanoparticles. (a-b) Intensity distributions at x - y , x - z and y - z planes, respectively, with a clear aperture (WF) (a) and with a 2.5D phase function (b). (c-d) Intensity profiles of WF (black) and 2.5DM (red) along the lateral (c) and axial (d) direction. 80 nm gold nanoparticles were embedded in immersion oil to match the refractive index with the immersion medium of the objective lens ($NA = 1.4$).

We further validated the focal response of the 2.5D imaging system using fluorescent beads and similar results were obtained as shown in Figure 13. To demonstrate the capability of the 2.5DM in 3D imaging, we prepared a 3D hydrogel bead sample using 200 nm fluorescent beads. First, a 3D stack of images with WF were obtained by serial z -scanning over ~ 4.5 μm (Figure 13e-13h) and projected onto a 2D image plane by maximum intensity projection (MIP) along the z -

axis (Figure 13i). For the same imaging area, we also recorded a single image in a snapshot by 2.5DM (Figure 13j). One can see that each fluorescent spot obtained by the 2.5D imaging system corresponds well with the projected image by WF.

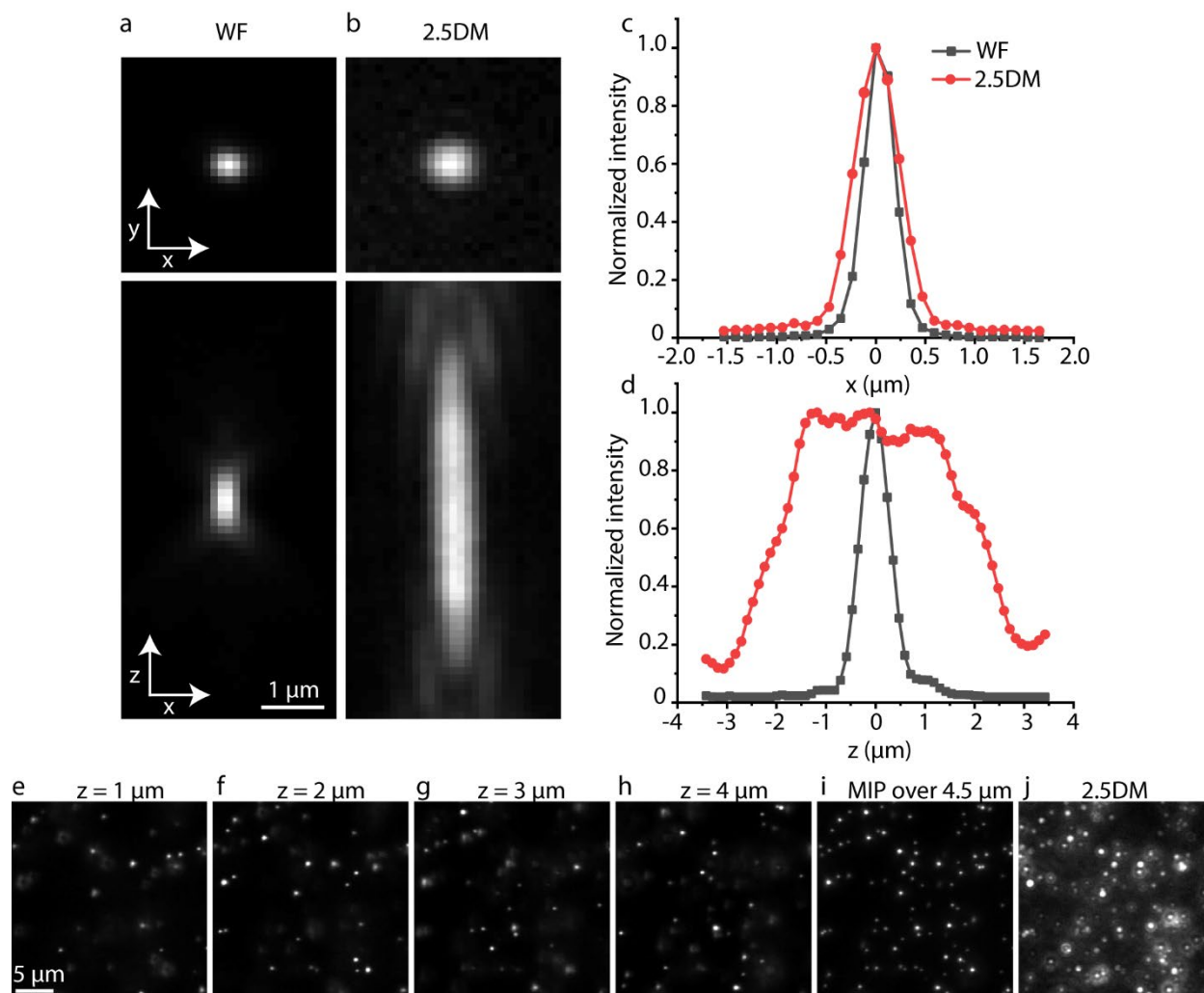


Figure 13 PSF measurement using 200 nm fluorescent beads. (a-b) Intensity distribution at the x - y and x - z planes with a clear aperture (WF) (a) and a 2.5D phase function (b). (c-d) Intensity profiles along the lateral (c) and axial (d) axis for WF (black) and 2.5DM (red). ¹⁰ Representative images of beads in 3D hydrogel at different image depth obtained by WF. (i) Image obtained by maximum intensity projection (MIP) of 3D image stack via WF. (j) Single-shot image by 2.5DM in the same area as WF.

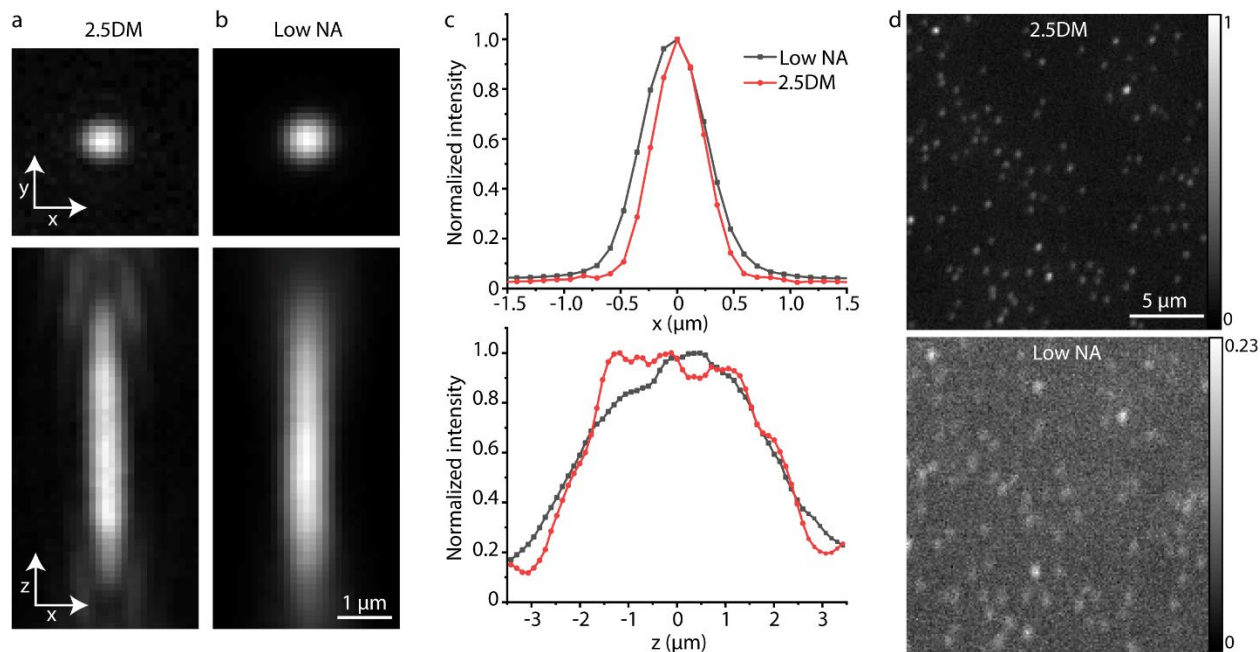


Figure 14 Experimental characterization of a low NA imaging system. (a-c) PSF measurements using 200 nm fluorescence beads. (a-b) Intensity distribution at the x-y and x-z planes by 2.5DM (a) and a lower NA system (b). (c) Lateral and axial intensity profiles of 2.5DM (red) and a lower NA system (black). (d) single-molecule images for the surface immobilized Atto647N-DNAs by 2.5DM and a lower NA system. All images were recorded at an excitation intensity of $\sim 100 \text{ W/cm}^2$ and an exposure time of 800 ms.

As we have described in Chapter 2, given the same extended DOF, 2.5DM shows advantages in minimizing the lateral resolution without scarifying the light throughput efficiency compared to a WF approach using a low NA objective lens. To address this, instead of using a low NA objective, which requires a separated detection module to maintain a similar effective pixel size as that obtained in a high NA imaging system, an iris was placed close to the SLM and the effective NA was adjusted by tuning the size of the pupil aperture at the conjugated BFP. We experimentally confirmed that the lateral FWHM of a low NA system gets broader than the FWHM of a 2.5DM (Figure 14c). In addition, we imaged surface immobilized single-molecule DNAs

labeled with Atto647N by 2.5DM and a low NA system under the same excitation intensity and exposure time (Figure 14d). one can see that a significant degradation in SNR occurred in the low NA system, hindering its application in single-molecule imaging.

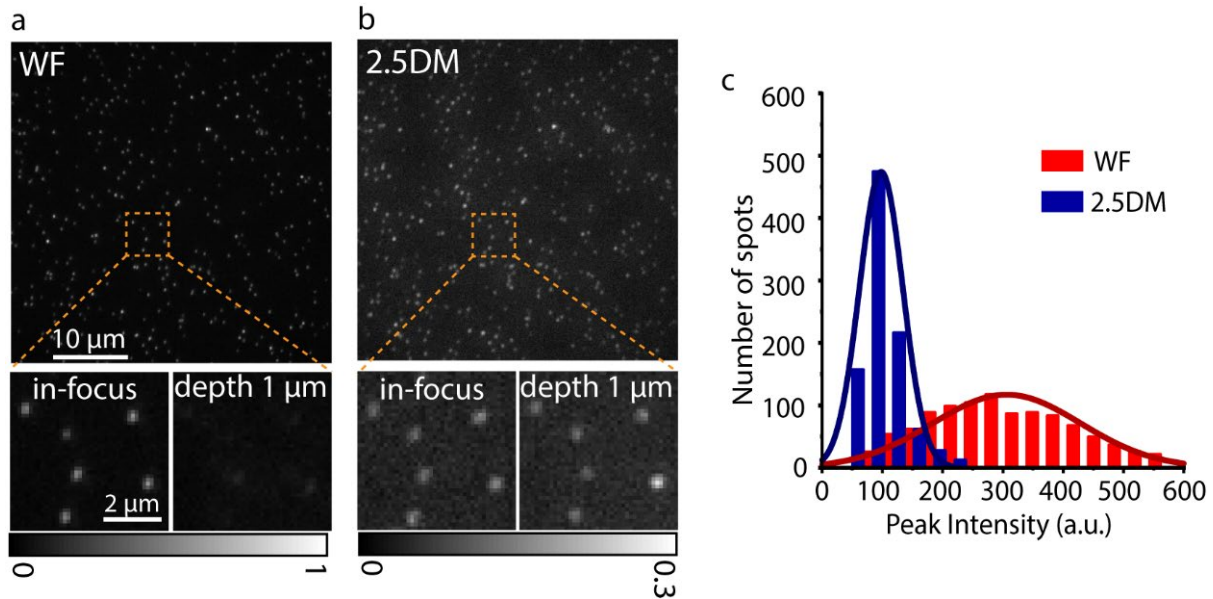


Figure 15 Single-molecule fluorescence intensity measurements. Surface immobilized DNAs were labeled with AlexaFluor647. (a-b) Single-molecule images by WF (a) and 2.5DM (b). Zoomed-in images from subregions marked by dashed squares at the focal plane and an imaging depth of 1 μm above the surface. Both were recorded at an excitation intensity of 100 W/cm² and an exposure time of 800 ms. (c) Peak intensity histograms of single-molecule spots for corresponding cases.

It has been noted that the peak intensity of the 2.5D images decreases as the axial depth of field increases. To quantitatively analyze the peak intensity reduction in the 2.5D imaging system, we examined the ratio of the peak intensity obtained with 2.5DM and WF (named Strehl ratio) by imaging single molecule DNAs labeled with Atto647N on a coverslip (Figure 15). Illumination intensity of 100 W/cm² and exposure time 800 ms were used for both of 2.5DM and WF. We recorded 20 images from different areas by WF (Figure 15a) and 2.5DM (Figure 15b) and One

may note that the shape of single-molecule spots is not isotropic along x - and y -axis attributed to the polarization effect arising from the linear polarized response of the SLM inserted at the conjugated BFP. However, the elongated PSF broadens the lateral width along the radial direction, resulting in more isotropic intensity distribution shown in Figure 15b.

To evaluate the peak intensity value of each single-molecule spot, we calculated the intensity difference between a peak value and averaged periphery background intensity around the spot for more than 1000 well-isolated single-molecule spots and a histogram of back-ground corrected peak intensity values for each spot was plotted (Figure 15c). It shows that a mean value of the peak intensity by the 2.5D imaging system was ~ 3 -fold lower than that with a clear aperture. The Strehl ratio of the peak intensity with 2.5DM and WF, indicates that for 2.5DM, in order to achieve a comparable peak intensity or SNR as that with a clear aperture, one needs to increase the exposure time by a factor of ~ 3 given the same illumination intensity.

3.3 Application of 2.5DM to smFISH

Transcription profiling in individual cells provides critical information, which could be easily averaged out by bulky measurements, i.e. qPCR and RNA-seq, as described in Chapter 1. One powerful method that provides accurate counts of mRNA copy numbers in individual cells is fluorescence in situ hybridization (FISH) technique followed by imaging analysis²⁴. Additionally, this method reveals subcellular spatial information of mRNA, as the localization of mRNA provides useful knowledge to understand the essential functionality of each mRNA species and its corresponding responsibility in specific protein generation. To precisely capture and analyze mRNA copy numbers, many methods have been studied and practically applied to single molecule

FISH imaging. One widely spread technique is to detect individual mRNA molecules using multiple singly labeled probes¹⁴. Owing to their great work, a flexible amount of DNA probes ranging from 1 to 96 can be designed and simultaneously bind to each individual mRNA. Figure 16 shows a schematic of multiple DNA probes labeled with fluorescent dyes binding to a specific mRNA as the sequence designed for. One may also need to note that the required number of probes for robust signal is also likely to relay on the target sequence¹⁴.

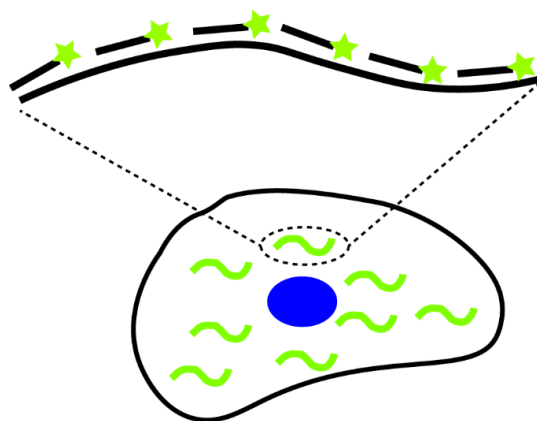


Figure 16 Schematic of mRNA with multiple probes labeled with fluorescent dyes.

3.3.1 Quantitative Imaging of mRNAs in Mammalian Cells by 2.5DM

To demonstrate the potential applications of 2.5DM in mRNA imaging, we performed single molecule mRNA FISH experiments in U2OS cells on a target mRNA *EEF2* (Eukaryotic Translation Elongation Factor 2), one of the high-abundance mRNAs in mammalian cells.⁹⁹ 32 probes labeled with AF647 were used to amplify the signal of each molecule. We first recorded a 3D stack of smFISH images by WF via serial z-scanning over a 5 μm thickness of the cell over a field of view (FOV) of $\sim 100 \mu\text{m} \times 100 \mu\text{m}$. 25 z-steps of images were obtained under epi-illumination at given experimental conditions, i.e., an exposure time of 400 ms per step and illumination intensity 100 W/cm^2 (Figure 17a). Maximum intensity projection (MIP) along the

axial direction was then performed on the 3D stack of images (Figure 17b) to reduce 3D information into a projected single image, which indicates the relative location of each mRNA in cells. For the same image area, we obtained a single snapshot image using 2.5DM with an exposure time of 1 s under the same illumination intensity as WF (Figure 17c). The colocalization of single-molecule spots obtained by 2.5DM and MIP showed that they corresponded well with each other (Figure 18). Transcription active sites were clearly observed in nuclei. Then an image applying average intensity projection (AIP) to the 3D stack of images was performed (Figure 17d) to mimic an approach of DOF extension (described in Chapter 1), that rapidly moves the focal plane along z-axis over a certain distance^{16, 40}, for example, by using an electronically tunable lens (ETL)^{33,96} to extend the effective PSF along z-axis without any mechanical movement.

To identify and count the copy number of single molecule mRNAs in individual cells, a Laplacian of Gaussian filter⁸² was applied to reduce the non-uniform background while sharpening the original image¹⁴. This two-step process is called LoG operation and the combined Laplacian and Gaussian functions can be expressed as:

$$LoG(x, y) = -\frac{1}{\pi\sigma^4} \left[1 - \frac{x^2+y^2}{2\sigma^2}\right] e^{-\frac{x^2+y^2}{2\sigma^2}} \quad (13)$$

where σ represents the bandwidth of the filter. An optimal bandwidth of the filter is determined based on the size of the observed spot and adjusted to optimize the signal to background ratio of the particles. After applying the LoG filter, noise cannot be removed completely in the filtered image, in particular, some dim non-specific binding spots may contribute to the mRNA counting, resulting in an overcounting problem. To enhance the accuracy of spot counting, a threshold value is necessitated. In general, the number of single molecule spots for all possible thresholds are counted, where a single molecule spot is defined as a connected component around the adjacent

pixels. Upon the curve of spots counted as a function of the threshold, a plateau is typically exhibited where the number of spots counted is less sensitive to the particular threshold value chosen within the plateau region and the accurate copy number of mRNAs can be determined. The uniformity of the illumination beam also plays a critical role in the accurate spot-finding. Compared to a Gaussian illumination, a more uniform illumination makes the spot-counting less sensitive to the threshold value. To do so, either more expanded beam is required to fill a uniform intensity distribution over the field of view, or some beam-shaping elements can be used to convert a Gaussian beam to a flat-top beam ⁸¹. Single molecule images were processed on a cell-by-cell basis, using a customized script written in MATLAB.

We then counted the copy number of mRNAs (*EEF2*) in a single cell (enclosed by a yellow dash polygon) under MIP and 2.5DM and the single molecule spots for all possible threshold values, normalized to 1 were plot (Figure 17e). Based on the spot-finding algorithm, a threshold value within a plateau region was chosen, showing a copy number of 617 mRNAs (by MIP) and 587 mRNAs (by 2.5DM) were detected, respectively, indicating a good agreement with each other. We also counted the copy number of mRNAs using a 3D stack, showing a copy number of 609, a almost same result as counter under MIP. Less than 5% decrease of the counted mRNAs in 2.5DM might be attributed to the overlapped spots (Figure 18) due to the broadening of the lateral width compared to WF and photobleaching during the image acquisition. To overcome the overlapping issues between adjacent spots, multi-spot fitting could be used. One may note that a longer plateau was observed with 2.5DM compared to MIP by WF, that may be explained by the intensity smoothness of the elongated PSF to single molecule spots located in different image depths with

variant peak intensities, whereas MIP is more likely to sharpen the nonuniformity of the emitting light from individual single-molecule spots located in different positions in the cell volume.

A custom-made Matlab script was used to calculate the SBR for three methods, i.e., MIP, 2.5DM and AIP, based on a series of criteria.¹⁰⁰ First, all images obtained were 2×2 binned, resulting in a pixel size of 118 nm. A minimal intensity value was subtracted from the raw image to obtain a background- corrected image. Then each well-isolated single-molecule spot was identified and analyzed in a 13×13 -pixel array around the central pixel of the spot. SBR was defined as I_s/I_b , where the corresponding background level for individual spots, represented by I_b , was calculated by the averaged intensity from the periphery region of the pixel array and the signal level, represented by I_s , was calculated by averaging the intensity from the central region around the peak intensity. The size of the central region was determined by lateral FWHM measurement of PSF as described in section 3.2. More than 100 well-separated single-molecule spots were used for the SBR analysis.

Since the effective PSF of AIP at the transverse plane is a superposition of in-focus spot and expanded out-of-focus as well, in other words, AIP image would collect not only in-focus fluorescence light but also out-of-focus background. As a result, AIP image showed the lowest SBR compared to MIP and 2.5DM (Figure 17f). Although the image obtained by 2.5DM compromised the SBR by a factor of 1.7 compared to MIP obtained by WF, it significantly improved the image acquisition rate by an order of magnitude with a single snapshot exposure, while still maintaining a high spatial resolution. In addition, SBR analysis indicated that 2.5DM showed higher SBR than obtained in AIP images (similar to rapidly moving the focal plane), which is particularly crucial for quantitative mRNA imaging with high abundance.

To further investigate whether WF and 2.5DM both could provide reliable mRNA counting given the same exposure time in total, we recorded a 2.5D image in a single snapshot exposure of 1s (Figure 19a) and a stack of images with WF for the same image area at shorter integration time of 40 ms per step where 25 z-steps of images were acquired with the total exposure time of 1s. Then a projected 2D image was obtained by MIP as shown in Figure 19b. A zoom area (surrounded by a white dash rectangular) indicated that the MIP image showed a remarkable SNR degradation and many single-molecule spots were overwhelmed by noise compared to the 2.5D image. We plotted the copy number of mRNAs as a function of all possible thresholds in the selected cell (surrounded by a yellow dash polygon) as shown in Figure 19c. Clearly, compared to 2.5DM, MIP with the total integration time of 1 s showed an exponentially decaying curve with no plateau observed due to the low SNR, making it difficult in reliable mRNAs counting. After applying a LoG filter to enhance the SNR and remove the slowly varying background, a threshold value 0.11, represented by the black dash line at the cross of two curves was chosen as the threshold value to determine the number of spots in two zoom images, where each distinct spot found was assigned to a random color (Figure 19d). The spots counted in 2.5D image well corresponded with those identified by eyes (zoomed image in Figure 19a). However, 4 out of 17 spots, overwhelmed by the background noise, were missed in the MIP image, which could result in severe error in quantitative measurements¹⁴, such as false-positive detection and/or missing single-molecule spots. A longer integration time in 2.5DM allowed one to collect more photons from fluorescence emission, leading to a higher SNR.

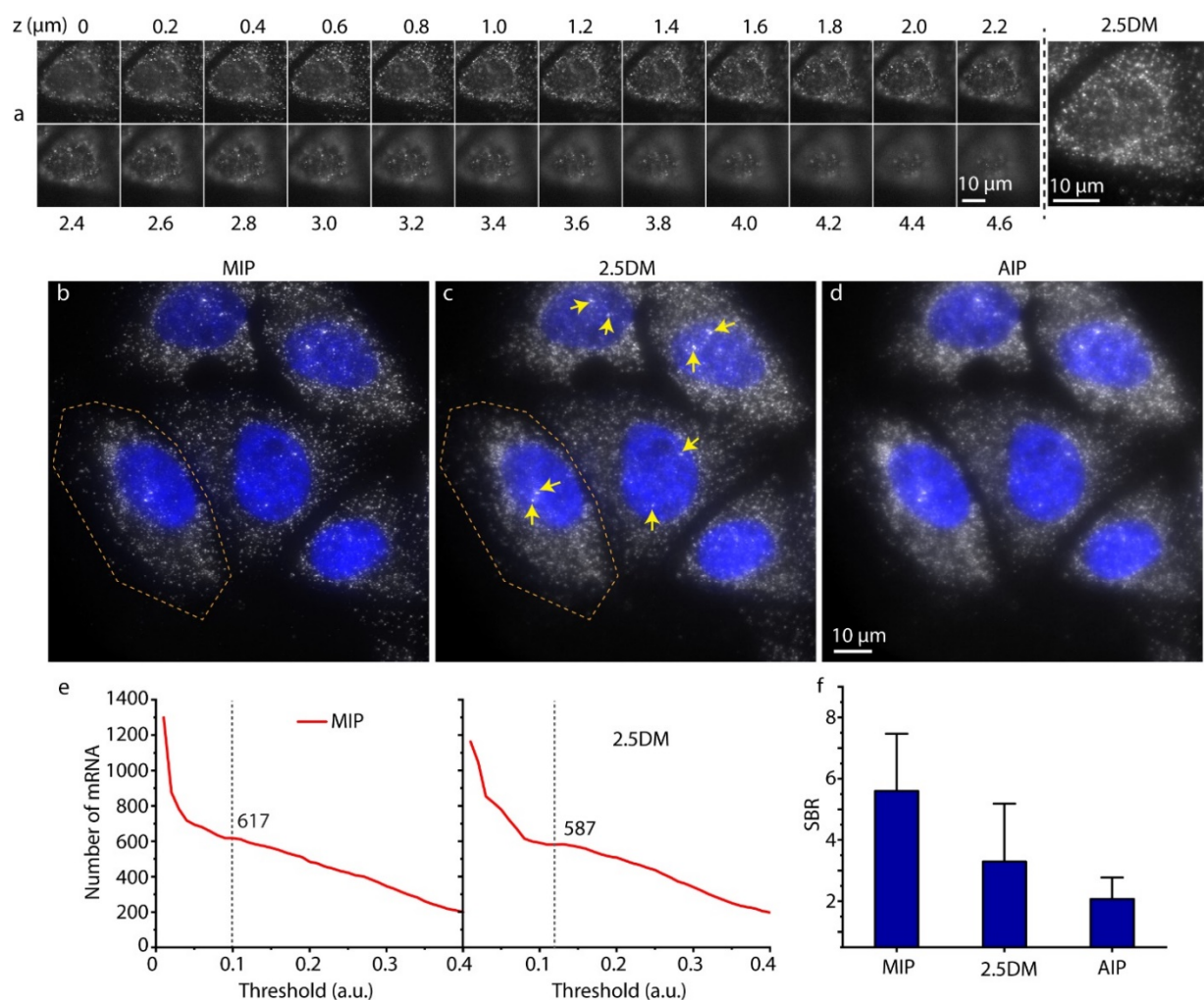


Figure 17 Single molecule mRNA FISH imaging of *EEF2* on U2OS cells using 2.5DM. (a) smFISH images of WF at different imaging depths (left) and the single-shot image of 2.5DM (right) in the same area. (b-d) Images obtained by (b) maximum intensity projection (MIP) (b), 2.5DM (c) and average intensity projection (AIP) (d) for the 3D cell volume. Nuclei were stained with DAPI shown in blue. Yellow arrows indicate active transcription sites. All images were recorded at an excitation intensity of ~100 W/cm² with an exposure time of 400 ms/step (WF) or 1 s (2.5DM). (e) Plots of the number of transcripts found in a single cell (surrounded by a yellow dashed polygon in (b) and (c)) as a function of threshold values for MIP and 2.5DM, where the vertical dashed lines indicate the optimal thresholds. (f) Signal to background ratio (SBR) for different techniques. The error bars denote the standard deviation from the mean value.

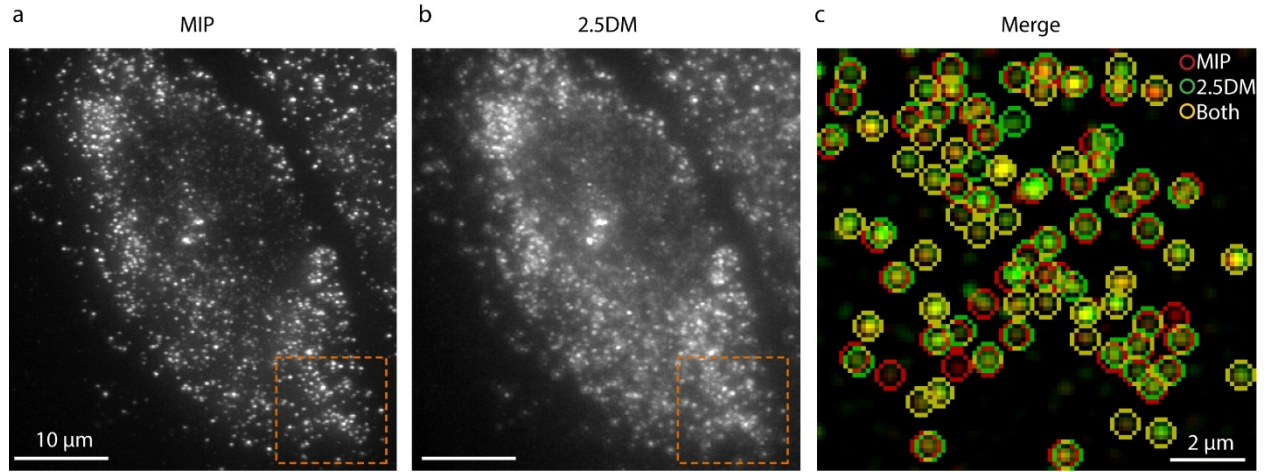


Figure 18 Co-localization of smFISH spots obtained by two methods. (a) Maximum intensity projection (MIP) and (b) 2.5DM imaging. (c) Color-coded circles representing identified mRNA molecules by MIP (red), 2.5D³¹ and both (yellow) from a merged zoomed-in image of subregions marked by dashed squares in (a) and (b).

To validate the capability of our approach for detecting different RNA species, we also performed single molecule mRNA FISH imaging of *TOP2A* (Topoisomerase 2-alpha) with 48 designed probes labeled with AF647 in U2OS cells at the same experimental conditions as the FISH imaging of *EEF2*, i.e., an exposure time of 400 ms per step for MIP (25 steps in total), and a single exposure of 1 s for 2.5DM with the epi-illumination intensity of $\sim 100 \text{ W/cm}^2$ over a volume of $\sim 100 \times 100 \times 5 \mu\text{m}^3$. The copy number of mRNAs (*TOP2A*) as a function of thresholds (normalized to 1) in a single cell (circled by yellow dash polygons) was plotted for two images, i.e., MIP image obtained by the 3D stack of images (Figure 20a) and 2.5D image (Figure 20b). The resulting copy number showed a good agreement with each other. Longer plateaus were observed for both MIP (Figure 20c) and 2.5DM (Figure 20d) than the case that 32 probes were used in *EEF2* FISH images, indicating much reliable counting with more numbers of probes, owing to the

brighter emission from extra probes which agrees with the analysis in the previous literature¹⁴. As a result, a variety of mRNA species with copy numbers ranging from low to high (up to ~ 600) in mammalian cells can be measured using 2.5DM with remarkably improved acquisition rate, providing a promising potential in faster high-throughput transcriptional profiling applications.

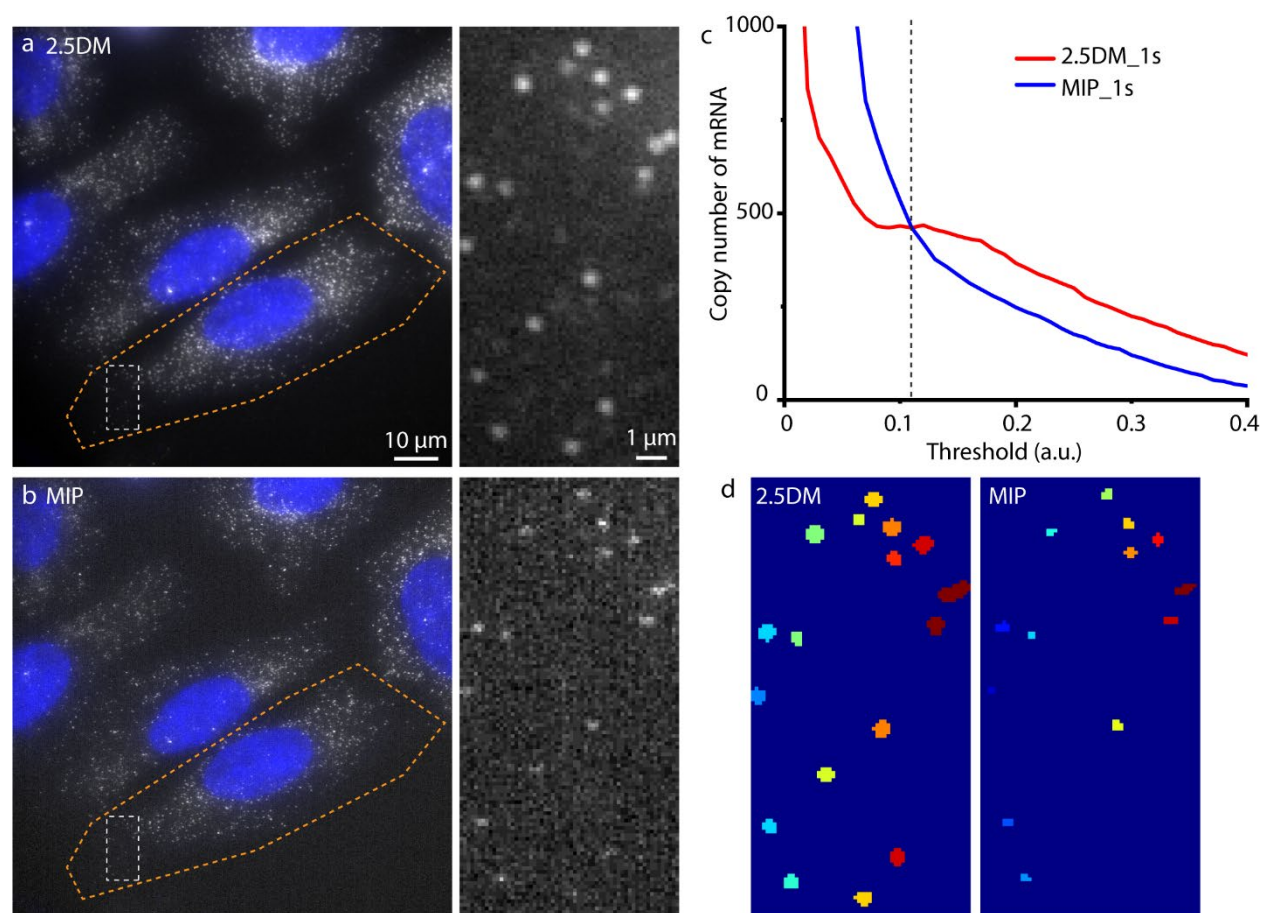


Figure 19 Quantification of mRNAs by 2.5DM and WF given the same exposure time. (a) Single exposure image by 2.5DM at exposure time 1 s, and a zoom image (right) surrounded by a white dash square. (b) Image by MIP of 25 z-steps via WF at exposure time 40 ms per frame and the corresponding zoom image (right). (c) Plots of number of spots found as a function of threshold values: 2.5DM (red) and MIP (blue). (d) Resulting images of two zoomed regions in (a) and (b) after applying a threshold value (the black dash line) in (c). Each distinct spot is assigned to a random color.

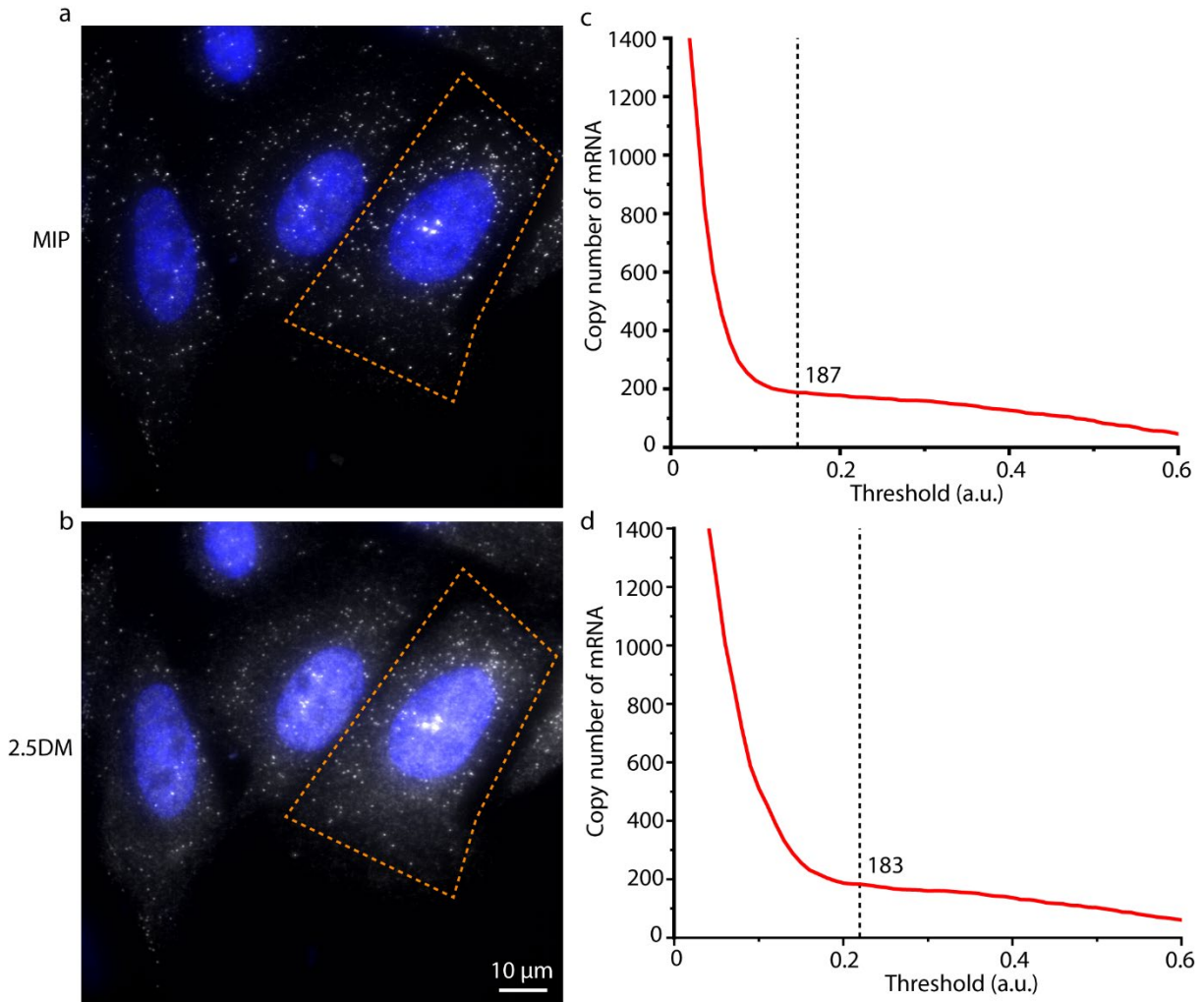


Figure 20 smFISH images of *TOP2A* labeled with AF647 on U2OS cells. (a-b) Images by MIP with WF (a) and single-shot image by 2.5DM (b). (c-d) Corresponding plots of the copy number of mRNAs identified in the selected cell (circled by a yellow polygon) as a function of all possible thresholds for MIP (c) and 2.5DM (d). Black dash lines indicate the optimal threshold value where the accurate copy number can be determined. 48 FISH probes labeled with AF647 were used and all images were recorded at an excitation intensity of $\sim 100 \text{ W/cm}^2$ with an exposure time of 400 ms/step (WF) or 1 s (2.5DM).

3.3.2 High-throughput smFISH Imaging by 2.5DM

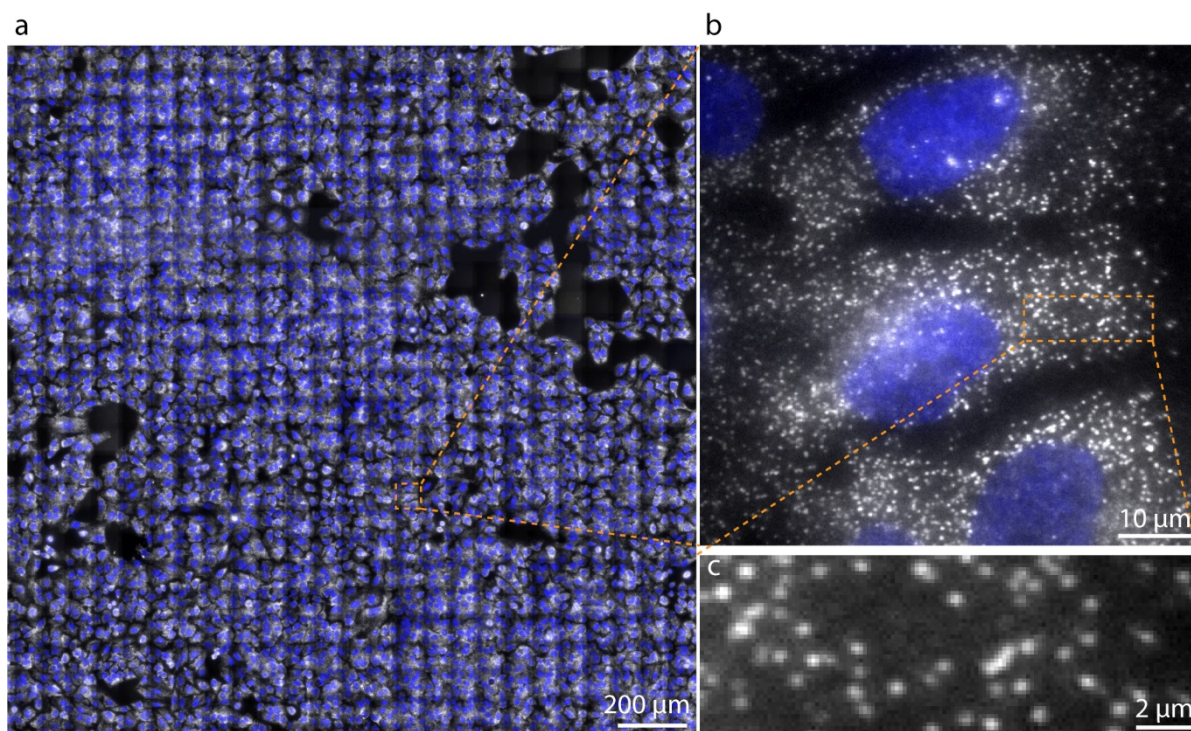


Figure 21 High-throughput smFISH imaging. (a) smFISH image of a $2 \times 2 \text{ mm}^2$ region of U2OS cells stained with DAPI (blue) and 32 probes labeled with AF647 for *EEF2*. 26×26 two-colored images with 20 % overlap between adjacent field of views were acquired under epi-illumination at exposure time of 600 ms for AF647 and 20 ms for DAPI. (b) Zoomed image of the rectangular region shown in (a) with an area of $65 \times 65 \text{ }\mu\text{m}^2$. (c) A further-zoomed region represented in (b).

To demonstrate the advantage of 2.5DM in performing high-throughput measurement, we obtained a smFISH image over an area of $\sim 2 \times 2 \text{ mm}^2$ with an imaging depth of $\sim 5 \text{ }\mu\text{m}$ in U2OS cells (Figure 21a). This image was composed of a grid of 26×26 smFISH images cross a FOV of $\sim 100 \times 100 \text{ }\mu\text{m}^2$ and a 20% overlap between two adjacent images was used to ensure a proper stitching. 676 images were obtained by 2.5DM within $\sim 9.2 \text{ min}$, whereas it required $\sim 64 \text{ min}$ in total for the same measurement performed by a traditional approach through serial z-scanning. The

individual mRNA molecules including transcription active sites were clearly observed in individual cells with a high SBR over the entire image area (Figure 21b and 21c). the total number of imaged cells was counted by imaging the nuclei using DAPI signal where cell nuclei were identified via setting a certain threshold value. Above a certain threshold value (normalized to 1), the intensity signal from the corresponding pixel was assigned to 1. The number of nuclei and the nucleus size were calculated from the pixels representing the intensity of 1. The total number of cells measured in the image area was ~2,830, leading to a throughput of 5.1 cells/s by 2.5DM, which was ~7.3-fold higher than the throughput by the conventional WF (0.7 cells/s). By implementing 2.5DM, the throughput efficiency was remarkably improved with a much-reduced light dose.

To analyze the copy number of mRNAs (*EEF2*) in individual cells quantitatively, well-isolated cells were segmented by defining cell boundaries based on a fact that the density of transcripts decreases significantly close to the edge of cells. Only cell boundaries that have one nucleus located in an enclosed boundary were defined as well-isolated ones and intentionally selected. After cells were properly segmented, we counted the copy number of mRNAs in each selected cell and plotted the number of mRNAs as a function of nucleus size calculated by DAPI signal (Figure 22). The averaged copy number of *EEF2* per U2OS cell was 505 ± 2.9 , represented by mean value \pm standard error of the mean. Statistical analysis indicated a positive linear correlation between the copy number of mRNAs and the nucleus size ($r = 0.71$) which showed a similar result as reported in the previous study about the relation between the mRNA abundance and cell volume and/or the nucleus size⁹⁹.

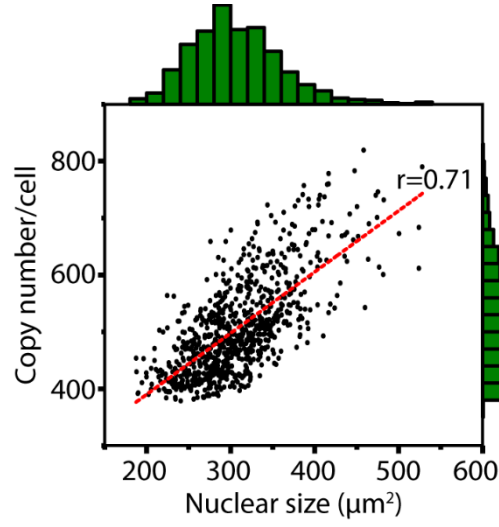


Figure 22 Copy number per cell as a function of nuclear size. The total number of cells analyzed was 814. The solid red line indicates the linear fit and r denotes a correlation coefficient.

To make the throughput of 2.5D imaging system more comparable to that of imaging flow cytometry (>200 cells/s), throughput efficiency for smFISH measurement need to be further improved. Many strategies can be used in the future work, which are mainly categorized by two different approaches: system level design and advanced smFISH techniques.

3.3.2.1 Improve Throughput via System Design

The total acquisition time required for a high-throughput smFISH measurement is composed of an area-independent time and an area-dependent time which can be expressed as $(\tau + t_{xy}) \times m^2$, where τ represents the exposure time per frame, t_{xy} denotes the settling time of a motorized stage and m^2 is the number of stitched images required for a specific image area. The area-dependent time can be further reduced by strategies based on the system design. Whereas it is difficult to reduce the settling time of a motorized stage due to the “stop-image” strategy, there are several approaches that could be applied to decrease m and τ . For instance, the imaging FOV

can be further expanded by replacing the current oil immersed objective lens (100×) with a 60×/NA1.4 oil or 60×/NA1.3 silicon objective lens. In a combination with fully used sCMOS pixels (2048×2048), the imaging FOV will be increased by 4-fold from $\sim 100 \times 100 \mu\text{m}^2$ to $\sim 200 \times 200 \mu\text{m}^2$. A flat-field illumination allows a smaller overlap when stitching imaging⁸¹, leading to a decreased m . 2.5DM showed a low photobleaching compared to a conventional microscope, which provides a possibility to further improve the throughput by increasing the frame rate under higher illumination intensity with significantly degrading the SNR. However, not only the amount of light dose but also the peak excitation intensity would play a critical role in determining the extend of photodamage of samples. Image post-processing based on computational algorithms such as using deep-learning¹⁰¹ or camera-related noise correction¹⁰² could be useful in lowering the exposure time and excitation intensity while improving the SNR.

3.3.2.2 Improve Throughput via Multiplexed Error-robust FISH

Many biology researchers are of interest to systems level questions, such as quantitatively understanding the interactions between different biological components. smFISH approach has remained limited in transcriptional profiling by the number of genes that can be simultaneously studied in single cells compared to alternative approach, genomics, which can systematically analyze all genes and proteins at a time with averaged information over numerous cells. Considering the advantage of smFISH approach in mapping the spatial context of specific mRNAs in their native environment, many advanced researches have allowed a simultaneous measurement of 10-30 distinct mRNA species in single cells^{21-23,103}. These approaches are using combinatorial labelling with either barcodes with spectrally resolved fluorophores or sequential hybridization.

However, to answer systems level questions, the measurement of hundreds to thousands of RNA species within a single cell is highly demanding for imaging-based approaches.

MERFISH has been proposed to substantially increase the number of RNA species that can be measured simultaneously in individual cells²⁵. This highly multiplexed smFISH method used combinatorial labeling and sequential hybridization with an error-robust encoding scheme as shown in Figure 23. Each mRNA species is encoded with a N bit binary barcode. During each hybridization round, the subset of RNAs that are encoded with 1 should read the emitting signal from the probes labeled with distinct fluorophores. The number of RNA species that can be addressed increases exponentially with the number of imaging rounds limited by the multiple distinct signals (N) used for labeling. Ideally, N rounds of hybridization would allow maximum number of $2^N - 1$ RNA species to be imaged. However, the detection reliability of RNA species rapidly decreases with the increasing number rounds of hybridization. To overcome this issue, MERFISH includes an error-robust encoding scheme in which only a subset of $2^N - 1$ binary words separated by a certain Hamming distance are used to encode RNA species. To reduce errors and enhance detection accuracy, the number of 1 bit should be kept relatively low: only 4 per a binary code word. In other words, each RNA species should be targeted with four sets of probes labelling with distinct fluorophores. Multiple singly labeled probes up to 96 can be used to enhance the fluorescence intensity in each imaging round.

This highly multiplexed imaging approach has shown significant improvement in analyzing large number of RNA species with preserving their spatial context¹⁰⁴. In combination with 2.5D imaging system and approaches of reducing area-dependent time, such as FOV expansion, flat-field illumination and computational-based image post-processing, the throughput

efficiency of smFISH imaging could be significantly improved, allowing a systematically study of image-based gene regulatory network under subcellular vision.

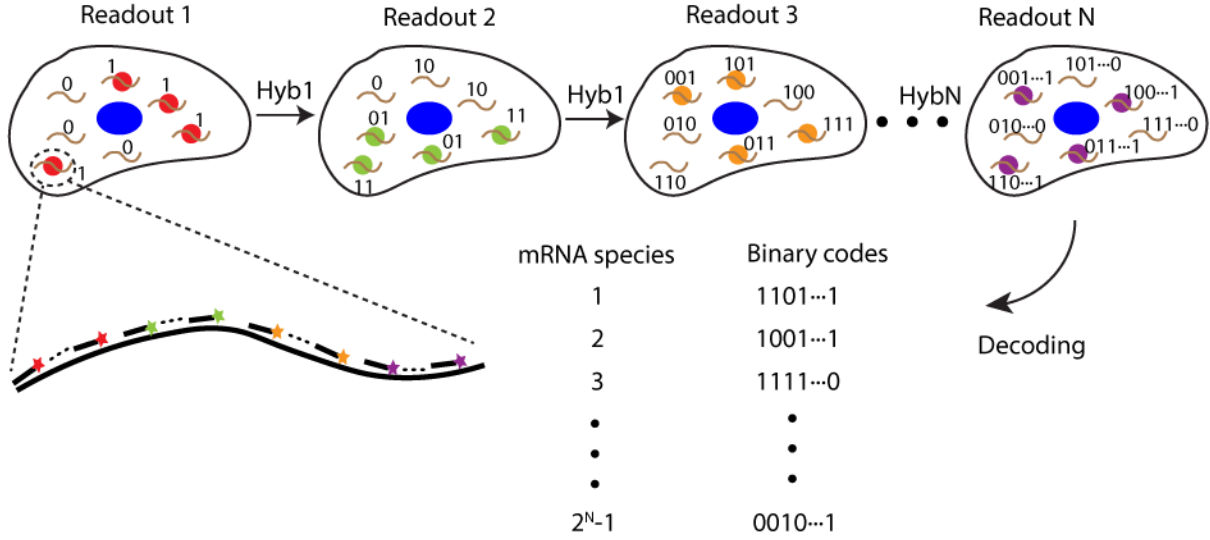


Figure 23 Scheme of highly multiplexed error-robust FISH (MERFISH) approach. Each RNA species is encoded with a N -bit binary word with a modified Hamming Distance 4 code. During each imaging round, the subset of RNAs that encode binary code 1 emit fluorescence signal. A different readout probe is used in each round hybridization and multiple singly labeled probes can be used to target each RNA to increase the SBR. Each binary code word contains a particular combination of four of N distinct readout signals. After N rounds of hybridization, every specific RNA species is decoded from the binary words measured during the experiment.

3.3.3 Multi-color smFISH Imaging by 2.5DM

To understand the functionality of a biological structure and its interaction with different proteins or biomolecules, multicolor fluorescence microscopy has shown its power in resolving the spatial relationship and temporal dynamics of subcellular components^{32,105-109} owing to the significant advances in optical instruments and detector design as well as the introduction of a

variety of new fluorophores spanning the entire visible spectral region. Different components of interest are labeled with distinctly colored probes in fixed and living cells and tissues. The colocalization between differently labeled entities is used as the indicator to study their potential interactions and to address many interesting biological questions. 3D imaging of whole cells with different color-coded components demands sequential image acquisition at different axial depths, suffering from multiple effects, for instance, out of focus molecule activation (photobleaching) and phototoxicity, especially in living cells. With 2.5DM, the volumetric information can be simultaneously recorded in a single exposure frame and projected as 2.5D images.

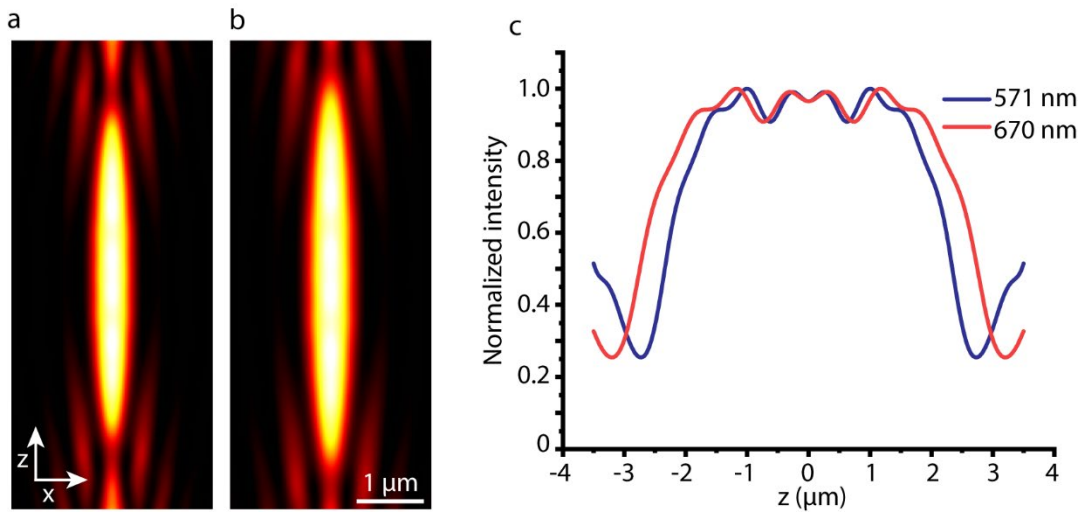


Figure 24 Focal responses of 2.5DM under two distinct wavelengths. (a-b) Intensity distribution of PSFs at the x - z plane generated by the same 2.5D phase pattern under two distinct wavelengths of 571 nm (a) and 670 nm (b) representing the peak emission wavelengths of Cy3B and AF647. (c) The corresponding intensity profiles of PSFs along the z -axis.

To elucidate the ability of multicolor imaging using 2.5DM, for instance dual color imaging, such as microtubules and mitochondria labeled with AF647 and Cy3B, respectively, a comparison of the intensity distribution at x - z plane of two distinct fluorophores with peak emission at 571 nm

for Cy3B and 670 nm for AF647, respectively, was shown in Figure 24a and 24b. In this simulation, the same phase pattern designed as described in Chapter 2 was applied for both wavelengths. As one can see from the intensity profiles along the axial direction (Figure 24c), axial FWHM of peak wavelength $\lambda = 670$ nm is ~ 5.5 μm and FWHM of peak wavelength $\lambda = 571$ nm was ~ 4.7 μm . With the same phase pattern, 2.5DM generated two elongated PSFs with the axial extension larger than 4.7 μm for two typical fluorophores, i.e., AF647 and Cy3B, which could well cover the thickness of a typical cell type, such as U2OS cells. In other words, two proteins labeled with these two distinct fluorophores can be immediately imaged through the cell volume by 2.5DM without rapidly switching the phase pattern of the SLM. which results in a further improvement in the image acquisition rate towards fast video-rate volumetric imaging systems.

To experimentally demonstrate the capability of 2.5DM in performing multi-color imaging, we first performed a 3D hydrogel fluorescent beads imaging to elucidate the ability of our 2.5D imaging system to an alternative color, which has the peak emission at the wavelength of 605 nm and could be effectively excited by 561 nm laser, since we have successfully validated the use of AF647 in smFISH mRNA imaging shown in section 3.3. To enhance the SBR of 3D beads image, a highly inclined epi-illumination was used to shrink the thickness of the excitation beam. First, a hydrogel beads image with a thickness of ~ 3 μm was recorded by sequentially z-scanning through the volume and then projected onto 2D image by MIP as shown in Figure 25a. A single exposure image was then obtained by 2.5DM at the same image area shown in Figure 25b. Figure 25c showed a representative frame of 3D stack at the imaging depth of $2\mu\text{m}$ above the surface of the coverslip. From the zoom images (Figure 25d-25f), one can clearly see that the spots observed by 2.5DM corresponded very well with those obtained by MIP of the 3D stack. one may also note

that more spots were displayed on the 2.5D image, which could result from the longer axial extension of the PSF ($> 3 \mu\text{m}$) generated by the 2.5D imaging system than the recorded image volume.

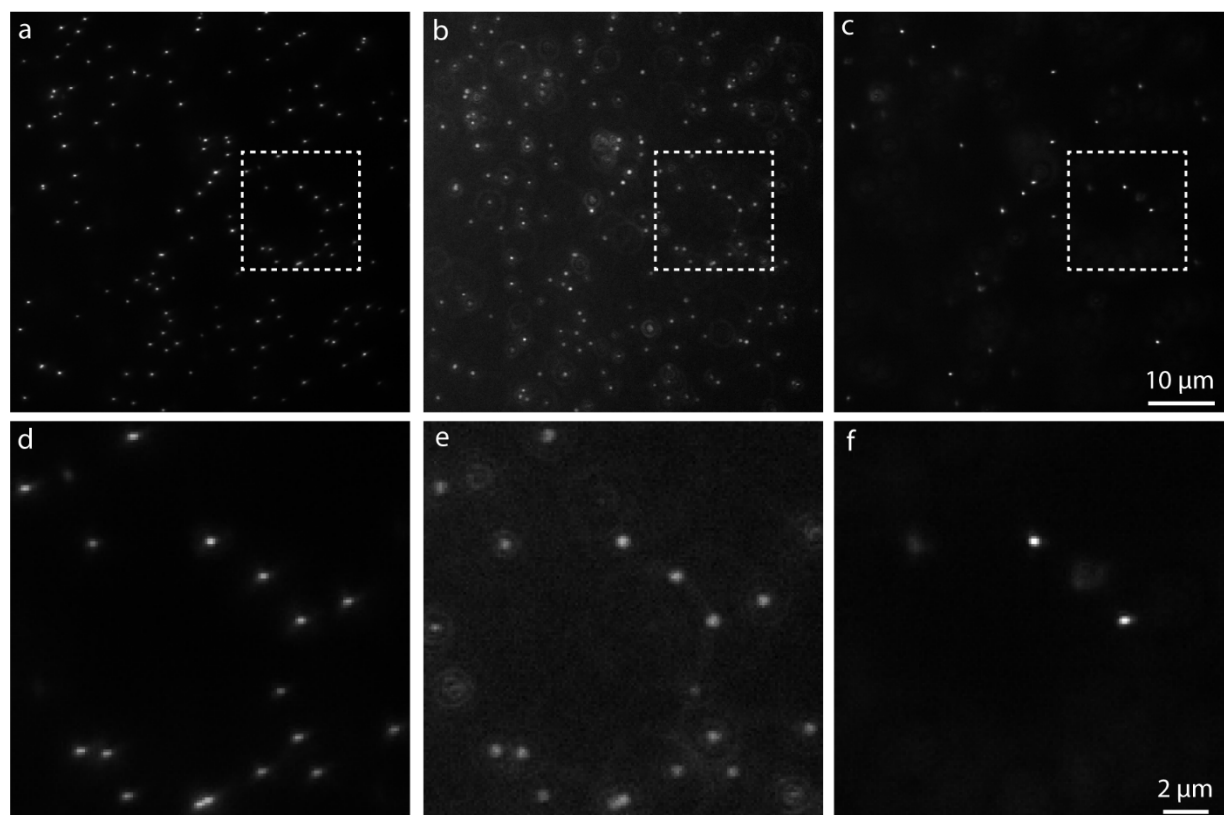


Figure 25 3D hydrogel fluorescence beads images with the peak emission wavelength 605 nm. (a) 3D stack of images recorded and projected by MIP. (b) Single exposure image using 2.5DM at the same image area. (c) A representative frame of the 3D stack at the image depth of $2 \mu\text{m}$ above the image surface. (d)-(f) Corresponding zoom images of white dash square regions in (a)-(c), respectively. The fluorescence beads were excited by 561 nm laser.

Then we further demonstrated the capability of 2.5DM in measuring different mRNA species by labeling two distinct mRNAs, i.e., *EEF2* with Cy3B and *TOP2A* with AF647, respectively, in the same mammalian cells (U2OS). Two organic dyes were excited by two lasers

at wavelengths of 532 nm (Cy3B) and 638 nm (AF647) with an epi-illumination intensity of 100 W/cm² at an exposure time of 600 ms. As one can see, smFISH images of *EEF2* (Figure 26a) and *TOP2A* (Figure 26b) were clearly observed over the entire cell volume. A superposition of two distinct mRNA images (Figure 26c and 26d) showed the colocalization of each mRNA molecule with high SNR. By performing multi-color imaging using 2.5DM, the throughput efficiency would be further improved.

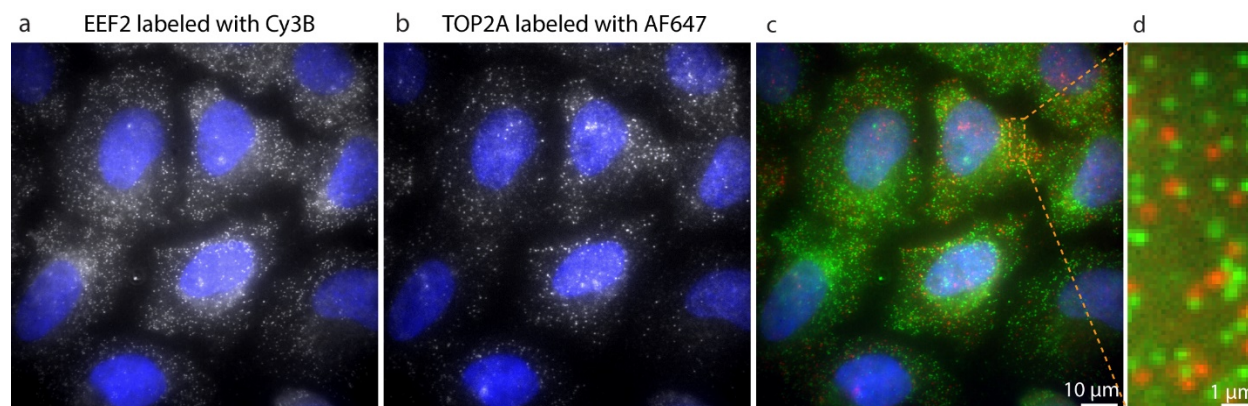


Figure 26 Two color smFISH imaging on *EEF2* and *TOP2A* on U2OS cells. (a-c) 2.5D images of *EEF2* labeled with Cy3B (a), *TOP2A* labeled with AF647 and overlapped image of two channels: green represents Cy3B and red represents AF647. An illumination intensity of ~ 100 W/cm² at an exposure time of 600 ms was used. (d) Zoomed image for the rectangular region shown in (c).

3.4 Immunofluorescence Imaging by 2.5DM

Immunofluorescence imaging is a powerful technique in biological research to visualize the distribution of the target molecules and proteins, even intermediate-sized filaments¹¹⁰, using the specificity of antibodies to their antigen to probe fluorescent dyes to specific biomolecule targets within a cell. Immunofluorescence can also be used in combination with other, non-

antibody methods of fluorescent staining to study the correlation between different functional structures in subcellular levels. However, a limitation of immunofluorescence is photobleaching, resulting in the loss of activity, like most of fluorescence techniques. This drawback generally is controlled by reducing the illumination intensity or exposure time of the fluorescent dyes under the light, and by employing more robust fluorophores less prone to bleaching. As demonstrated in smFISH imaging, 2.5DM technique can be implemented to immunofluorescence imaging as well to obtain the distribution of the specific protein targeted within a cell in a single exposure image, remarkably reducing the light dose exposed onto the sample.

To experimentally demonstrate the capability of 2.5DM in visualizing the distribution of proteins, we employed 2.5DM for imaging Vimentin in U2OS cells. Vimentin was stained with antibodies labeled with AF647. We first recorded a 3D stack of images (25 steps) with a sample thickness of 5 μm across a field of view of $\sim 100 \times 100 \mu\text{m}^2$ with WF at an illumination intensity of 12 W/cm^2 and an exposure time of 10 ms per step. 2D projected images by MIP (Figure 27a), AIP (Figure 27b) and a single frame of image at the depth of 2 μm (Figure 27c) were obtained based on the 3D stack. Then a single snapshot image by 2.5DM was obtained at an exposure time of 30 ms (Figure 27d), indicating an improvement in image acquisition rate by ~ 8 -fold. As one can expect, the image obtained by 2.5DM showed a higher contrast compared to the AIP image. Particularly, Better spatial connection was exhibited in the 2.5D image whereas the MIP image displayed discontinuities which may be attributed to the enhancement of MIP to intensity variation from different imaging planes¹¹. This discontinuity may lead to inappropriate rendering to the distribution of target proteins. However, 2.5D image showed worse SNR/SBR than that by MIP

as expected, owing to the degradation of the lateral resolution. This problem can be remarkably mitigated by the advancement of image post-processing techniques¹¹²⁻¹¹⁴.

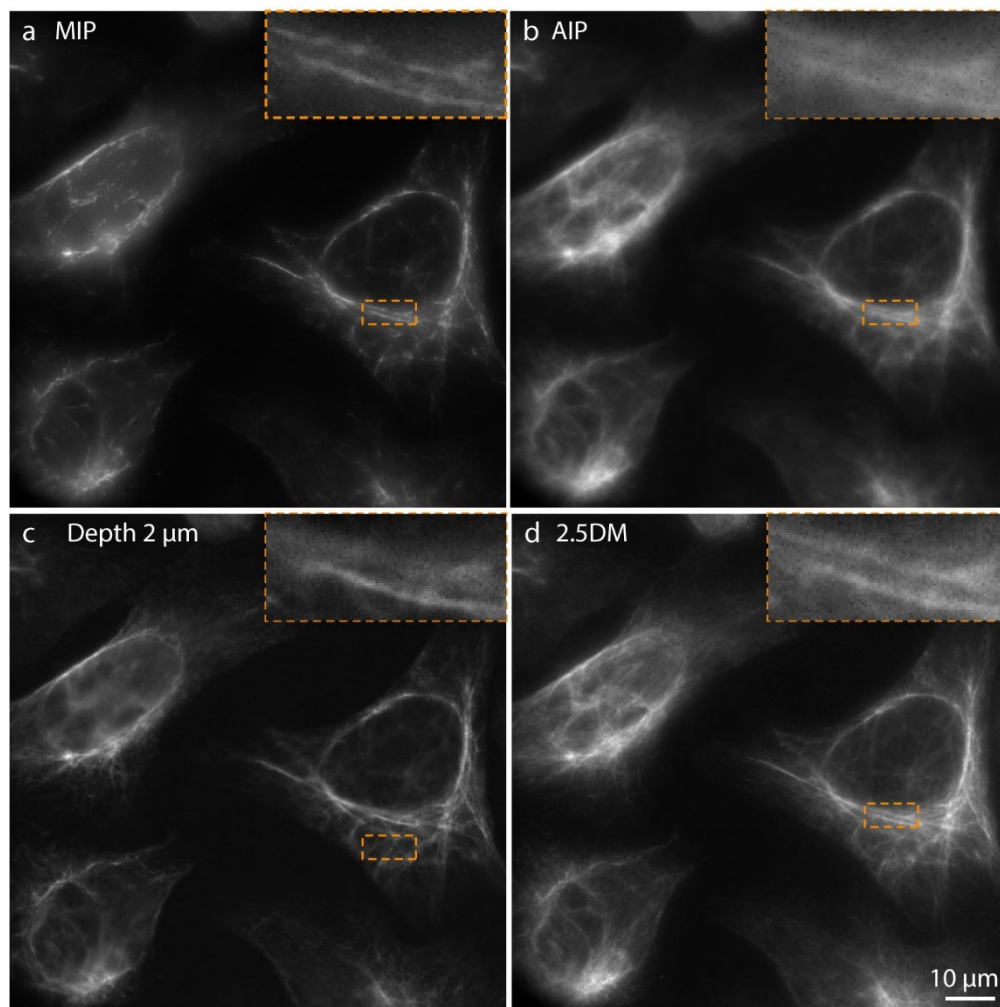


Figure 27 Immunofluorescence imaging of vimentin by 2.5DM. (a-c) Images obtained by MIP (a), AIP (b) with 25 z-steps (10 ms/step) in an imaging volume of $\sim 100 \times 100 \times 5 \mu\text{m}^3$ and a representative frame at the depth of $2 \mu\text{m}$ above the surface (c). (d) A single-shot image by 2.5DM at an exposure time of 30 ms. All images were taken with an excitation intensity of $\sim 12 \text{ W/cm}^2$.

Since we were using a sCMOS camera in the experiments because it exhibits several advances in imaging performances including high quantum efficiency, large field of view and

rapid frame rates, providing a perfect balance in sensitive, speed and spatial resolution, which is in particular suitable for fast, high-throughput imaging. However, compared to charge coupled devices (CCD) and electron-multiplying CCD (EMCCD) cameras¹¹⁵, the working principle of sCMOS cameras, i.e. parallel charge to voltage conversion and different responsivity of individual pixels, leads to an extra pattern noise even without the detected photons, and readout noise. The extra noise, in combination with readout noise and photon shot noise, can deteriorate the image quality, and induce artificial bright pixels, in particular, for photon-limited applications¹¹⁶. An automatic correction of sCMOS-related noise with preserving the fine features of the raw images has been reported recently to improve the image quality with reduced light exposure time, which could also facilitate fast video-rate imaging for live-cell applications.

Based on the mechanisms of the noise source generation, the acquisition in each pixel of a sCMOS camera can be categorized by three terms: fixed-pattern noise generated in different pixels given the same number of incident photons; a combination of readout noise and photon shot noise; and offset background in the absence of light exposure. The fixed pattern noise can be estimated by a one-time camera calibration. The photon shot noise and readout noise can be considered as a sum of two independent random variables, which can be practically approximated by a Gaussian distribution¹¹⁷. An accurate assessment of the noise variance is essential to retain the fidelity of the reconstruction of the denoising image. By taking advantage of the knowledge of the optical system, i.e., numerical aperture, emission wavelength and pixel size, a cut-off frequency determined by the optical transfer function (OTF) can be used to evaluate the noise-related pixel fluctuation above the cut-off frequency. To this end, a high-pass filter can be used to filter out the signal from the sample with noise-only contribution.

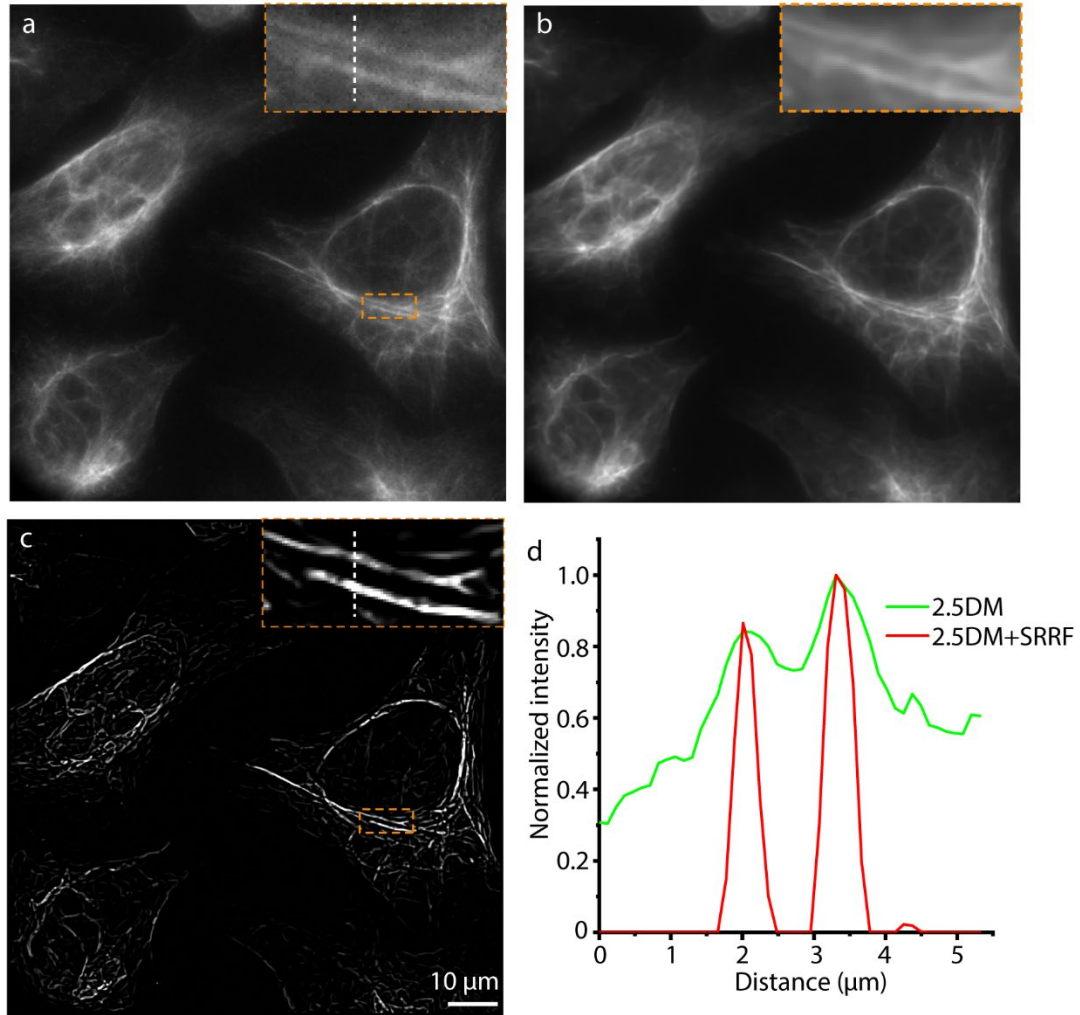


Figure 28 Post-processing of 2.5D image based on SRRF. (a-c) Vimentin images in U2OS cells obtained by 2.5DM (a), after sCMOS-related noise correction (b) and after reconstruction by NanoJ-SRRF (c). (d) Line profiles along the dashed lines of inset zoom-in regions in (a), (c).

We applied this automatic noise-correction algorithm to the vimentin image obtained by 2.5DM, the noise fluctuation was diminished (Figure 28b) compared to the raw image (Figure 28a), resulting in a much smoother background whereas without significantly reducing the background level. We further adopted a computation-based super-resolution imaging method, i.e. super-

resolution radial fluctuation (SRRF)¹¹⁸, which has been developed in ImageJ as a freely available

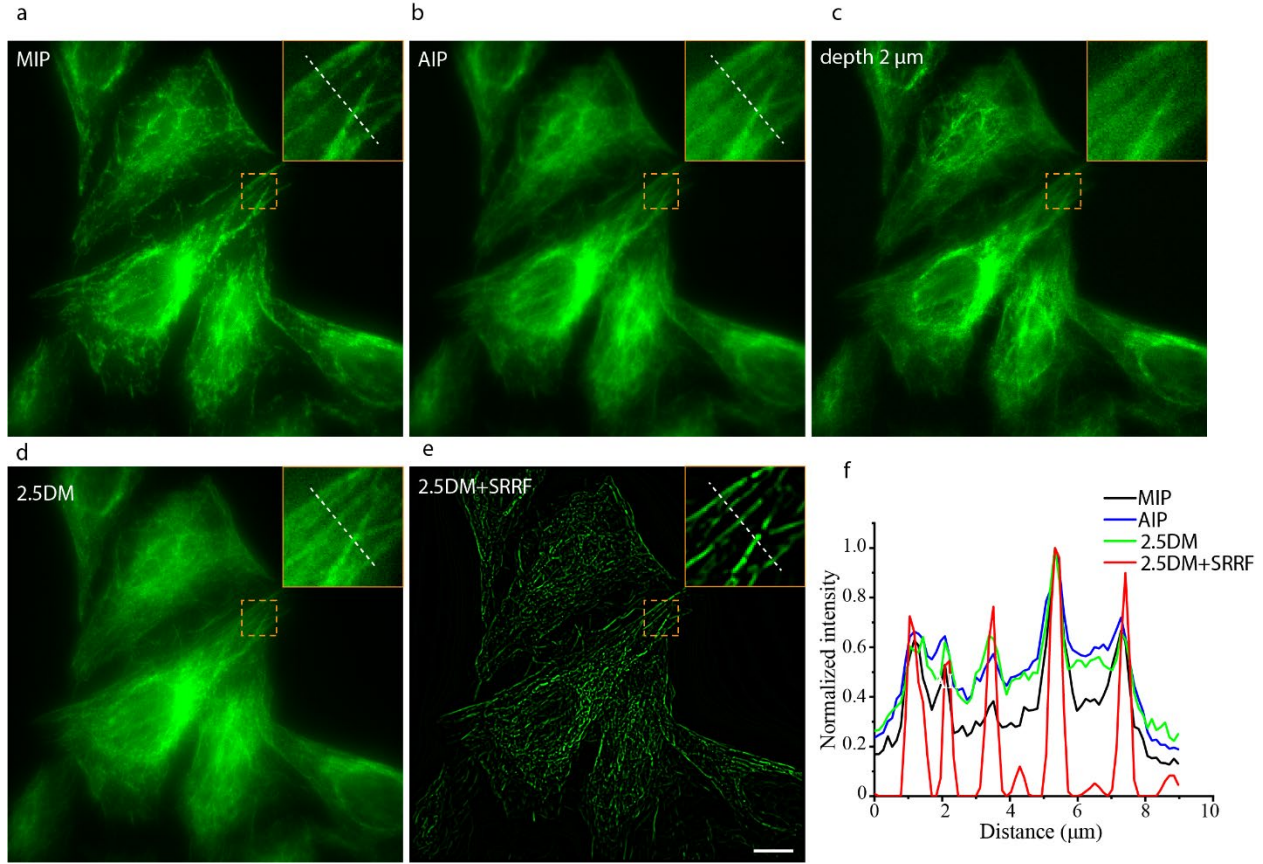


Figure 29 Immunofluorescence imaging of microtubules labeled with AF488 by 2.5DM. (a-c) Images obtained by MIP (a), AIP (b) and a representative frame at the depth of 2 μm above the surface (c) of 3D stack at an exposure time of 10 ms/step. (d) A single-shot image by 2.5DM at an exposure time of 30 ms. (e) An SRRF image using 2.5D image. (f) Line profiles along the dashed lines of subregions surrounded by squares in (a), (b), (d) and (e). All images were taken with an illumination intensity of ~12 W/cm².

open-source plugin (NanoJ-SRRF)¹¹⁸, to the smoothed image (Figure 28b). In this method, the degree of local gradient convergence is calculated over the entire field of view on a sub-pixel basis. Compared to the directly detected image which is comprised of radially symmetric points with diffraction-limited resolution, the calculation of radially results in a remarkably improved spatial

resolution. In addition, by weighting the radially map with intensity and gradient magnitudes, fake positives associated with non-fluorophore can be further filtered, enabling a high-resolution image without sacrificing SNR (Figure 28c). As shown in Figure 28d, SRRF image exhibited a remarkable improvement in the spatial resolution as well as the SBR, validating its compatibility with 2.5D images. We also confirmed 2.5D approach for imaging other protein types such as microtubules labeled with AlexaFluor 488 (Figure 29).

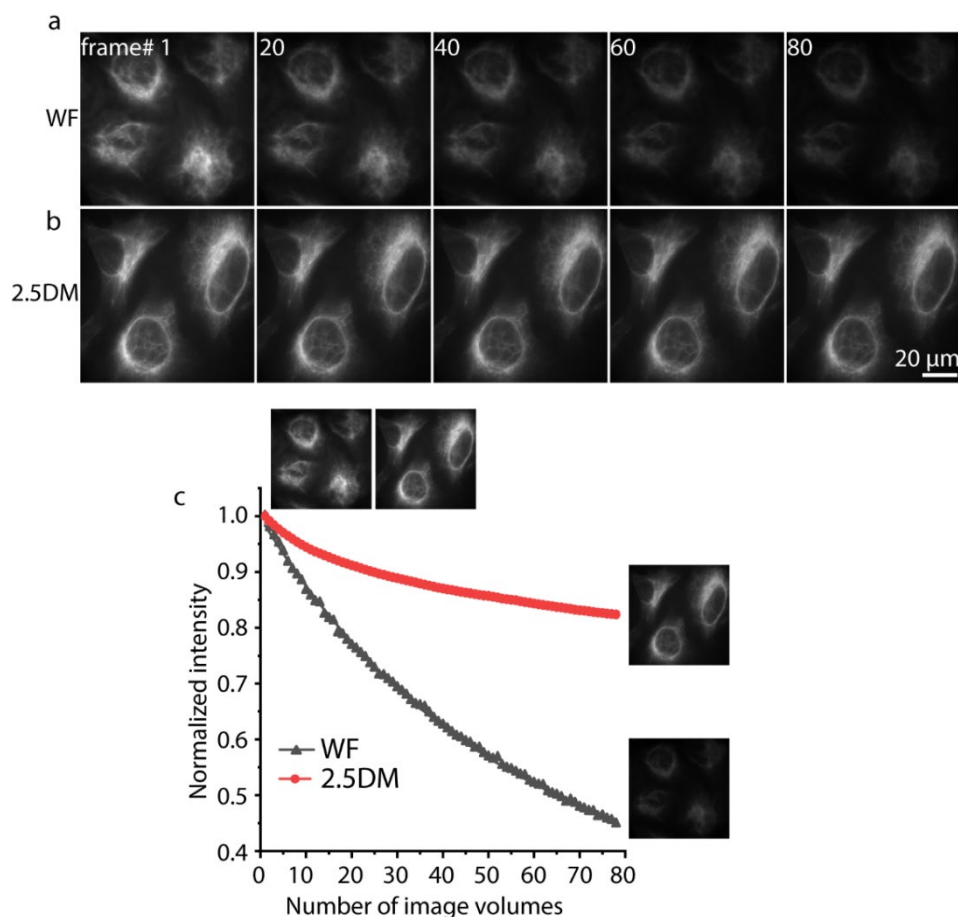


Figure 30 Measurement of the photobleaching effect on 2.5DM and WF. (a-b) Vimentin images obtained by WF (a) and 2.5DM (b) after specified numbers of image volumes. (c) Photobleaching traces of WF (black) and 2.5DM (red) as a function of the number of image volumes. All images were taken under epi-illumination with an excitation intensity of $\sim 100 \text{ W/cm}^2$.

To confirm the capability of 2.5DM in reducing the light exposure time and quantify the extent of photobleaching, we measured the fluorescence images of Vimentin repeatedly over a 3D volume ($100 \times 100 \times 5 \mu\text{m}^3$) by WF (10 ms/frame) and 2.5DM in a single exposure of 30 ms in different image areas. The excitation intensity was 100 W/cm^2 for both cases. More than 80 image volumes in each field of view were continuously recorded to trace the fluorescence signal evolution (Figure 30a and 30b). Excitation beam was turned off between volumes to minimize unnecessary light exposure. A constant background was subtracted from the raw images and the intensity at each time point was calculated by summing up intensity values from each pixel. We plotted the photobleaching curves of WF and 2.5DM and fitted them with a single exponential decay function (Figure 30c). As one can clearly see that 2.5DM displayed a 1.5-fold lower photobleaching rate than that observed in WF, confirming a lower light dose (8.3-fold) is necessitated in 2.5DM, which leads to a reduced photodamage by implementing 2.5DM.

CHAPTER 4 2.5DM WITH IMPROVED DETECTION EFFICIENCY AND DEPTH ABERRATION CORRECTION

4.1 Overview

In our current SLM-based 2.5D imaging system, the light transmission efficiency in the detection path is ~41%. Due to a random polarization of fluorescence, ~50% of the emission light is inevitably discarded by passing through a polarized beam splitter (PBS) or linear polarizer before it is modulated by a SLM, which inherently responds only to a certain linearly polarized light. The fluorescence light polarized in any other direction is not able to be modulated in this scheme, which in turn leads to undesired cross modulation between wavefront and polarization modulation. While the transmission efficiency can be improved by simply replacing the SLM with a well-designed passive phase plate³⁰, it requires a specific design for fluorophores emitting at different wavelengths. Such as for multi-color imaging. In addition, mechanically switching phase plates not only reduce the image acquisition rate, but may also lead to the system misalignment, which in turn reduces the resolution of the imaging system.

To overcome the loss issue due to a SLM, a variety of approaches have been suggested for polarization-insensitive beam shaping or specific mode generation by a SLM⁵¹⁻⁵⁵. For instance, by separating two orthogonal polarized beams via a birefringent beam displacer⁵² or a polarized beam splitter^{53,54}, one component that cannot be modulated by the SLM would first converted into the orthogonal polarization using a half-wave plate before reaching onto the SLM (Figure 31a). Two phase-modulated components are then recombined in a common path with a spatial deviation from the incident light. A double-pass SLM configuration^{51,55} has been reported to achieve 3D-STED beam generation, in which two orthogonal polarized components share the same optical path and

their wavefront is modulated by two exactly same phase patterns located at two adjacent areas of a SLM (Figure 31b).

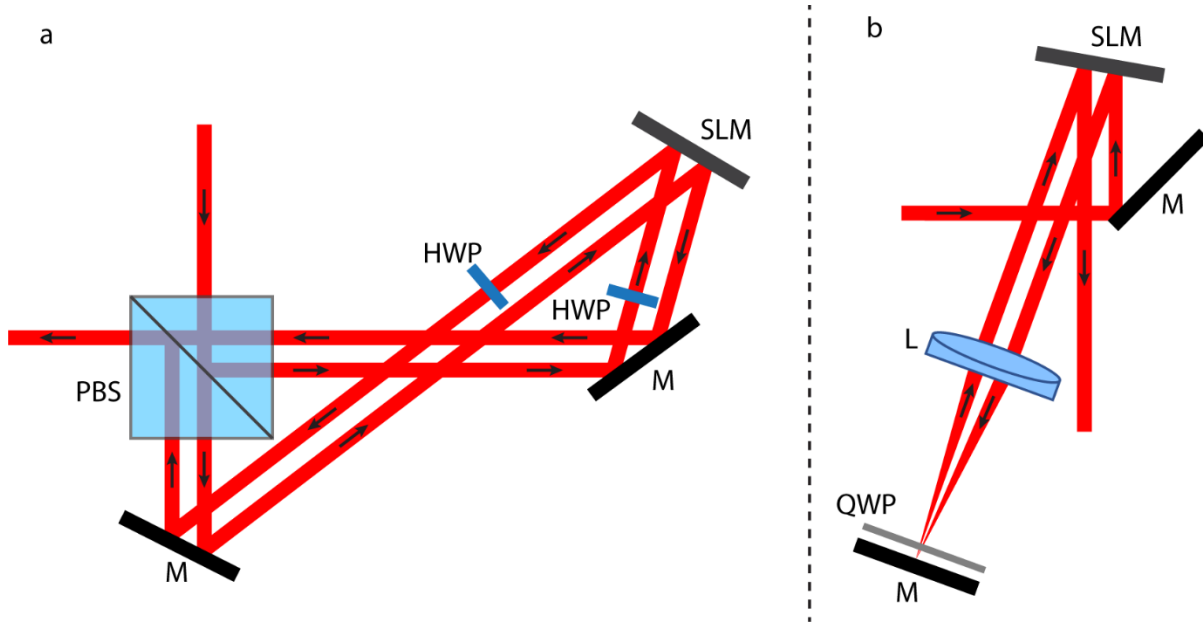


Figure 31 Schematics of two polarization non-sensitive SLMs. (a) Polarization non-sensitive SLM by separating two orthogonal polarized beams via a polarized beam splitter (PBS) and converting non-responded component by 90 via a half-waveplate (HWP). (b) Double pass configuration in which two orthogonal polarized components are exchanged by double-passing a quarter-waveplate (QWP). L, lenses; M, mirrors; SLM, spatial light modulator.

To date, these techniques have only been successfully demonstrated for specific beam generation in the excitation path of fluorescence microscopy. Extended DOF via PSF engineering still suffers significantly light loss when a SLM is used to encode the wavefront of the emission light^{38,56}. To mitigate this problem, several approaches have been proposed via splitting two orthogonal polarized components by a polarized beam splitter, modulating the wavefront of each component independently and finally imaging them into different areas of a camera^{57,58}. While the

SLM in these methods fully utilizes the fluorescence light, SNR of each image is still inherently limited because of the physical separation of two polarizations. A deformable mirror¹³, in particular, continuous surface type, could be used as an alternative for improving light efficiency³⁶ owing to its reflective nature. However, the control mechanism of each actuator under the mirror makes it impractical in producing a phase pattern with sharp variation, i.e., binary phase as that of 2.5DM. Some coupling effects are also inevitable arising from the position control of adjacent actuators. Compared to a liquid crystal SLM, DM has much smaller number of actuators, ranging from several tens to hundreds, which greatly limited its application for producing more sophisticated wavefronts in PSF engineering methods.

To image many thick biological samples, it's crucial to manage and properly correct aberrations that can reduce the resolution and the SBR of images. As the image plane moves deeper into the sample, the image quality degrades due to the depth aberration arising from the refractive index mismatch⁴⁹ between the sample and the immersion medium of the objective lens and due to sample-induced aberrations⁵⁰ arising from refractive index variations of the sample itself. Among these aberrations, depth aberration is dominant in many samples^{49,119}. One solution to remedy this problem is to use glycerol¹²⁰, silicone or water immersion objectives¹²¹ to minimize the refractive index difference between the sample and the immersion fluid. It can also be effectively compensated by correcting the deformed wavefront at the BFP of the objective using adaptive optics, such as DMs⁴⁹ or SLMs. Therefore, it is worthy to study how to improve the detection efficiency of a SLM-based imaging system while maintaining its extra degree of freedom in aberration correction.

In this chapter, we presented a SLM-based polarization-insensitive 2.5DM that could substantially improve the fluorescence transmission efficiency. This could play a crucial role for photon-limited applications and live cell imaging with reduced photobleaching or phototoxicity. Furthermore, we demonstrated the potential capability of an SLM-based imaging system in correcting depth aberration and aberration induced by optical components as well. We also showed that with the implementation of SLM, our 2.5DM could be used for imaging thicker samples with high fidelity of volumetric information while requiring much less z -scanning steps.

4.2 Polarization-insensitive 2.5DM

4.2.1 Microscope Design

Figure 32 showed the experimental setup of 2.5D microscope in which two orthogonal polarized detection lights were encoded at the conjugated BFP of the objective lens through a double-pass configuration described previously¹⁵ for 3D-donut beam generation. The excitation laser beam (638 nm, 405 nm, Cobolt) exiting from the fiber (P5-405BPM-FC-2, Thorlabs) output is collimated by a lens (L1, $f = 80$ mm) and further expanded by a telescope (L2, $f = 50$ mm; L3, $f = 150$ mm) to obtain a uniform epi-illumination. The beam passing through a lens (L4, $f = 400$ mm), is reflected by a dichroic mirror (DM1, Di03-R405/488/532/635-t1-25×36, Semrock) and delivered to the sample through an objective (UPlanSApo, 100×/1.4, Olympus). Fluorescence emission is filter by a multiband emission filter (FF01-446/523/600/677, Semrock) and an intermediate image plane is generated at the focal plane of a tube lens (T, $f = 180$ mm). A 1:1 4f system composed of two lenses (L5, $f = 200$ mm; L7, $f = 200$ mm) relays the intermediate image on a scientific complementary metal oxide semiconductor (sCMOS) camera (Zyla 4.2 Plus, Andor),

giving an image magnification of $100\times$. A knife-edge mirror is used to redirect the detection light onto the SLM at a shallow incidence angle (within $\pm 5^\circ$) to ensure proper performance of the SLM in a compact configuration. When light is first incident on the SLM, the wavefront of the horizontal component of the input polarization is modulated while the vertical polarized component remains unmodified. The polarization of both components is exchanged by double-passing an achromatic quarter waveplate (AQWP10M-580, Thorlabs) oriented at 45° . The pupil aperture is reimaged onto the conjugated BFP where the SLM is placed by a relay module composed of a lens (L6, $f = 300$ mm) and a mirror (M2) at its Fourier plane. The image relay ensures that both polarized components will experience the same amount of phase modulation. The common path length also ensures a superposition of both components on the camera without introducing a spatial shift. The total transmission of the SLM arrangement has been improved to $\sim 77\%$ compared to 41% in the previous work¹²². 23% of the system loss is mainly induced by double-reflection of the silver-coated knife-edge mirror and SLM, which can be further improved to 80% by simply replacing the silver-coated mirror with a dielectric coated mirror.

4.2.2 Minimizing Off-axis Aberration

To physically separate the second reflected light from the SLM with the first reflected one, off-centered light incident on the relay lens is intentionally introduced, which inevitably brings off-axis aberrations into the system. Compared to a well collimated laser beam, the intrinsic divergence of fluorescence light further aggravates the effect of off-axis aberrations. To characterize the divergence of the fluorescence light propagating in the detection path (Figure 33), a bright dye layer (Atto488) was imaged using a 491 nm laser with a peak emission at the

wavelength of 520 nm, which can be clearly visualized by eyes. To minimize the non-symmetric aberration induced by the off-center light, we first optimized the distance between two incident light onto the SLM by calculating the minimal distance from the knife-edge mirror to the SLM (h) without introducing light blocking,

$$h = D_{pupil} / \tan(\theta) \quad (14)$$

where D_{pupil} is the diameter of the pupil aperture at the conjugated BFP, θ is the angle between incident and reflected light on the surface of the SLM. Here $\theta = 10^\circ$. Meanwhile, 1-inch quarter-waveplate was placed close to the reflection mirror to avoid any beam blocking.

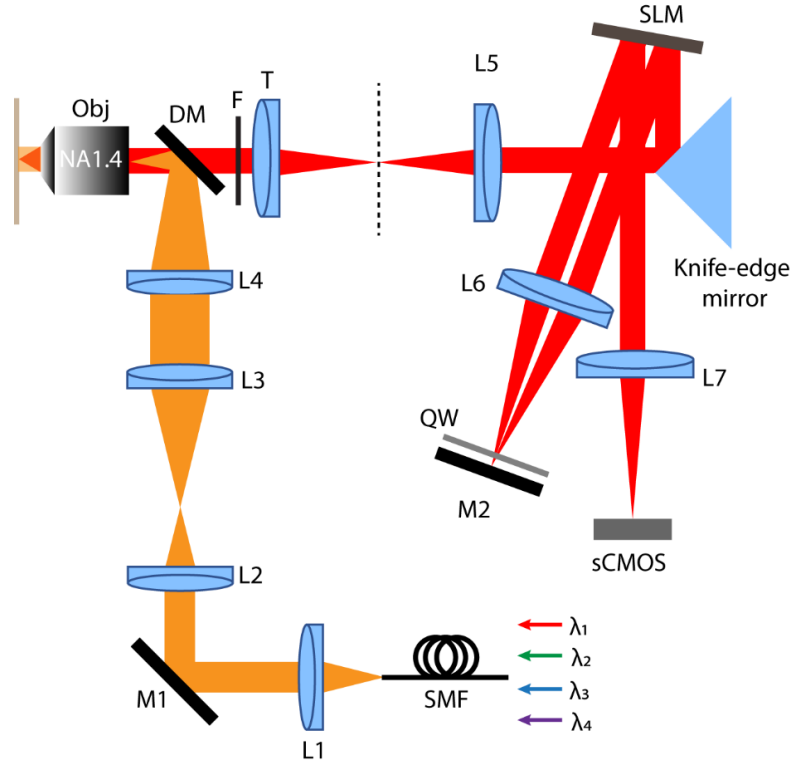


Figure 32 Microscope design with improved transmission efficiency. $\lambda_1 = 638$ nm, $\lambda_2 = 532$ nm, $\lambda_3 = 491$ nm, $\lambda_4 = 405$ nm; DM, dichroic mirrors; F, multiband emission filter; L1-7, lenses; T, tube lens; M1-2, mirrors; Obj, objective lens; QW, quarter waveplate; SLM, spatial light modulator; SMF, single mode fiber.

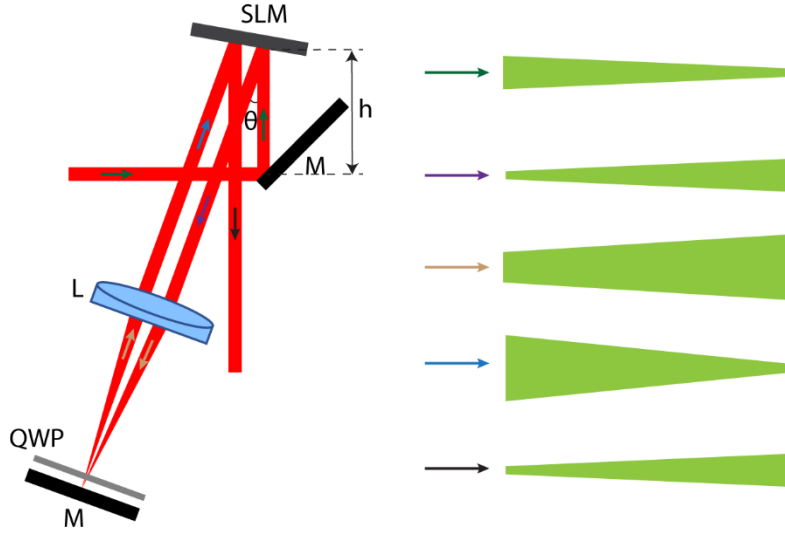


Figure 33 Characterization of fluorescence light divergence in the detection path. Different colors represent the sub-path in the detection. The divergence was characterized by imaging a bright dye layer (Atto488) on the coverslip. The dye was excited by 491 nm laser. h is the vertical distance from the edge of mirror to the SLM. θ is the angle of the incident and reflected light from the SLM.

Additional aberrations that cannot be removed by the careful alignment was characterized and compensated by implementing the corresponding phase function onto the SLM by searching through different combinations of first 12 Zernike polynomial terms. As a result, the main contribution of aberrations was observed as first-order astigmatism as a combination of vertical astigmatism ($\phi_{ast_0^\circ}$) and oblique astigmatism ($\phi_{ast_45^\circ}$):

$$\phi_{ast} = C_1 \phi_{ast_0^\circ} + C_2 \phi_{ast_45^\circ} \quad (15)$$

where C_1 (0.6) and C_2 (-0.5) are the weighting factors of two astigmatism terms. Figure 34 showed the focal response of WF at x - y and x - z planes without/with astigmatism correction. Compared to the non-symmetric PSF resulting from off-axis aberration, a diffraction-limited PSF was generated after the aberration correction. The residual aberrations can be detected and compensated by either

using a wavefront-sensor directly^{50,123} or using software-based phase retrieval algorithms, in which specific laser beams generated by certain phase patterns are used for sensing even small wavefront distortions, which could induce remarkable deformations from their desirable shapes. By finding the corresponding phase pattern that generates the distorted beam-shape, a compensated aberration pattern of the system can be implemented onto an adaptive optics, such as SLM or DM to compensate any phase distortion of the system.

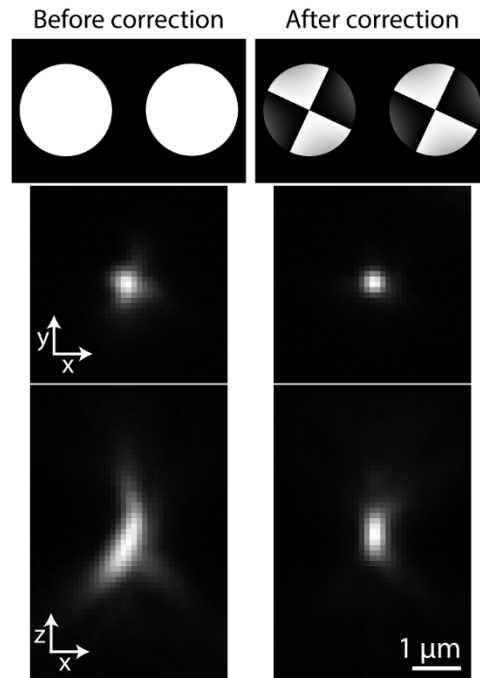


Figure 34 Focal responses of WF before and after off-axis aberration correction.

4.2.3 PSF Measurement

To measure the PSF of 2.5DM in the double-pass configuration, we imaged 200 nm fluorescent beads dispersed in 1× phosphate-buffered saline buffer (PBS, pH 7.4). Because the beads are smaller than the diffraction spot, it can serve as point emitters excited by the illumination

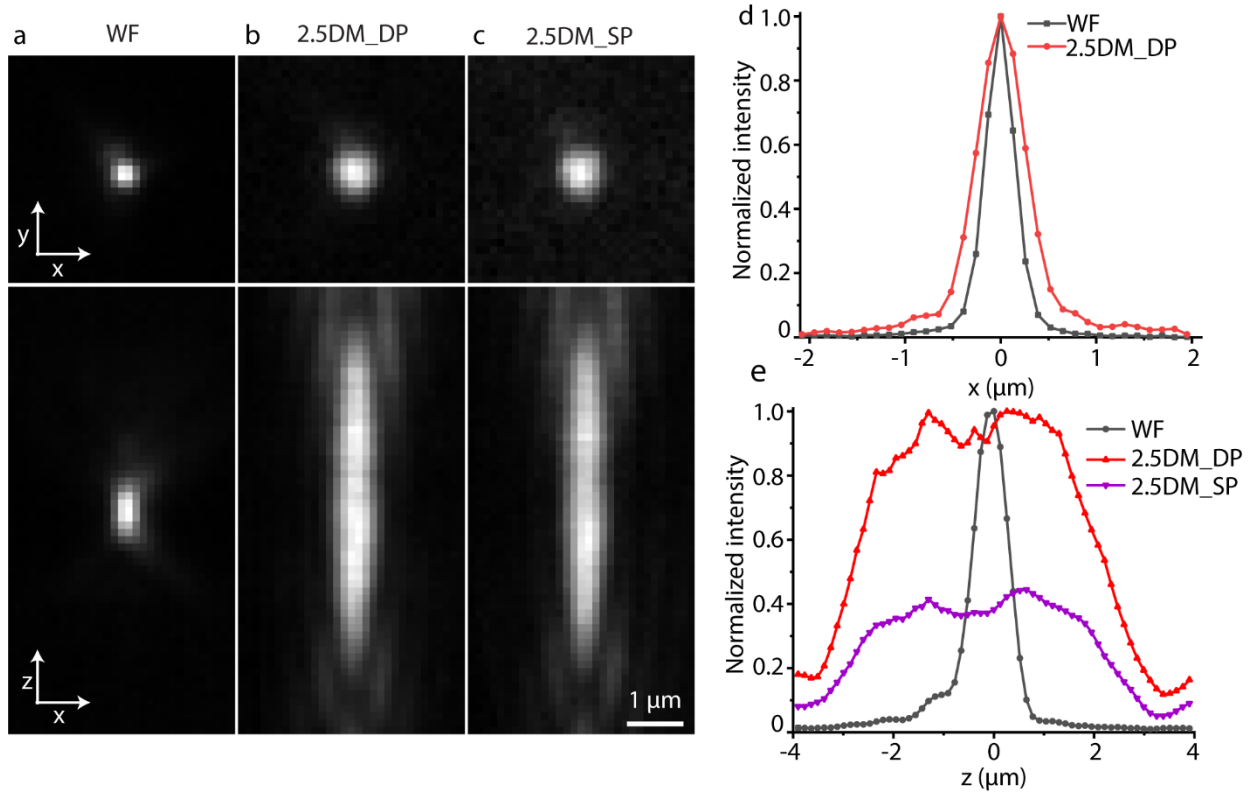


Figure 35 PSF measurements using 200-nm fluorescent beads. (a-c) Intensity distribution at x - y and x - z planes with WF (a), 2.5DM with double-pass (b) and single-pass (c) configurations. (d) Lateral intensity profiles of WF (black) and double-pass 2.5DM (red). (e) Axial intensity profiles of WF, 2.5DM with double-pass and single-pass (purple) configuration, where the axial intensity of 2.5DM with single-pass configuration was normalized with respect to the peak intensity value of 2.5DM with double-pass configuration.

light ($\lambda = 638 \text{ nm}$) and the emission light was then collected by an oil immersion objective lens ($\text{NA} = 1.4$). Compared to the PSF with a clear aperture referred as widefield (WF) (Figure 35a), a defocus-invariant PSF along the optical axis was demonstrated by our 2.5D system with double-pass configuration (Figure 35b). Similar PSF distribution has been observed by a single-passing 2.5D system (Figure 35c) where a linear polarizer was used to discard unmodulated emission light

by the SLM, which corresponds well with our previous result¹²². From the intensity profiles (Figure 35d and 35e), one can see that 2.5DM changes the FWHM of the PSF along the x -axis from 0.36 μm to 0.58 μm while the FWHM along the z -axis changes from 0.76 μm to 5.03 μm . Therefore, with 2.5D imaging system, an axial depth extension of 6.6-fold is achieved while the lateral width is broadened by only a factor of 1.6. More importantly, one can see that with the double-pass configuration, the peak intensity along the axial direction has been increased by 2.25-fold compared to the case with a single-pass configuration. A slightly higher than 2-fold improvement of the peak intensity by the double-pass configuration may attribute to the uneven power transmission of two orthogonal polarized components.

4.2.4 smFISH Imaging

In our previous work¹²², we have demonstrated the potential application of 2.5DM in RNA imaging. To further validate the capability of double-pass configuration in improving the total transmission efficiency, we performed smFISH imaging in U2OS cells on the target of *EEF2* with 32 FISH probes labeled with AF647. First, a 3D stack of smFISH images was obtained by WF over a 5 μm thickness at an exposure time of 340 ms per step (25 steps in total) and an excitation intensity of 100 W/cm² and a maximum intensity projection (MIP) of the 3D stack along the axial axis was performed to display the location of individual mRNAs within each cell (Figure 36a). Next, we recorded a single snapshot image by double-pass 2.5DM at the exposure time of 1 s and the same excitation intensity as WF (Figure 36b). We counted the copy number of mRNAs in the same cell under WF and 2.5DM based on a spot-finding algorithm¹⁴. As expected, the number of detected mRNAs by WF (589) and 2.5DM (574) showed a good agreement with each other. We

further analyzed well-isolated single molecule spots and plotted background-subtracted peak intensity in a histogram for three cases, i.e., WF, 2.5DM with double pass configuration, and 2.5DM with single-pass configuration (Figure 36c). As a result, 2.5DM with double-pass configuration showed a comparable mean value of the peak intensity with WF while the mean value of the peak intensity with single-pass 2.5DM was decreased by a factor of 1.97, indicating a significantly improved transmission efficiency via the double-pass arrangement.

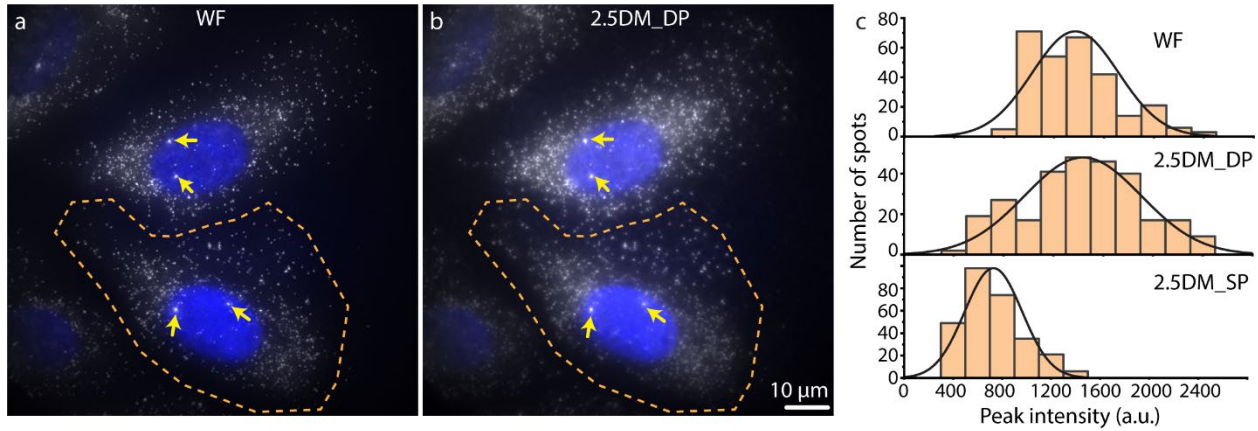


Figure 36 Single-molecule FISH images of *EEF2* on U2OS cells by double-pass 2.5DM. (a-b) Images obtained by MIP of a stack of images (25 steps in total) (a) and 2.5DM with double-pass configuration (b) for the 3D cell volume. Nuclei stained with DAPI are shown in blue. 32 FISH probes were labeled with AF647. Yellow arrows indicate the active transcription sites. The copy number of mRNAs in a single cell enclosed by a yellow polygon was counted in (a) and (b). Images were acquired under epi-illumination at an excitation intensity of 100 W/cm² with an exposure time of 340 ms/step (WF) and 1s (double-pass 2.5DM). (c) Peak intensity histograms of single-molecule spots by WF and 2.5DM with double-pass/single-pass configuration.

4.3 Depth Aberration Correction

The depth aberration can be theoretically estimated for a given imaging depth into the sample, which results from the path length difference induced by the refraction of light at an interface of two media (Figure 37b). when the light emitted from a point source at the focal plane of a lens through two different media ($n_1 > n_2$), the phase aberration introduced at the BFP of the lens can be expressed as

$$\phi_{BPF} = \frac{2\pi}{\lambda} d \left(n_2 \sqrt{1 - \left(\frac{NA\rho}{n_2} \right)^2} - n_1 \sqrt{1 - \left(\frac{NA\rho}{n_1} \right)^2} \right) \quad (16)$$

where d is the distance of the interface and the imaging depth, λ is the wavelength of the emission light, NA is the numerical aperture of the objective lens and ρ is the normalized radial coordinate at the pupil plane. From the aberration function, one can see that aberration induced by refractive index mismatch is a depth-dependent aberration which requires a simultaneous phase update when imaging a 3D volume of a thick sample.

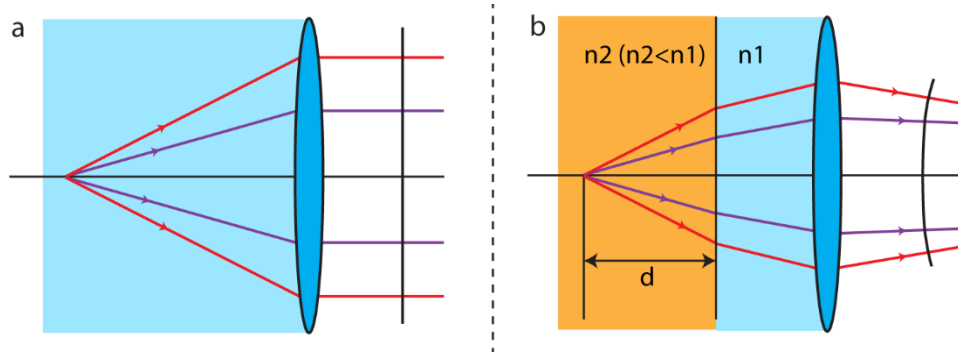


Figure 37 Ray trace of a point source through a lens in a uniform medium (a) and in two media (b) with different refractive index ($n_2 < n_1$). d represents the distance from the point source to the interface of two media. The wavefront at BFP of the lens is displayed as the vertical line (plane wave) in (a) and the curved line (distorted wavefront) in (b).

4.3.1 Characterization of Depth Aberration by Simulation

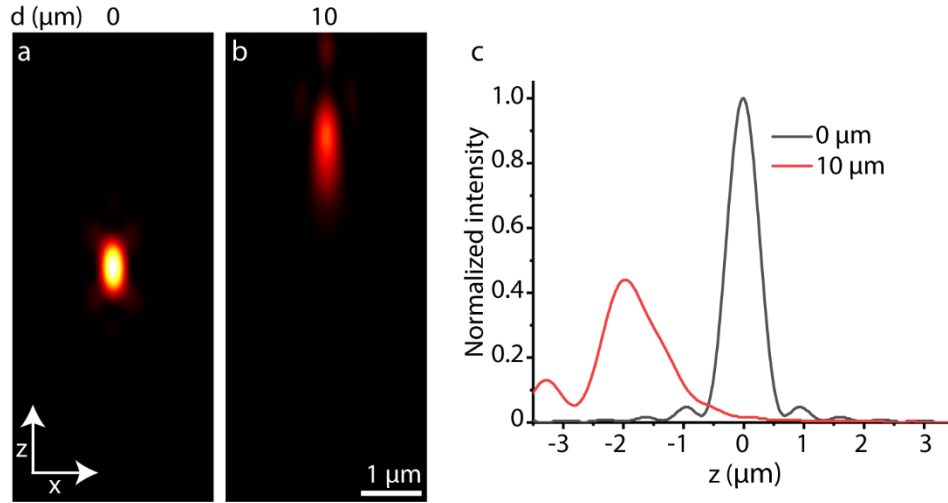


Figure 38 Simulation of focal responses by WF with depth aberration induced. (a-b) Intensity distributions of PSFs at the x - z plane at the imaging depth of 0 μm (a) and 10 μm (b) above the coverslip. Both intensity values are normalized with respect to the peak intensity at the depth of 0 μm . (c) Intensity profiles along the axial direction for the corresponding cases. The wavelength (λ) used in the simulation is 670 nm and the refractive index n_1 is 1.518 and n_2 is 1.33.

We simulated the effect of the depth aberration in PSF distortion by WF and 2.5DM in a high NA imaging system ($\text{NA} = 1.4$). The wavelength used in the simulation is 670 nm which is close to the emission maximum of a common red-emitting fluorophore AF647. In the WF case, compared to the PSF at the coverslip (Figure 38a), the resulting PSF at the imaging depth of 10 μm (Figure 38b) showed a strong spherical aberration and the peak intensity decreased by a factor of 2.27 than that at the coverslip (Figure 38c). one may also note that the position of the focal spot at the depth of 10 μm showed a nearly 2 μm shift compared to the spot right at the coverslip. Therefore, depth aberration induced by the index mismatch not only degrades the signal intensity and spatial resolution, but also introduces a depth-dependent defocusing, which could increase the

imaging volume required to cover the entire specimen. In 2.5DM, we simulated the focal response at imaging depth of 10 μm (Figure 39a) and 20 μm (Figure 39b). The uniformity of intensity distribution along the axial direction breaks and the PSFs exhibit a strong intensity variation as the imaging depth moves deeper into the sample (Figure 39d). However, with implementing the phase function represented in Equation (17), the distorted PSFs (Figure 39a and 39b) are readily to be recovered back to a moderately uniform intensity distribution over a specific depth (5.5 μm) as shown in Figure 39d.

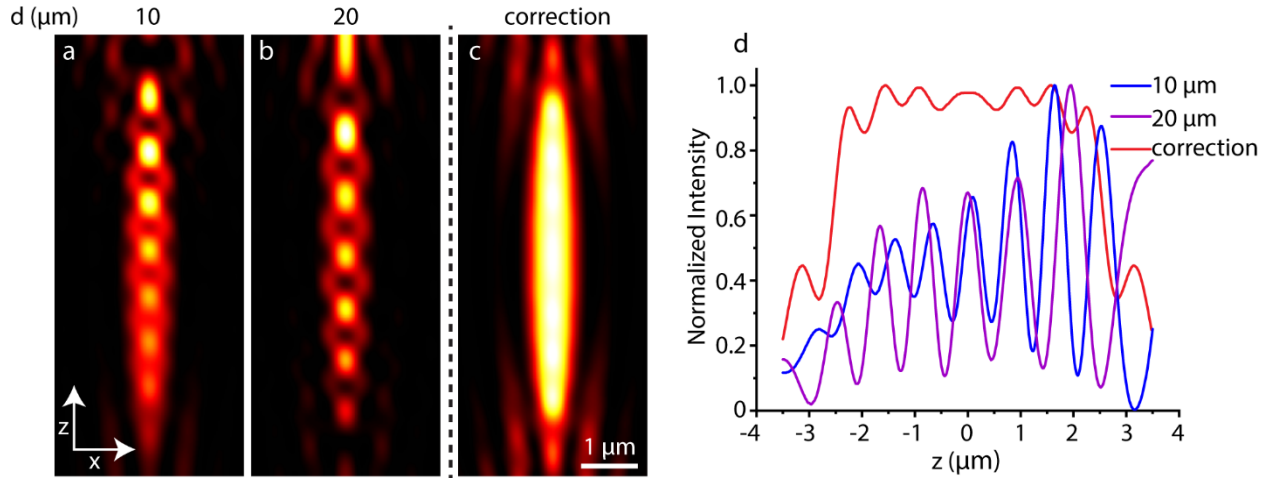


Figure 39 Simulation of focal responses by 2.5D phase with depth aberration induced. (a-c) Intensity distributions of PSFs at the x - z plane at the imaging depth of 10 μm (a), 20 μm (b) above the coverslip and after correcting for the corresponding depth aberration (c). (d) Intensity profile along the axial direction for the corresponding cases.

4.3.2 Characterization of Depth Aberration by Experiments

To experimentally study the effect of deep aberration in imaging thick samples, such as tissues, we first measured the focal response of fluorescence beads in a gel solution (refractive

index of 1.33) at the depth of 10 μm above the coverslip by WF. As a result, the measured PSF before correcting for the corresponding depth aberration (Figure 40a) exhibited strong distortion, which is similar to the effect of spherical aberration. After compensating the corresponding depth aberration, the focal response showed a more tightly focal spot. From the intensity profiles (Figure 40b, 40c), one can clearly see that with the depth aberration correction the FWHM of the PSF along the axial direction was significantly reduced from 1.32 μm to 0.88 μm while the lateral FWHM changed from 0.44 μm to 0.38 μm . The peak intensity of the corrected PSF was increased by a factor of 1.78 than that of the uncorrected PSF. We recorded a 3D stack of bead images around the depth of 10 μm above the surface and resliced it at the x - z plane as shown in Figure 40d and 40e. One can immediately see that before the depth aberration, the location of each focal spot was shifted by a certain distance along the z -axis ($\sim 2.34 \mu\text{m}$) compared to the position in the corrected image, indicating a good agreement with the simulation (Figure 38). As expected, the peak intensity of the corrected image (Figure 40e) showed a remarkable increase with much tightly focal spots compared to the uncorrected image (Figure 40d).

In 2.5DM, the defocus-invariant PSF at the coverslip exhibited a high uniformity over a specific depth as described in the simulation of Chapter 2, which is very crucial for quantitative single-molecule imaging. To elucidate the effect of the depth aberration in the extended PSF, we measured the PSFs of the 2.5D imaging system at the imaging depth of 20 μm above the coverslip without (Figure 41a) and with (Figure 41b) correcting for the depth aberration. As one can see from the plot of the intensity profiles along the axial direction (Figure 41c), without the aberration correction the intensity showed a strong variation while it exhibited high uniformity over the

designed DOF after correcting for the depth correction, which corresponded well with the simulation (Figure 39c).

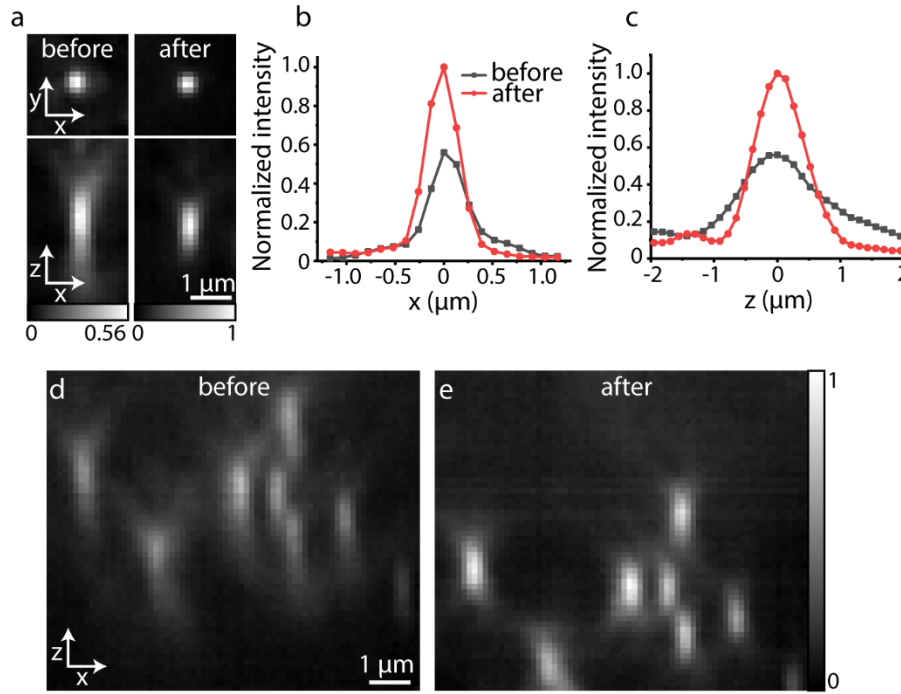


Figure 40 Measurement of depth aberrations by WF using 3D fluorescent beads. (a) Intensity distributions of PSFs at the imaging depth of 10 μm above the coverslip before/after the depth aberration compensation. (b-c) Lateral (b) and axial (c) intensity profiles before (black) and after (red) correcting for the depth aberration. Both intensity profiles are normalized with respect to the peak intensity value after the aberration correction. (d-e) Images of hydrogel beads at the x-z plane around the image depth of 10 μm before (d) and after (e) the depth aberration compensation.

A PSF displaying poor uniformity may cause information loss when projecting the volumetric image onto a 2D plane, especially, when imaging a thick biological sample, such as tissues. To elucidate this issue, we imaged a 3D bead sample in a gel solution within 20 μm thickness. Given the FWHM ($\sim 5 \mu\text{m}$) of 2.5D PSF measured along the axial axis, we first obtained

a 3D stack of images with 4 μm per step without adding any aberration compensation. Then the depth aberration term corresponding to the z-position at 2, 6, 10, 14, 18 μm , was superposed with the 2.5D phase to correct the aberration at the middle of each step. 2D projected images by maximum intensity projection showed that several spots displayed on the corrected image (Figure

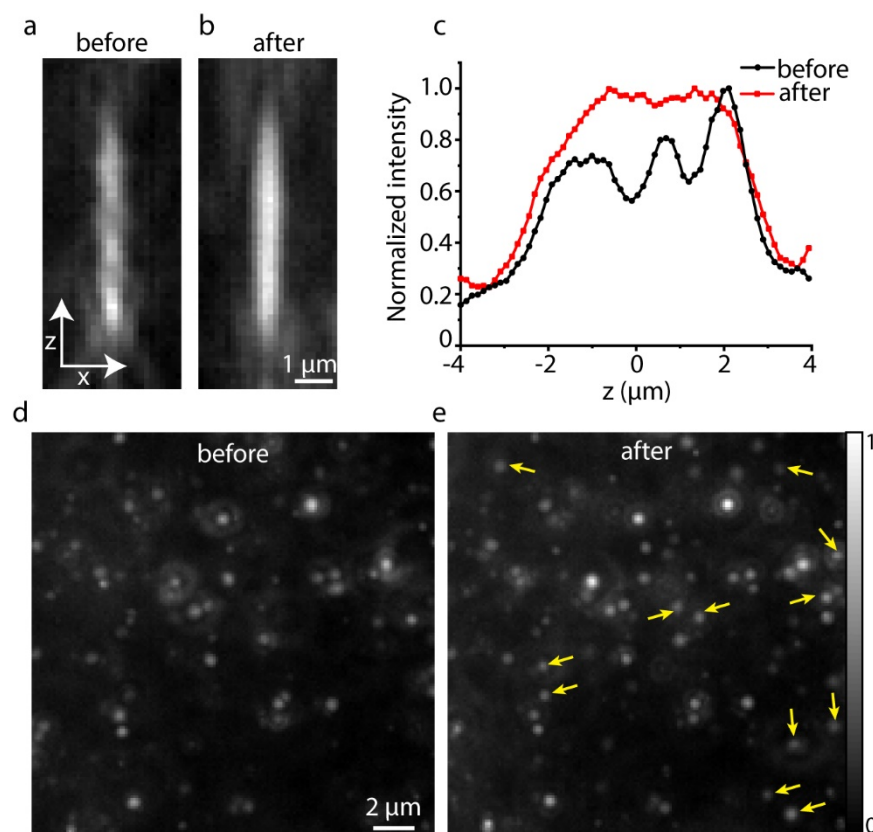


Figure 41 Measurement of depth aberrations by 2.5DM using 3D fluorescent beads. (a-b) Intensity distributions at the x-y and x-z planes before (a) and after (b) the depth aberration correction. (c) Axial intensity profiles before (black) and after (red) correcting for the depth aberration. Intensity profiles before/after the aberration correction are normalized with respect to the peak intensity values of themselves. (d-e) Images of hydrogel beads obtained by MIP of a stack of images (5 steps in total) within a thickness of 20 μm before (d) and after (e) correcting for the corresponding depth aberration at 2, 6, 10, 14, 18 μm , respectively.

41e) were missing in the uncorrected image (Figure 41d). The axial information loss can be explained by two problems existing in the distorted PSF: poor uniformity of the axial intensity and shift of the centered position of the extended focal spot as the image moves deeper into the sample. Combined with the depth aberration correction, 2.5DM could be used for imaging thick samples with significantly increasing the acquisition rate.

4.3.3 Fluorescent Labeled Collagen Imaging

As we have demonstrated the effect of depth aberration in distorting the PSF with 2.5DM, including the degradation of intensity uniformity within the designed DOF and the focal shift compare to the PSF at the coverslip, an effective aberration correction for different imaging depth through a thicker sample should greatly improve the fidelity of volumetric imaging with substantially reducing the image acquisition rate, in which the PSF of 2.5DM throughout the sample maintains its uniformity over the extended axial depth and relocate the focal plane as the same as that at the coverslip. This is demonstrated in Figure 42 by imaging rat tail collagen labeled with Atto647N. We polymerized the collagen gel at temperature of 4 °C and imaged 8 z-positions within a thickness of 32 μm , and then projected onto a 2D image by MIP using an exposure time of 100 ms per frame under epi-illumination (3 W/cm²) without the correction for depth aberration (Figure 42a and 42c) and with the correction (Figure 42b and 42d) sequentially at the depth of 2, 6, 10, 14, 18, 22, 26, 30 μm , respectively. As expected, the projected image after the aberration correction showed more fibred features which were lost in the uncorrected image. The result well corresponded with 3D beads image (Figure 41d and 41e). The aberration-corrected image (Figure 42d) also demonstrates better intensity uniformity of spatial structures than the uncorrected image

because the axial intensity of the PSF without aberration correction exhibited a significant fluctuation, which would only enhance the contrast for structures located in specific depths.

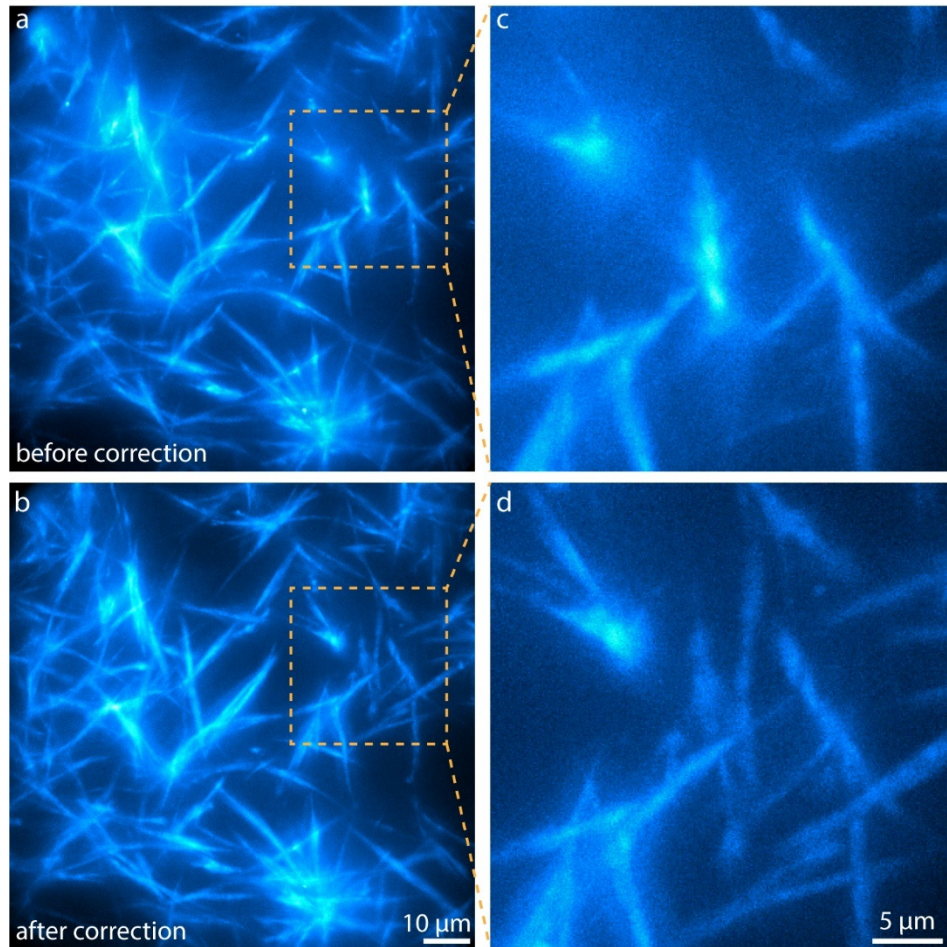


Figure 42 Fluorescent-labeled collagen images by 2.5DM with depth aberration correction. (a-b) Images obtained by MIP of 8 z-positions within a thickness of 32 μm before (a) and after (b) sequentially correcting the depth aberration at z- position of 2, 6, 10, 14, 18, 22, 26, 30 μm , respectively. (c-d) Corresponding zoom-in regions in (a) and (b) enclosed by a dash square. Rat tail collagen labelled with Atto-647N was polymerized at 4 $^{\circ}\text{C}$. All images were taken under epi-illumination at an excitation intensity of 3 W/cm^2 .

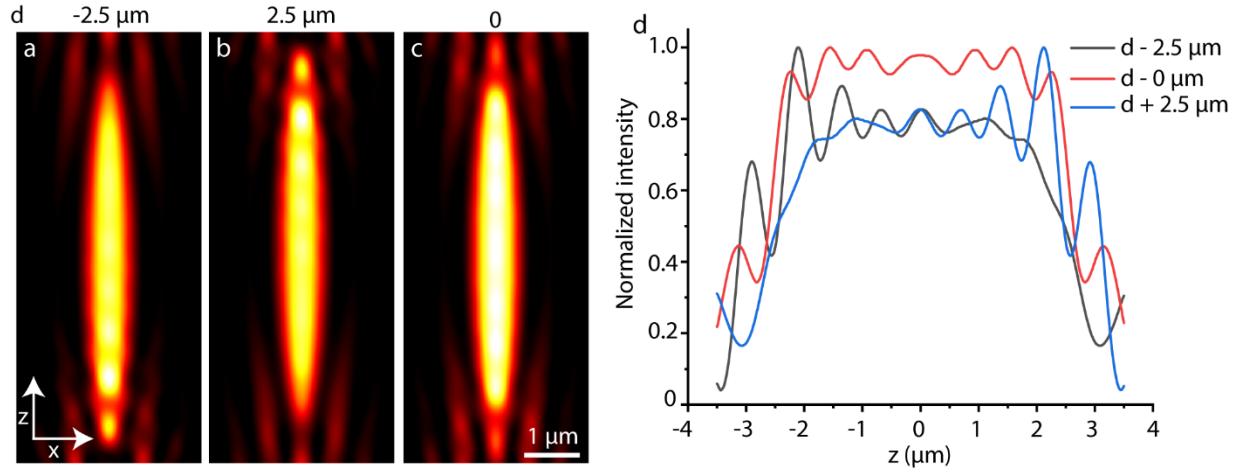


Figure 43 Focal responses of 2.5DM with depth aberration correction at the middle z -position. (a-c) Intensity distributions of PSFs located at $2.5 \mu\text{m}$ below (a) and above (b) the middle z -position (c). (d) Intensity profiles along the z -axis for the corresponding cases.

In both wide-field microscopy and 2.5DM, the depth-induced aberration not only degrades the image quality in terms of SNR/SBR, but also significantly shift the focus as the image plane moves deeper. To obtain an aberration-free 3D image, depth-related aberrations must be simultaneously corrected at each axial position, which could be achieved by combining an adaptive element with a wavefront sensor in a closed loop system. However, a closed loop wide-field microscopy would significantly increase the image acquisition time, in particular, imaging a thick sample. 2.5DM with moderated depth aberration correction at the middle position of each extended DOF could substantially speed up the image acquisition by less serial z -scanning while maintaining the high uniformity of the axial profile as shown in the simulation (Figure 43), where within an image thickness of $5 \mu\text{m}$, the depth aberration was only compensated at the middle z -position (Figure 43c) of the entire thickness, the focal responses of the point sources located at 2.5

μm below (Figure 43a) and above (Figure 43b) the middle position showed moderately uniform intensity distribution, confirming a high fidelity of reserving volumetric information by 2.5DM.

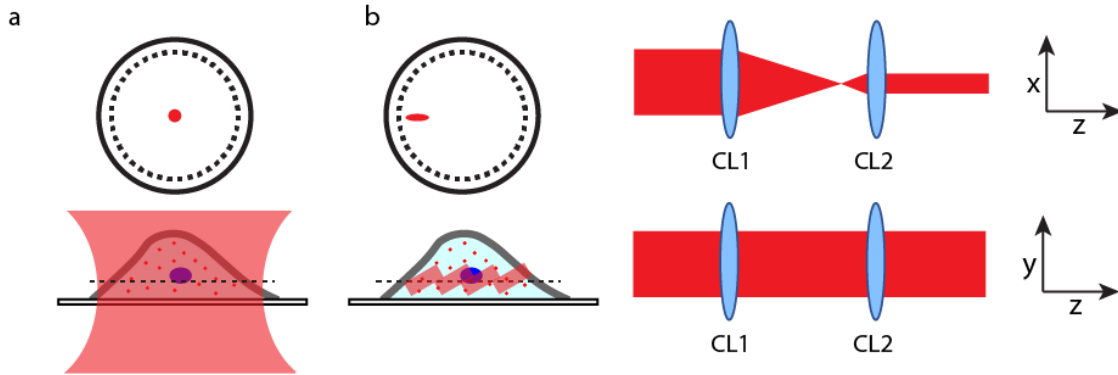


Figure 44 Schematic of Epi- and highly inclined swept tile illumination. (a) Epi-illumination wide-field microscopy. (b) HIST microscopy, where inclined tile beam ensures a thinner illumination. A pair of cylindrical lenses can be used to generate one dimensional elongated beam at the focal plane.

When imaging a thick biological sample under a wide-field epi-illumination, one may have to deal with a strong autofluorescence background, which can significantly reduce the SBR. In a worse situation, this autofluorescence could overwhelm the detected signal, leading to unfaithful interpretation of biological phenomena. To overcome this issue, many techniques have been reported by either improving the optical sectioning capability of the excitation beam, such as using light-sheet microscopy¹²⁴⁻¹²⁸ or using a highly inclined swept tile microscopy proposed recently⁶³, or by enhancing the fluorescence signal using hybridization chain reaction techniques¹²⁹. Compared to light-sheet microscopy, where two-objective arrangement makes it difficult to perfectly align the system and it also requires a specific design for mounting the sample, HIST microscopy needs only single objective with high compatibility with conventional microscopes. In HIST microscopy (Figure 44), an elongated beam generated by a pair of cylindrical lenses is

first focused on the BFP of the objective. Then a virtual light sheet is generated by laterally sweeping the tile beam with a confocal slit detection to remove out-of-focus fluorescence. In combination of two approaches, the autofluorescence background can be expected to be substantially suppressed with improved SBR.

CHAPTER 5 3D SUPER-RESOLUTION IMAGING BY SINGLE-MOLECULE LOCALIZATION

5.1 Overview

Limited by the wave nature of the light, the smallest distinguishable distance between two objects by conventional fluorescence microscopy is approximately about 200-300 nm along the lateral direction and 500-700 nm along the axial direction¹³⁰. Any subcellular structures smaller than 200 nm cannot be resolved due to the diffraction limitation. To visualize the molecules/proteins at the tens of nm level, Electron microscope (EM) can be used attributed to the much smaller wavelength of an electron than the visible light¹³¹. However, one main issue for EM stems from the sample preparation. An EM sample requires dehydration and thin sectioning which may introduce inappropriate interpretation for the images due to the variation of the structure¹³². The fixation and low pressure required by EM samples also makes it difficult for live-cell imaging. Unlike fluorescence microscopy, EM is difficult to identify specific molecules via the labeling of target proteins. Therefore, super-resolution fluorescence microscopy with nanometer resolution is highly desirable for biological studies.

In recent years, a variety of super-resolution techniques have been developed to break the diffraction limitation of fluorescence microscopy, mainly categorized by three different mechanisms. First, methods based on the nonlinear saturation effect which spatially suppresses the emission of a point source at the periphery to narrow the effective PSF of the imaging system, such as stimulated emission depletion (STED) microscopy^{133,134}. In this method, a tightly focused excitation beam would generate a diffraction-limited focal spot and the fluorescence in the peripheral region of the focal spot is depleted by an overlaid STED beam featuring a zero intensity

at the center of the beam through stimulated emission (Figure 45a). By scanning two overlaid beams over the sample, an image with much higher resolution (tens of nm) than the diffraction-limit could be generated. To improve the spatial resolution for wide-field microscopy, structured illumination microscopy (SIM)¹³⁵ has been developed by generating a series of excitation patterns, such as sinusoidal grids with a corresponding phase shift for each different pattern orientation (Figure 45b). In this approach, higher spatial frequency information beyond the cut-off frequency of a conventional microscope is encoded into the observed images and reconstructed in post image processing. A maximal two-fold enhancement of the spatial resolution can be achieved in a linear-SIM wide-field microscopy, limited by the inherent diffraction limitation of standing-wave patterns. Like STED microscopy, the spatial resolution can be further improved using non-linear or saturated SIM (SSIM)¹³⁶.

Instead of tailoring the excitation beam, another category of super-resolution techniques distinguishes molecules within the diffraction-limited volume by stochastically activating a sparse set of individual fluorophores far apart than the diffraction limitation at different time points and precisely localizing the position of each fluorophore by PSF fitting (Figure 45c), named as single-molecule localization microscopy (SMLM). These techniques include photoactivated localization microscopy (PALM)¹³⁷, fluorescence photoactivation localization microscopy (FPALM)¹³⁸, stochastic optical reconstruction microscopy (STORM)¹³⁹, and direct STORM (*d*STORM)¹⁴⁰. Although PALM/FPALM or STORM/*d*STORM uses different fluorophores, such as photoactivatable fluorescent proteins (PA-FPs) used in PALM/FPALM, pair of organic dyes used in STORM or standard organic fluorophores used in *d*STORM, the common mechanism behind these approaches is to reversibly control the transition of a fluorophore between the fluorescent

ON-state and nonfluorescent OFF-state in order to separate individual molecules that are densely labeled with fluorescent probes. In SMLM, the samples are typically illuminated by wide-field epi (3D imaging) or TIRF illumination (2D imaging). The uncertainty of single-molecule localization is inversely proportional to the square root of the number of detected photons¹⁴¹.

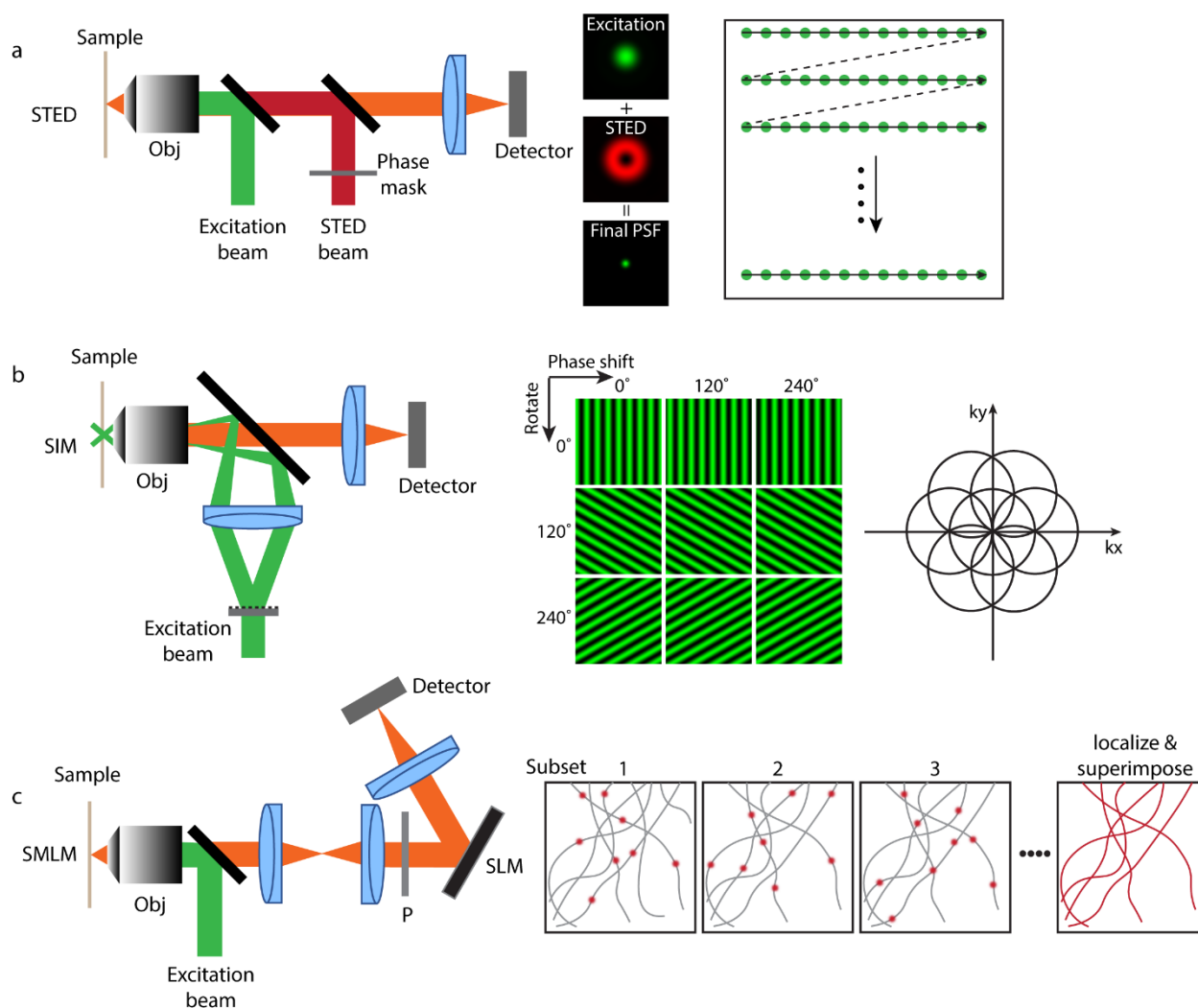


Figure 45 Super-resolution microscopies categorized in three mechanisms. (a-c) Principles of stimulated emission depletion⁸⁹ microscopy (a), structured-illumination microscopy (SIM) (b), and single-molecule localization microscopy (SMLM) (c). STED microscopy is a confocal-based technique, required point by point scanning. SIM and SMLM are generally conducted under wide-field epi illumination.

Whereas in PALM it is moderately easy to ensure only a sparse set of fluorophores residing in the ON-state at each time point by using FA-FPs, which are simply non-fluorescent before illuminating the sample with a light pulse at the wavelength of 405 nm used for activating the fluorophores, PA-FPs exhibit a lower photostability and brightness (typically a few hundred photons) than the standard organic fluorophores (several thousand photons) used in STORM/dSTORM¹⁴². Consequently, lower emitting photons directly results in a lower localization accuracy in PALM than that in STORM/dSTORM. Moreover, in PALM, before starting a next cycle, a sub-set of fluorophores residing in ON-state need to be photobleached after the signal readout. Typical frame rates (10-25 Hz)^{143,144} using PA-FPs are much lower than that (10-1,000 Hz)¹⁴⁵ using standard organic dyes in dSTORM. On the contrary, dSTORM shows its advantages in higher photostability, higher number of emitting photons and flexible controlment of frame rates by external conditions. More importantly, a variety of commercially available fluorophores over the entire visible spectra can be used in dSTORM in aqueous solvents and the photoswitching rates can be easily controlled by the concentration of thiol added into the imaging buffer, the pH of the solvent and the excitation intensity¹⁴⁶.

5.2 Methods for 3D Localization via PSF Engineering

Given that a 2D SMLM measurement might lose some critical information in different depths, in recent years, numerous studies have been performed in achieving 3D super-resolution imaging by PSF engineering. In these approaches, the precision of the axial localization is improved by encoding the depth information of fluorescent emitters into the variation of the PSF shapes controlled by specific designed phase patterns^{47,56,68-70} implemented onto an adaptive optics,

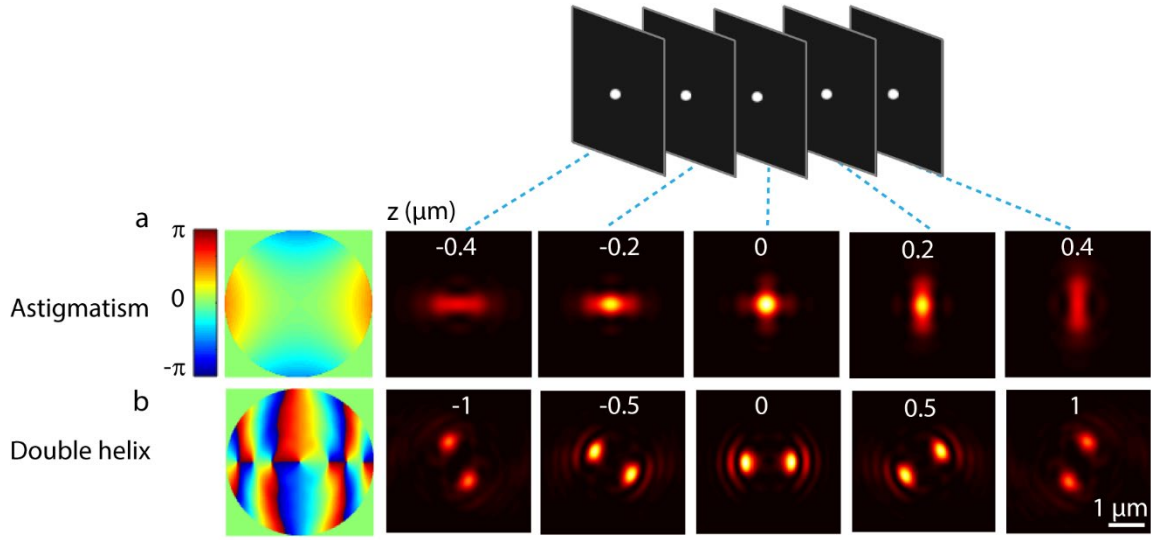


Figure 46 3D SMLM by PSF engineering. (a) Astigmatic phase mask on the back focal plane (left) and focal responses (right) at the different imaging depths, where the PSF widths along x and y axes vary as a function of defocusing depth. (b) Double-helix phase mask (left) and focal responses (right) at the x - y plane, where the angle of two main PSF lobes is characterized as a depth-encoded parameter.

including astigmatic PSF⁶⁸, rotating double-helix PSF (DH-PSF)⁴⁷, self-bending PSF⁶⁹, and Tetrapod PSF⁵⁶, to name a few. Although these engineered PSFs exhibit different shapes, the essential feature for all varies distinctly as a function of defocusing depth¹⁴⁷. To precisely localize the positions of molecules laterally and axially, such distinguishable parameters are first extracted and characterized based on the specific shape of PSFs, for example, the variation of PSF widths along x and y axes for the astigmatic PSF (Figure 46a), or the angle of two main PSF lobes for the case of DH-PSF (Figure 46b). Axial position of an emitter is then determined by a calibration curve associated with these parameters and the lateral position is calculated in a manner as other localization methods, i.e. by fitting the image data into an ideal PSF generated by simulation.

For more complicated-shaped PSFs such as Tetrapod, it becomes almost impossible to extract a simple parameter representing the depth position. In this case, to translate the fine feature of 3D PSF and improve the precision of the localization process, one should directly fit the cross-section profile in each depth to a 3D PSF model. According to the wide-ranging performance of these engineered PSFs in terms of size and axial range, one should cautiously choose the PSF that suits the specific application. For instance, the astigmatic PSF has much smaller axial range than that of the DH-PSF ($\sim 2\text{-}3\ \mu\text{m}$) and the Tetrapod PSF has even larger range up to $\sim 6\ \mu\text{m}$ at the expense of the larger footprint¹⁴⁷. Taken the simplicity of image-reconstruction and the range of the encoded depth into consideration, we demonstrated a 3D SMLM using DH-PSF in the next section.

5.3 dSTORM Imaging using DH-PSF

5.3.1 Calibration of Imaging System by DH-PSF

To generate a DH-PSF in which the depth information of each molecule is encoded in two rotated lobes around the optical axis, the same imaging system as 2.5DM was used where instead of loading a 2.5D phase pattern, a phase mask (Figure 47a) composed of multiple spiral phase functions, was implemented onto the SLM. Compared to the phase pattern optimized from superimposed Gaussian-Laguerre (GL) modes¹⁴⁸, multi-spiral-based approach^{149,150} shows more flexibility in extending the depth of the PSF by simply adjusting the number of spiral zones of the phase pattern as shown in the simulation under a high NA imaging system (Figure 48). The remarkable feature of this approach could benefit 3D-SMLM that requires to image biological structures with different thickness.

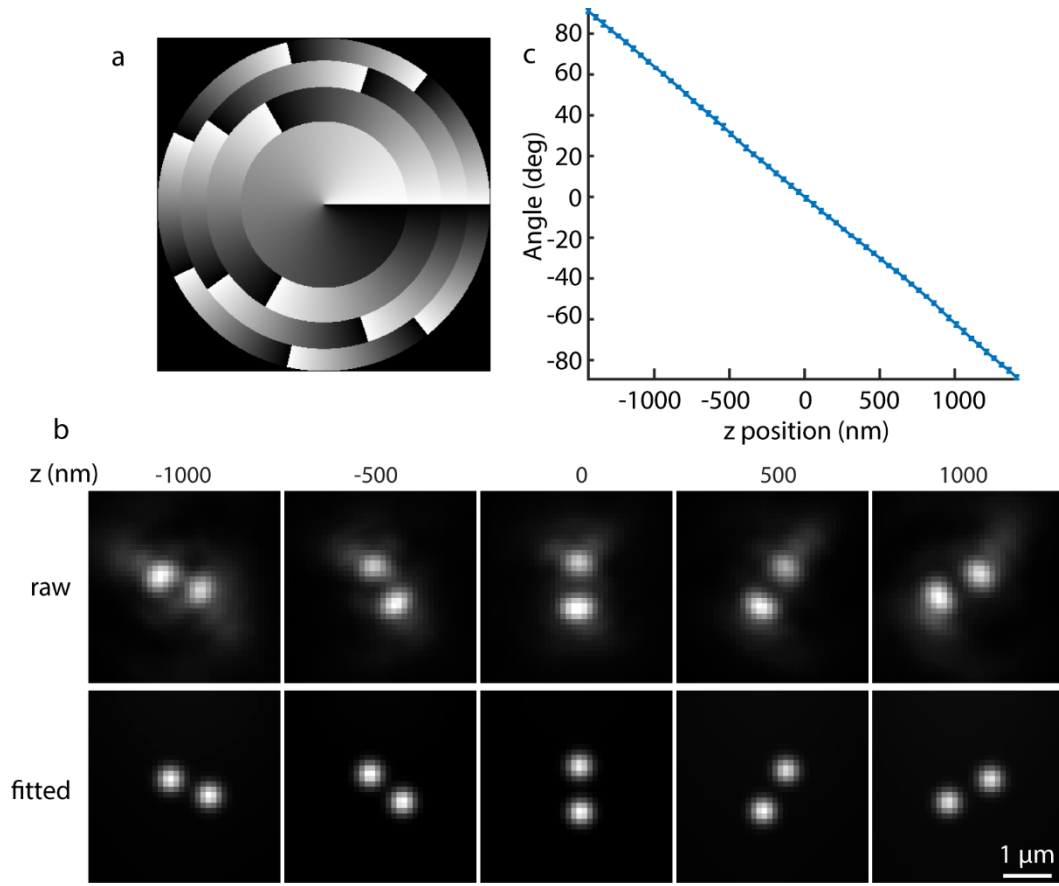


Figure 47 Calibration of DH-PSF imaging system. (a) Phase pattern used to generate DH-PSF. (b) Images of a fluorescent bead (200 nm) at different axial positions with raw images (upper) and fitted images (lower). (c) Plot of the rotating angle of two lobes with respect to the vertical direction as a function of z-position controlled by a piezo-stage. Fluorescent beads were excited by a laser at $\lambda = 638$ nm.

We calibrated the relation of z-position vs the rotated angle of DH-PSFs by imaging 200-nm fluorescent beads immobilized onto the coverslip. Fluorescent beads, served as point emitters, were excited by epi-illumination at the wavelength of 638 nm. Each emitter showed two double-helix lobes, which were vertical when the object was in-focus. As the object was moved towards or away from the objective lens, the two lobes were rotated in a counterclockwise or clockwise direction accordingly as shown in Figure 47b. To determine the 3D position of each emitter, raw

DH-PSFs were first fitted into two gaussian-distributed spots (Figure 47b) using an open-source software (easy-DHPSF)¹⁵¹. The lateral position (x & y) was then calculated from the midpoint coordinates of the line terminated by the central positions of two lobes. A stack of DHPSF images were recorded via a serial z-scanning with a step size of 50 nm and the corresponding angle of two lobes with respect to the vertical direction was extracted and plotted as a function of z-positions as shown in Figure 47c, indicating a nearly linear relation between the angle and the axial position.

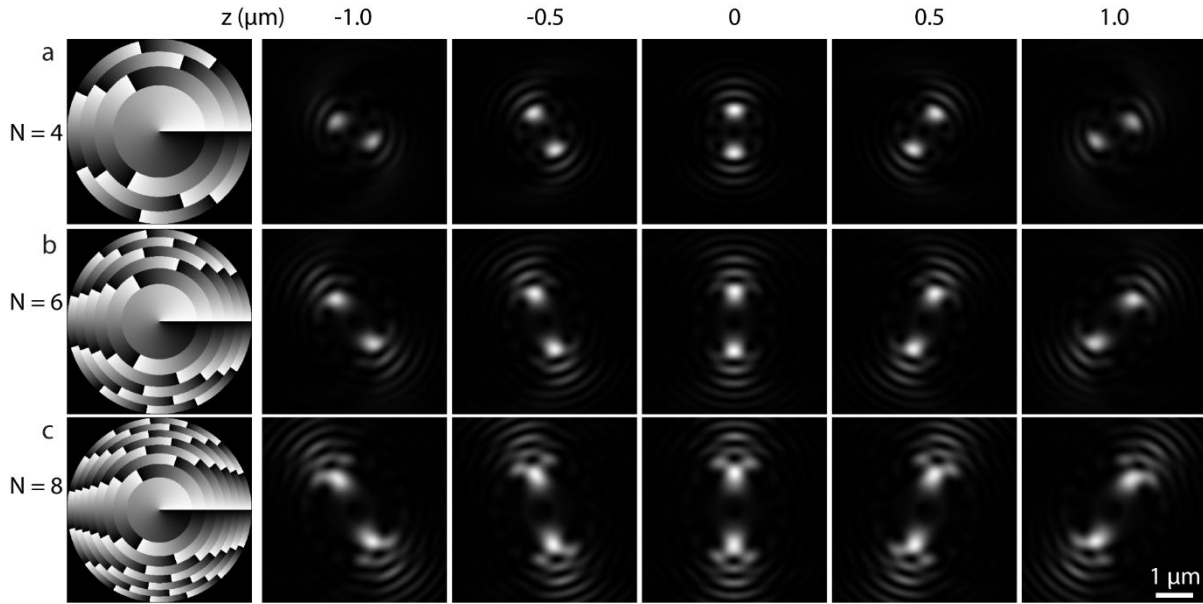


Figure 48 Focal responses of DH-PSFs at different axial positions with varying spiral zones. N represents the number of spiral zones with $N = 4$ (a), $N = 6$ (b) and $N = 8$ (c). Intensity distributions in each case are normalized to the peak intensity when the emitter is in focus.

5.3.2 Localization Precision of Single Molecules

Many biological structures are fluorescence-labeled using antibodies conjugated with organic dyes in order to visualize their fine details. It's critical to demonstrate the localization precision of single molecules which in general show low single to noise ratio due to the limited

number of emitting photons (up to few thousands). The precision of estimating a fluorophore is highly dependent on the number of photons (N) emitted from the fluorophore and the size of PSF (σ_{PSF}) in an approximated relation of σ_{PSF}/\sqrt{N} .¹⁴¹ In other words, more emitting photons from the fluorophore would lead to more accurate localization, which is not limited by the wave nature of the light. The photo-switching mechanism of many commercially available dyes has been thoroughly studied¹⁴⁶. The first category of fluorophores used in *d*STORM are carbocyanine fluorophores, such as Cy5¹²⁶, Alexa Fluor 568¹⁵² and Alexa Fluor 647¹⁵³, which have shown remarkable photo-stability and brightness with minimal photobleaching.

We characterized the localization precision of a typical dye used in *d*STORM, AF647, by imaging single molecule DNAs labeled with AF647 immobilized on the coverslip. Before imaging, the sample was embedded in aqueous buffer under specific blinking conditions¹⁵⁴ i.e. a low concentration of Trolox in phosphate-buffered saline (PBS, pH 7.4). By illuminating the sample with a 638-nm laser at the intensity of 2.4 kW/cm² and exposure time of 50 ms, a sparse set of fluorophores were observed with switched on and off for multiple cycles. Each well-isolated blinking molecule generated a cluster of 3D localizations based on the calibrated curve from DH-PSFs. By collecting each cluster and translating them into a common origin (Figure 49a), more than 2,000 localization events were analyzed, resulting in standard deviations of localizations as 13.1 nm along x-axis, 13.8 nm along y-axis and 21.5 nm along z-axis as shown in the histograms (Figure 49b, 49c and 49d). An average of 2700 photons were produced by each fluorophore during each image acquisition cycle (50 ms). This result showed a similar localization accuracy as obtained in previous studies^{68,151}. As one can see that the localization precision in the z-direction

was lower than that measured in x and y directions attributed to the decreased SNR of the emitter as it moved away from the focal plane.

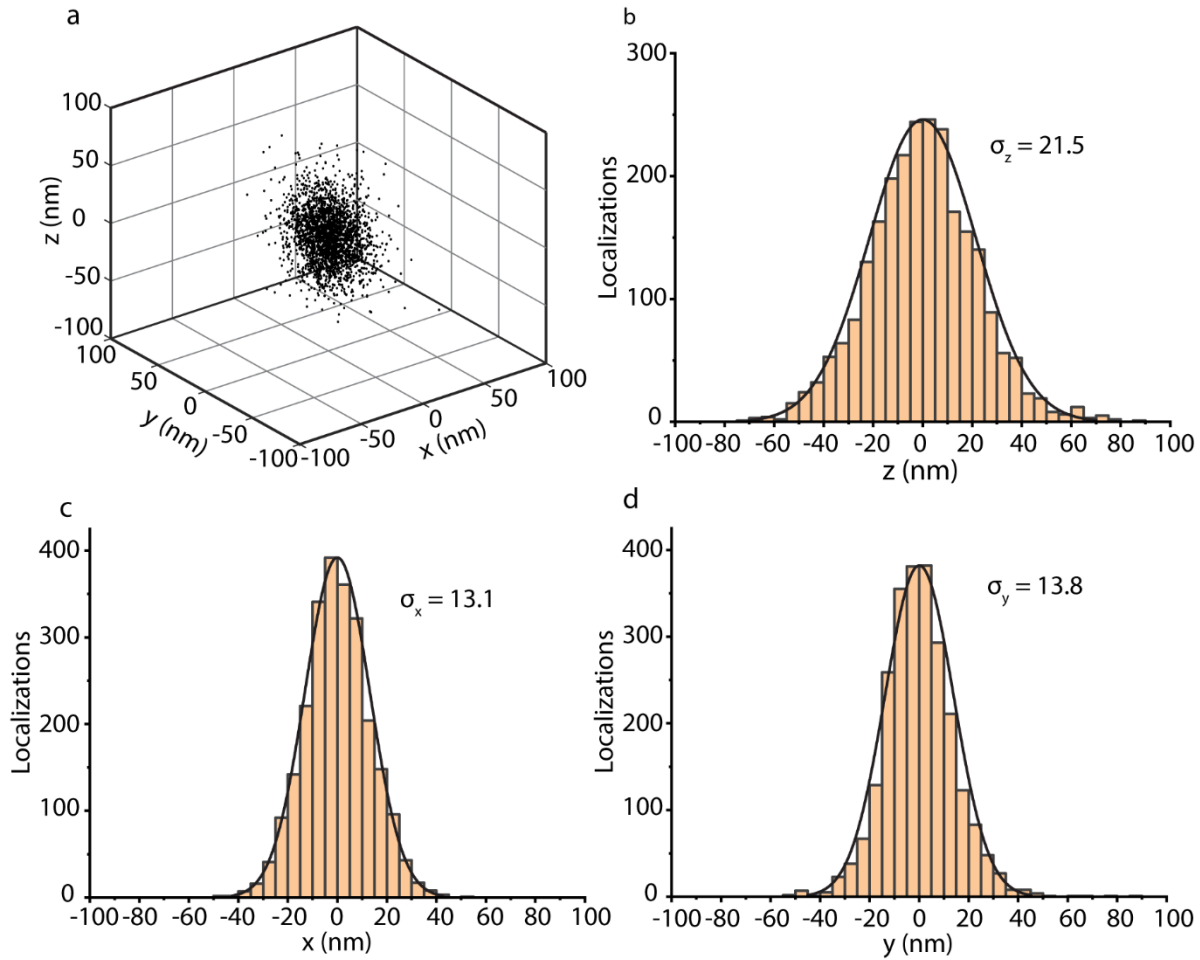


Figure 49 Experimental characterization of 3D localization precision for single fluorophore. (a) Localizations from subsets of clusters of repeated blinking molecules, where each cluster of localizations were translated to a common origin by center of mass and the total number of localizations analyzed was 2,000. (b-d) Histograms of localizations along the z -direction (b), x -direction (c) and y -direction (d) with standard deviations by Gaussian fitting: 13.1 nm in x and 13.8 nm in y and 21.5 nm in z .

5.3.3 3D Super-resolution Imaging in Mammalian Cells

To validate the 3D *d*STORM for cell imaging, we further performed immunofluorescence imaging of microtubules labeled with AF647 in U2OS cells. A switching buffer, containing oxygen scavenger (0.5 mg/mL glucose oxidase, 40 mg/mL catalase, 10% w/v glucose) and 50 mM β -mercaptoethylamine (MEA) in $1\times$ PBS buffer (pH 7.4), was added into the chamber before imaging. For cyanine fluorophores, the photo-switching can be significantly improved by applying an oxygen scavenging system. The sample was first illuminated under a low intensity (< 0.1 kW/cm²) to find the targeting structures with minimal photobleaching. Then the excitation intensity was increased to 10 kW/cm² in few seconds in order to switch the majority of fluorophores to fluorescent off-state. During the repeated on and off cycles, sparse sets of fluorescent molecules were observed in each frame at an exposure time of 20 ms (Figure 50a). 20,000 frames of images were recorded within 6.6 min and each well-isolated molecule was fitted by the calibrated DH-PSF to determine the 3D localizations. Correction for the stage drift, along *x*-, *y*- or *z*-direction was not necessitated within this amount of image acquisition time. Compared to a snap-shot image by the wide-field microscope (Figure 50b), after reconstruction, 187,390 localizations were calculated over a FOV of $16 \times 16 \mu\text{m}^2$, resulting in a substantial improvement in spatial resolution with color-coded *z* information over an imaging depth of $\sim 1 \mu\text{m}$ (Figure 50c). Overlapped microtubule filaments located in different depths can be clearly visualized in the reconstructed image, which were not distinguishable in the WF image (Figure 50f). To quantitatively measure the resolution of the DH image, a histogram of localizations around a microtubule filament was plotted, showing a full width of 48 nm of the filament (figure 50g).

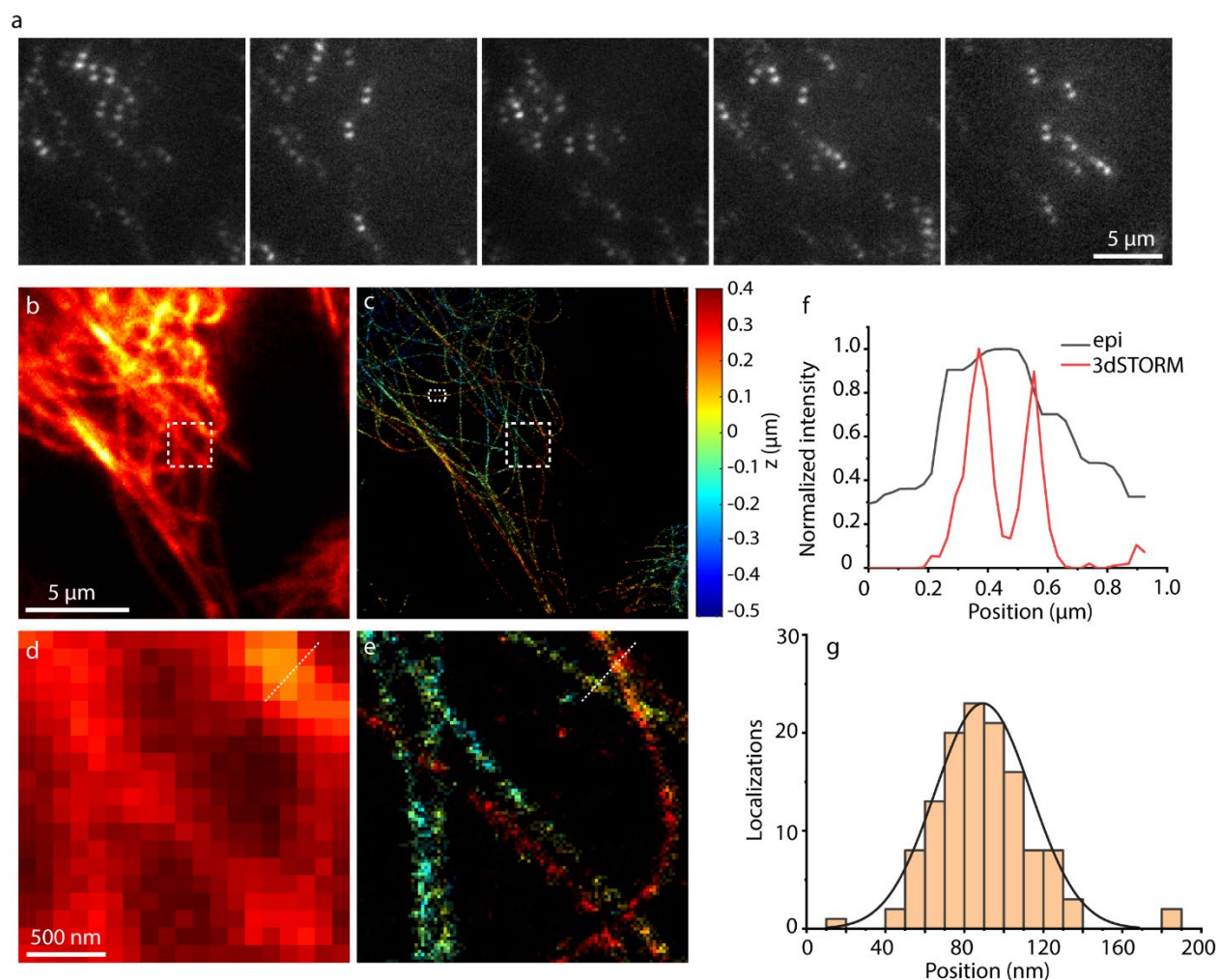


Figure 50 3D *d*STORM imaging of microtubules in U2OS cells. (a) Representative DH-images at different frames (20 ms per frame), indicating sparse sets of double helices encoding the 3D localization information of each molecule above the background noise. (b) epi-illumination image taken by a snapshot. (c) Reconstructed image in 3D over a FOV of $\sim 16 \times 16 \mu\text{m}^2$. The depth information was color-coded over an axial range of $\sim 1 \mu\text{m}$. (d-e) Zoomed images of subregions surrounded by dash squares in (b-c). (f) Line profiles of dash lines with epi-image (d) and *d*STORM (e). (g) Histogram of localizations of a straight microtubule segment (dash rectangular in (c)), yielding a lateral resolution of $\sim 48 \text{ nm}$.

CHAPTER 6 CONCLUSION

First, we presented a 2.5D imaging platform for fast and high-throughput subcellular imaging, that could substantially improve the image acquisition rate while maintaining high-resolution and single-molecule sensitivity. Compared to conventional methods via serial z-scanning to obtain volumetric information for 3D cell imaging, 2.5DM could project axial information onto a 2D image plane in a single camera exposure by generating a defocus-invariant PSF over a specific depth using a binary phase pattern implemented onto the SLM at the conjugated BFP of an objective lens. In contrast to other PSF engineering approaches for EDOF imaging, the obtained PSF using 2.5D phase function exhibits high-uniformity of the axial intensity and negligible lateral side-lobes. Moreover, 2.5DM shows the tunability of adjusting the imaging depth by simply controlling the strength of the aberration terms and a negligible degradation in focal responses for broadband emission, confirming its versatility to fluorescence microscopy.

Second, we employed 2.5DM in performing quantitative mRNA FISH imaging in mammalian cells. The copy number of mRNAs founded by 2.5DM in individual cells well corresponded with the number counted by conventional approaches (WF) while 2.5DM increased the imaging speed by an order of magnitude. Additionally, 2.5D approach showed superior SBR to the average intensity projection of the 3D stack images, mimicking a fast-volumetric imaging method by rapidly moving the focal planes. Whereas it compromised the SBR by 1.7 compared to the maximum intensity projection of the 3D stack images, the higher throughput efficiency (~10-fold) and less photodamage than WF could greatly compensate the reduction of the image quality. In particular, by using multiple singly labeled probes, signal from each emitter could be well

presented above the noise background, maintaining high-fidelity in quantitative single-molecule measurements. We also performed high-throughput smFISH imaging over a $2 \times 2 \text{ mm}^2$ region in mammalian cells with less than 10 min and immunofluorescence imaging at a volumetric imaging rate of $>30 \text{ Hz}$ with significantly reduced light dose exposed onto the specimens.

Then, we demonstrated a polarization-insensitive SLM-based 2.5DM which significantly improved fluorescence detection efficiency via a double-pass configuration. Furthermore, SLM, served as an adaptive element, provides a flexibility in compensating aberrations induced by the specimen, such as from the refractive index mismatch between the sample and immersion media (referred as to depth aberration), and aberrations induced by optical components as well. With the depth aberration correction, the axial intensity of the PSF by 2.5DM maintains high uniformity at different image depth as that at the coverslip. We employed the improved 2.5DM in quantitative mRNA FISH imaging in mammalian cells. The copy number of mRNAs counted in individual cells showed a good agreement with the counted number by WF. Moreover, under the same illumination intensity, it showed superior SNR to single-pass 2.5DM, indicating its great improvement in transmission efficiency, facilitating its versatility to photon-limited applications and showing its potential capability of further improving the throughput by decreasing the exposure time. We also showed that our 2.5DM could be used for imaging thick biological specimens with high fidelity of preserving volumetric information with substantially reduced z-scanning depths.

Finally, we demonstrated a 3D single-molecule localization imaging platform via encoding the depth information into the shape of the PSF using double-helix phase pattern. In this approach, the axial depth of the PSF can be flexibly adjusted by controlling the number of spiral zones in the

phase pattern. We validated the 3D SMLM by imaging immunostaining microtubules in mammalian cells with a measured resolution of ~ 48 nm using *d*STORM techniques. With 2.5DM and SMLM integrated in the same imaging system, our multi-functional microscope allows both fast and high-throughput volumetric imaging and super-resolution imaging by simply switching the specific phase patterns without any add-on module which might induce misalignment of the system and lead to improper interpretation of biological phenomena, especially for multi-color imaging. By combining our multi-functional microscope with other techniques, such as light-sheet microscopy and/or MERFISH, the throughput efficiency of measuring different RNA species simultaneously in individual cells could be remarkably increased, making image-based single-cell transcriptomics more comparable to commonly used high-throughput techniques, such as qPCR and RNA-seq. Moreover, our imaging system showed the potential advantages of low light dose and single-shot 3D images, which makes it possible to capture fast dynamics of cellular features in a large cell population, opening a potential pathway for advancing imaging-based assays in biological applications.

APPENDIX A: METHODS

PSF measurement

3D PSF of our 2.5D imaging system was measured using 80 nm gold nanoparticles (EM.GC80, BBI Solutions) or 200 nm fluorescent beads (F8806, ThermoFisher) immobilized on a poly-L-lysine (P8920, Sigma-Aldrich) coated flow chamber. For the gold nanoparticles, immersion oil (IMMOIL-F30CC, Olympus) was added to the flow chamber to match refractive index while the fluorescent beads were immersed in 1× phosphate-buffered saline buffer (PBS, pH 7.4). After recording a series of z-scanning images of beads or gold nanoparticles, the lateral and axial intensity profiles of the PSF around the centroid of the focal spot were measured.

Fluorescence intensity measurement of immobilized single molecules

Biotin labeled bovine serum albumin (BSA, A8549, Sigma-Aldrich) was coated on a flow chamber as described previously¹⁵⁵. After washing with PBS, 50 µg/mL neutravidin (31000, ThermoFisher) was added into the chamber and incubated for 2 minutes before washing out with PBS. ~100 pM of biotinylated DNA (18 nt; IDT) labeled with Atto647N (ThermoFisher) was incubated in the flow chamber for 5 minutes. Before imaging, an imaging buffer composed of 20 mM Tris (pH 8), 50 mM NaCl, an enzymatic oxygen scavenger system (0.8% (w/v) dextrose, 1 mg/mL glucose oxidase, 0.04 mg/mL catalase) and 2 mM Trolox was added into the chamber. Well-isolated single-molecule spots were selected using a custom-made MATLAB script¹⁵⁵. The peak intensity of each detected spot was calculated in a 7×7 -pixel array around the centroid of the spot after background subtraction.

Single-molecule RNA FISH on cultured mammalian cells

FISH probes (20 nt, 5'-amine) for *EEF2* and *TOP2A* designed by Stellaris Probe Designer were purchased from IDT. 10 µL of 1 mM FISH probes dissolved in Milli-Q water was mixed

with 10 μ L of 20 mM AF647-NHS ester (A20006, ThermoFisher) or Cy3B-NHS ester (PA63101, Cytiva), dissolved in DMSO and 55 μ L of 0.1 M sodium borate buffer (pH 8.5). The reaction vial was then incubated at room temperature overnight. The labeled DNAs were purified by ethanol precipitation and subsequently resuspended with a T50 buffer (10 mM Tris, 50 mM NaCl, pH 8). U2OS cells (human bone osteosarcoma, ATCC) were cultured with McCoy's 5A medium (30-2007, ATCC) mixed with 10% fetal bovine serum (F2442, Sigma) and 1% penicillin-streptomycin (15140122, ThermoFisher), and plated on an 8-well Lab-Tek chamber, then incubated for 48-72 hours at 37°C with 5% CO₂. Similar to our previous study⁶³, cells were first fixed with 4% (v/v) paraformaldehyde (PFA, 15710, Electron Microscopy Sciences) at room temperature for 10 min. After washing 3 times with PBS, cells were permeabilized with 0.5% (v/v) Triton X-100 in PBS for 15 min. After another washing step, they were incubated in wash buffer (Deionized formamide 10%, 20 \times saline-sodium citrate buffer (SSC) 10%, RNase-free water 80%) at room temperature for 5 min. Cells were incubated at 37°C overnight with FISH probes (5 nM for each probe) in hybridization buffer (100 mg/ml dextran sulfate, 1 mg/ml *E.coli* tRNA, 2 mM Vanadyl ribonucleoside complex, 0.2 mg/ml RNase free BSA, 2 \times SSC and 10% deionized formamide dissolved in RNase-free water). After adding wash buffer and incubating at 37°C for 30 minutes (repeat 3 times), the nuclei were stained with DAPI for 10 min at 37°C. Before imaging, imaging buffer was added into each chamber to reduce photobleaching. For two-color smFISH, *EEF2* and *TOP2A* labeled with Cy3B and AF647, respectively, were used while for one-color smFISH, they were labeled with AF647. 32 and 48 FISH probes were used for detecting *EEF2* and *TOP2A*.

Immunofluorescence imaging

After the confluency of U2OS cells grown on a coverslip was more than 70%, the culture medium was removed from the chamber and the cells were rinsed with PBS once. For immunostaining vimentin, the cells were fixed and permeabilized by incubating the coverslip in ice-cold methanol (-20°C) for 5 min. For immunostaining microtubules, the cells were first fixed with 3% Paraformaldehyde (PFA) and 0.1% glutaraldehyde in PBS for 10 min at room temperature. After washing cells with PBS for three times, the cells were incubated in 0.1% sodium borohydride dissolved in PBS immediately for 7 min to reduce unreacted aldehydes. Then the cells were washed for three times with PBS and permeabilized with 0.5% Triton X-100 in PBS for 15 min. After the fixation and permeabilization, the cells were washed for three times with PBS and then incubated in a blocking solution of 3% BSA (37525, ThermoFisher) for 1 hour to reduce non-specific binding. Then, the cells were first incubated with primary antibodies diluted in the blocking solution: monoclonal mouse anti-vimentin (V6389, Sigma-Aldrich) or monoclonal mouse α -tubulin (ab7291, Abcam) at a concentration of 3 μ g/ml overnight at 4°C refrigerator. Before adding secondary antibodies, the cells were washed twice with PBS for 5 min each. The cells were then incubated with secondary antibodies diluted in the blocking solution: goat anti-mouse F(ab')₂ fragment antibody (115-006-146, Jackson ImmunoResearch) labeled with AF647 at a concentration of 3 μ g/ml for 2-3 hours at room temperature. Then the sample was washed twice with PBS for 5 min each. For immunofluorescent imaging, the sample was mounted with Mowiol and sealed with epoxy and stored at -20 °C refrigerator for later use. For *d*STORM imaging, a switching buffer containing oxygen scavenger (0.5 mg/mL glucose oxidase, 40 mg/mL catalase, 10% w/v glucose) and 50 mM β -mercaptoethylamine (MEA) in 1 \times PBS buffer (pH 7.4) was added into the chamber before imaging.

Fluorescent beads imaging on 3D hydrogel

A hydrogel solution was prepared using 7.5% acrylamide and bisacrylamide (1610140, 1610142, Bio-Rad) (29:1), 0.2% tetramethylethylenediamine (TEMED, T7024, Sigma), 0.1% ammonium persulfate (A3678, Sigma) in 0.5× TAE buffer (Tris-acetate-EDTA). 200 nm fluorescent beads (F8806, ThermoFisher) were added to the hydrogel solution at a final concentration of 2% (v/v). 50 µL of the mixture was quickly injected into a flow chamber and incubated at room temperature for 5-10 min. The left solution can be used to check if the gel is formed.

Polymerization of rat tail collagen

The collagen (A1048301, ThermoFisher) labeled with Atto647N (5.5 mg/ml) and unlabeled collagen (3 mg/ml) were mixed and diluted by 1×PBS (pH 7.4) at 4°C to achieve a final concentration of 2 mg/ml collagen solution, containing 2% labeled and 98% unlabeled collagen. A small amount of NaOH could be used to adjust the final pH of the mixed solution to ~7-7.4. The solution was injected into a prechilled flow chamber and incubated at 4°C overnight to gradually polymerize the collagen gel.

APPENDIX B: MATLAB SCRIPT

```

%% script for simulating the focal response at the x-z plane of 2.5D imaging
system
%% system parameters:
NA = 1.4; % numerical aperture of objective lens
n = 1.518; % refractive index of immerision medium
lamda = 670e-9; % wavelength of the emission light
k = 2*pi*n/lamda; % wavenumber
alpha = asin(NA/n); % maximum open angle of objective lens

%% image plane in cartesian coordinates
Lx = 1.5e-6; % observation window along x-axis, unit: um
Lz = 4.0*1e-6; % observation window along z-axis, unit: um
Nx = 151; % discretization of image plane
Nz = 401; % discretization of image plane
x2 = linspace(-Lx,Lx,Nx);
z2 = linspace(-Lz,Lz,Nz);
[X2,Z2] = meshgrid(x2,z2);
Y2 = 0;

%% coordinates in the back focal plane (pupil plane)
N_theta = 400;
N_phi = 100;
delta_theta = alpha/(N_theta-1); % discretization of theta
delta_phi = 2*pi/(N_phi-1); % discretization of phi
theta0 = eps:delta_theta:alpha;
phi0 = eps:delta_phi:2*pi;

% transform to polar coordinate
rho = sin(theta0)./sin(alpha);
[Rho,Phi] = meshgrid(rho,phi0);

%% 2.5D phase pattern
gamma0 = 8; % control the strength of the spherical
aberration
psi0 = -1.525; % control the defocusing term for
optimizing the axial uniformity
P_df = exp(-1i*2*pi*psi0*Rho.^2); % phase term representing defocusing
P_sa = exp(-1i*2*pi*gamma0*Rho.^4); % phase term representing spherical
aberration

% combine spherical aberration and defocusing
P_comb = P_df.*P_sa;
P_bin = zeros(size(P_comb));
P_bin(real(P_comb)>=0) = 1;
P_bin(real(P_comb)<0) = -1;
Pupil = P_bin; % phase function at the back focal plane

%% electrical field at the image plane
Ex2 = 0; % Ex component in focal
Ey2 = 0; % Ey component in focal
Ez2 = 0; % Ez component in focal

```

```

%% integral of vectorial diffraction
for theta = eps:delta_theta:alpha
    for phi = eps:delta_phi:2*pi

        % add the effect of the polarization at the focal plane
        a = 1+(cos(theta)-1).*(cos(phi)).^2;
        b = (cos(theta)-1).*cos(phi).*sin(phi);
        c = -sin(theta).*cos(phi);
        d = 1+(cos(theta)-1).*(sin(phi)).^2;
        e = -sin(theta).*sin(phi);
        ff = cos(theta);
        V = [a b c;b d e;-c -e ff];
        px = [1,0,1/sqrt(2),1i/sqrt(2),2/sqrt(5),cos(phi),-sin(phi)];
        py = [0,1,1i/sqrt(2),1/sqrt(2),1i/sqrt(5),sin(phi),cos(phi)];
        pz = 0;
        P = [px(1,3);py(1,3);pz];

        % polarization in focal region
        PP = V*P;

        % complex amplitude at the back focal plane (pupil plane)
        A = Pupil(ceil(phi/delta_phi),ceil(theta/delta_theta));

        % numerical calculation of field distribution in focal region
        Ex2 =
        Ex2+A*sin(theta)*sqrt(cos(theta)).*PP(1,1).*exp(1i*k*(Z2*cos(theta)+sin(theta)
        ).*(X2*cos(phi)+Y2*sin(phi))))*delta_theta*delta_phi;
        Ey2 =
        Ey2+A*sin(theta)*sqrt(cos(theta)).*PP(2,1).*exp(1i*k*(Z2*cos(theta)+sin(theta)
        ).*(X2*cos(phi)+Y2*sin(phi))))*delta_theta*delta_phi;
        Ez2 =
        Ez2+A*sin(theta)*sqrt(cos(theta)).*PP(3,1).*exp(1i*k*(Z2*cos(theta)+sin(theta)
        ).*(X2*cos(phi)+Y2*sin(phi))))*delta_theta*delta_phi;

    end
end

%% incoherently superpose intensity of different components
Ix2 = conj(Ex2).*Ex2;
Iy2 = conj(Ey2).*Ey2;
Iz2 = conj(Ez2).*Ez2;
I1_xz = Ix2+Iy2+Iz2;

% normalize
MM1 = max(I1_xz(:));
I1_xz = I1_xz/MM1;

%% plot the intensity distribution at x-z plane and intensity profile along
z-axis, and x-axis
figure
surf(X2*1e6,Z2*1e6,I1_xz);
shading interp

```

```

axis image
view(2)
colormap(hot)
caxis([0 1])
xlabel('x');
ylabel('z');
title('Intensity distribution at x-z plane')

% intensity profile along z-axis
figure
plot(Z2(:, (Nx+1)/2)*1e6, I1_xz(:, (Nx+1)/2));
xlabel(['z ', '\mu m']);
ylabel('Normalized intensity');

% intensity profile along x-axis
figure
plot(X2((Nz+1)/2, :)*1e6, I1_xz((Nz+1)/2, :));
xlabel(['x ', '\mu m']);
ylabel('Normalized intensity');

```

LIST OF REFERENCES

- 1 Neumann, B. *et al.* Phenotypic profiling of the human genome by time-lapse microscopy reveals cell division genes. *Nature* **464**, 721-727 (2010).
- 2 Eulalio, A. *et al.* Functional screening identifies miRNAs inducing cardiac regeneration. *Nature* **492**, 376-381 (2012).
- 3 Almaça, J. *et al.* High-content siRNA screen reveals global ENaC regulators and potential cystic fibrosis therapy targets. *Cell* **154**, 1390-1400 (2013).
- 4 Chong, Y. T. *et al.* Yeast proteome dynamics from single cell imaging and automated analysis. *Cell* **161**, 1413-1424 (2015).
- 5 Mahecic, D., Testa, I., Griffié, J. & Manley, S. Strategies for increasing the throughput of super-resolution microscopies. *Curr. Opin. Chem. Biol.* **51**, 84-91, (2019).
- 6 Kim, J., Venkata, N. C., Hernandez Gonzalez, G. A., Khanna, N. & Belmont, A. S. Gene expression amplification by nuclear speckle association. *J. Cell Biol.* **219**, e201904046 (2019).
- 7 Buxbaum, A. R., Haimovich, G. & Singer, R. H. In the right place at the right time: visualizing and understanding mRNA localization. *Nature reviews Molecular cell biology* **16**, 95-109 (2015).
- 8 Battich, N., Stoeger, T. & Pelkmans, L. Image-based transcriptomics in thousands of single human cells at single-molecule resolution. *Nature methods* **10**, 1127 (2013).
- 9 Moffitt, J. R. *et al.* Molecular, spatial, and functional single-cell profiling of the hypothalamic preoptic region. *Science* **362**, eaau5324 (2018).
- 10 Eng, C.-H. L. *et al.* Transcriptome-scale super-resolved imaging in tissues by RNA seqFISH+. *Nature* **568**, 235-239 (2019).

- 11 Kanter, I. & Kalisky, T. Single cell transcriptomics: methods and applications. *Frontiers in oncology* **5**, 53 (2015).
- 12 Morin, R. D. *et al.* Profiling the HeLa S3 transcriptome using randomly primed cDNA and massively parallel short-read sequencing. *Biotechniques* **45**, 81-94 (2008).
- 13 Sultan, M. *et al.* A global view of gene activity and alternative splicing by deep sequencing of the human transcriptome. *Science* **321**, 956-960 (2008).
- 14 Raj, A., van den Bogaard, P., Rifkin, S. A., van Oudenaarden, A. & Tyagi, S. Imaging individual mRNA molecules using multiple singly labeled probes. *Nat. Methods* **5**, 877-879, doi:10.1038/nmeth.1253 (2008).
- 15 Guo, M. T., Rotem, A., Heyman, J. A. & Weitz, D. A. Droplet microfluidics for high-throughput biological assays. *Lab on a Chip* **12**, 2146-2155 (2012).
- 16 Streets, A. M. *et al.* Microfluidic single-cell whole-transcriptome sequencing. *Proceedings of the National Academy of Sciences* **111**, 7048-7053 (2014).
- 17 Wu, A. R. *et al.* Quantitative assessment of single-cell RNA-sequencing methods. *Nature methods* **11**, 41 (2014).
- 18 Lécuyer, E. *et al.* Global analysis of mRNA localization reveals a prominent role in organizing cellular architecture and function. *Cell* **131**, 174-187 (2007).
- 19 Femino, A. M., Fay, F. S., Fogarty, K. & Singer, R. H. Visualization of single RNA transcripts in situ. *Science* **280**, 585-590 (1998).
- 20 Maamar, H., Raj, A. & Dubnau, D. Noise in gene expression determines cell fate in *Bacillus subtilis*. *Science* **317**, 526-529 (2007).

- 21 Levsky, J. M., Shenoy, S. M., Pezo, R. C. & Singer, R. H. Single-cell gene expression profiling. *Science* **297**, 836-840 (2002).
- 22 Lubeck, E. & Cai, L. Single-cell systems biology by super-resolution imaging and combinatorial labeling. *Nature methods* **9**, 743 (2012).
- 23 Lubeck, E., Coskun, A. F., Zhiyentayev, T., Ahmad, M. & Cai, L. Single-cell in situ RNA profiling by sequential hybridization. *Nature methods* **11**, 360 (2014).
- 24 Levsky, J. M. & Singer, R. H. Fluorescence in situ hybridization: past, present and future. *Journal of cell science* **116**, 2833-2838 (2003).
- 25 Chen, K. H., Boettiger, A. N., Moffitt, J. R., Wang, S. & Zhuang, X. Spatially resolved, highly multiplexed RNA profiling in single cells. *Science* **348**, aaa6090 (2015).
- 26 Abrahamsson, S. *et al.* Fast multicolor 3D imaging using aberration-corrected multifocus microscopy. *Nature methods* **10**, 60 (2013).
- 27 Basiji, D. A., Ortyn, W. E., Liang, L., Venkatachalam, V. & Morrissey, P. Cellular image analysis and imaging by flow cytometry. *Clin. Lab. Med.* **27**, 653-670, (2007).
- 28 Han, Y. Y., Gu, Y., Zhang, A. C. & Lo, Y. H. Review: imaging technologies for flow cytometry. *Lab Chip* **16**, 4639-4647 (2016).
- 29 Mertz, J. Strategies for volumetric imaging with a fluorescence microscope. *Optica* **6**, 1261-1268 (2019).
- 30 Tang, J., Ren, J. & Han, K. Y. Fluorescence imaging with tailored light. *Nanophotonics* **8**, 2111-2128 (2019).
- 31 Blanchard, P. M. & Greenaway, A. H. Simultaneous multiplane imaging with a distorted diffraction grating. *Applied optics* **38**, 6692-6699 (1999).

- 32 Hajj, B. *et al.* Whole-cell, multicolor superresolution imaging using volumetric multifocus microscopy. *Proceedings of the National Academy of Sciences* **111**, 17480-17485 (2014).
- 33 Duocastella, M. *et al.* Fast inertia-free volumetric light-sheet microscope. *ACS Photonics* **4**, 1797-1804 (2017).
- 34 Kong, L. *et al.* Continuous volumetric imaging via an optical phase-locked ultrasound lens. *Nat. Methods* **12**, 759-762 (2015).
- 35 Botcherby, E. J., Booth, M. J., Juskaitis, R. & Wilson, T. Real-time extended depth of field microscopy. *Opt. Express* **16**, 21843-21848 (2008).
- 36 Shain, W. J., Vickers, N. A., Goldberg, B. B., Bifano, T. & Mertz, J. Extended depth-of-field microscopy with a high-speed deformable mirror. *Opt. Lett.* **42**, 995-998 (2017).
- 37 Žurauskas, M., Barnstedt, O., Frade-Rodriguez, M., Waddell, S. & Booth, M. J. Rapid adaptive remote focusing microscope for sensing of volumetric neural activity. *Biomed. Opt. Express* **8**, 4369-4379 (2017).
- 38 Dowski, E. R. & Cathey, W. T. Extended depth of field through wave-front coding. *Applied optics* **34**, 1859-1866 (1995).
- 39 Ojeda-Castaneda, J. & Gomez-Sarabia, C. M. Tuning field depth at high resolution by pupil engineering. *Adv. Opt. Photonics* **7**, 814-880 (2015).
- 40 Palillero-Sandoval, O., Aguilar, J. F. & Berriel-Valdos, L. R. Phase mask coded with the superposition of four Zernike polynomials for extending the depth of field in an imaging system. *Applied optics* **53**, 4033-4038 (2014).
- 41 Cai, B. *et al.* Optical volumetric projection for fast 3D imaging through circularly symmetric pupil engineering. *Biomedical optics express* **9**, 437-446 (2018).

- 42 Zhou, F., Ye, R., Li, G., Zhang, H. & Wang, D. Optimized circularly symmetric phase mask to extend the depth of focus. *JOSA A* **26**, 1889-1895 (2009).
- 43 Tomer, R. *et al.* SPED light sheet microscopy: fast mapping of biological system structure and function. *Cell* **163**, 1796-1806 (2015).
- 44 Meng, Q., Xu, T., Smith, Z. J. & Chu, K. Optical volumetric projection with large NA objectives for fast high-resolution 3D imaging of neural signals. *Biomedical Optics Express* **11**, 3769-3782 (2020).
- 45 Quirin, S., Peterka, D. S. & Yuste, R. Instantaneous three-dimensional sensing using spatial light modulator illumination with extended depth of field imaging. *Optics express* **21**, 16007-16021 (2013).
- 46 Izeddin, I. *et al.* PSF shaping using adaptive optics for three-dimensional single-molecule super-resolution imaging and tracking. *Optics express* **20**, 4957-4967 (2012).
- 47 Pavani, S. R. P. *et al.* Three-dimensional, single-molecule fluorescence imaging beyond the diffraction limit by using a double-helix point spread function. *Proceedings of the National Academy of Sciences* **106**, 2995-2999 (2009).
- 48 Lee, J. H., Uhm, T. K., Lee, W. S. & Youn, S. K. 757-764 (International Society for Optics and Photonics).
- 49 Kner, P., Sedat, J. W., Agard, D. A. & Kam, Z. High-resolution wide-field microscopy with adaptive optics for spherical aberration correction and motionless focusing. *Journal of microscopy* **237**, 136-147 (2010).

- 50 Vermeulen, P., Muro, E., Pons, T., Loriette, V. & Fragola, A. Adaptive optics for fluorescence wide-field microscopy using spectrally independent guide star and markers. *Journal of Biomedical Optics* **16**, 076019 (2011).
- 51 Lenz, M. O. *et al.* (Wiley Online Library, 2014).
- 52 Zhu, G., Chen, Y., Liu, Y., Zhang, Y. & Yu, S. Characterizing a 14×14 OAM mode transfer matrix of a ring-core fiber based on quadrature phase-shift interference. *Optics letters* **42**, 1257-1260 (2017).
- 53 Liu, J. & Wang, J. Demonstration of polarization-insensitive spatial light modulation using a single polarization-sensitive spatial light modulator. *Scientific reports* **5**, 1-7 (2015).
- 54 Fickler, R. *et al.* Quantum entanglement of high angular momenta. *Science* **338**, 640-643 (2012).
- 55 Velasco, M. G. M. *et al.* 3D super-resolution deep-tissue imaging in living mice. *bioRxiv*, 790212 (2019).
- 56 Shechtman, Y., Sahl, S. J., Backer, A. S. & Moerner, W. E. Optimal point spread function design for 3D imaging. *Physical review letters* **113**, 133902 (2014).
- 57 Pavani, S. R. P., DeLuca, J. G. & Piestun, R. Polarization sensitive, three-dimensional, single-molecule imaging of cells with a double-helix system. *Optics express* **17**, 19644-19655 (2009).
- 58 Backlund, M. P. *et al.* Simultaneous, accurate measurement of the 3D position and orientation of single molecules. *Proceedings of the National Academy of Sciences* **109**, 19087-19092 (2012).

- 59 Moffitt, J. R. *et al.* High-performance multiplexed fluorescence in situ hybridization in culture and tissue with matrix imprinting and clearing. *Proc. Natl. Acad. Sci. U.S.A.* **113**, 14456-14461 (2016).
- 60 Kishi, J. Y. *et al.* SABER amplifies FISH: enhanced multiplexed imaging of RNA and DNA in cells and tissues. *Nat. Methods* **16**, 533-544 (2019).
- 61 Richardson, D. S. & Lichtman, J. W. Clarifying tissue clearing. *Cell* **162**, 246-257 (2015).
- 62 Dunsby, C. Optically sectioned imaging by oblique plane microscopy. *Optics express* **16**, 20306-20316 (2008).
- 63 Tang, J. & Han, K. Y. Extended field-of-view single-molecule imaging by highly inclined swept illumination. *Optica* **5**, 1063-1069 (2018).
- 64 Fornasiero, E. F. & Opazo, F. Super - resolution imaging for cell biologists: Concepts, applications, current challenges and developments. *Bioessays* **37**, 436-451 (2015).
- 65 Dempsey, G. T., Vaughan, J. C., Chen, K. H., Bates, M. & Zhuang, X. Evaluation of fluorophores for optimal performance in localization-based super-resolution imaging. *Nature methods* **8**, 1027 (2011).
- 66 van de Linde, S., Wolter, S., Heilemann, M. & Sauer, M. The effect of photoswitching kinetics and labeling densities on super-resolution fluorescence imaging. *Journal of biotechnology* **149**, 260-266 (2010).
- 67 Dempsey, G. T. *et al.* Photoswitching mechanism of cyanine dyes. *Journal of the American Chemical Society* **131**, 18192-18193 (2009).
- 68 Huang, B., Wang, W., Bates, M. & Zhuang, X. Three-dimensional super-resolution imaging by stochastic optical reconstruction microscopy. *Science* **319**, 810-813 (2008).

- 69 Jia, S., Vaughan, J. C. & Zhuang, X. Isotropic three-dimensional super-resolution imaging with a self-bending point spread function. *Nature photonics* **8**, 302-306 (2014).
- 70 Lew, M. D., Lee, S. F., Badieirostami, M. & Moerner, W. E. Corkscrew point spread function for far-field three-dimensional nanoscale localization of pointlike objects. *Optics letters* **36**, 202-204 (2011).
- 71 Ojeda-Castañeda, J. & Gómez-Sarabia, C. M. Tuning field depth at high resolution by pupil engineering. *Advances in Optics and Photonics* **7**, 814-880 (2015).
- 72 Sheppard, C. J. R. & Hegedus, Z. S. Axial behavior of pupil-plane filters. *JOSA A* **5**, 643-647 (1988).
- 73 Gu, M. *Advanced optical imaging theory*. Vol. 75 (Springer Science & Business Media, 2000).
- 74 Hao, X., Kuang, C., Wang, T. & Liu, X. Effects of polarization on the de-excitation dark focal spot in STED microscopy. *Journal of Optics* **12**, 115707 (2010).
- 75 Liu, Z., Flores, A., Wang, M. R. & Yang, J. J. Diffractive infrared lens with extended depth of focus. *Optical Engineering* **46**, 018002 (2007).
- 76 Sochacki, J., Bara, S., Jaroszewicz, Z. & Kołodziejczyk, A. Phase retardation of the uniform-intensity axilens. *Optics letters* **17**, 7-9 (1992).
- 77 Zalvidea, D. & Siqueira, E. E. Phase pupil functions for focal-depth enhancement derived from a Wigner distribution function. *Applied optics* **37**, 3623-3627 (1998).
- 78 Ojeda-Castañeda, J., Andres, P. & Diaz, A. Annular apodizers for low sensitivity to defocus and to spherical aberration. *Opt. Lett.* **11**, 487-489 (1986).
- 79 Ryu, S. & Joo, C. Design of binary phase filters for depth-of-focus extension via binarization of axisymmetric aberrations. *Optics express* **25**, 30312-30326 (2017).

- 80 Abrahamsson, S., Usawa, S. & Gustafsson, M. 60900N (International Society for Optics and Photonics).
- 81 Khaw, I. *et al.* Flat-field illumination for quantitative fluorescence imaging. *Optics express* **26**, 15276-15288 (2018).
- 82 Siviloglou, G. A., Broky, J., Dogariu, A. & Christodoulides, D. N. Observation of accelerating Airy beams. *Physical Review Letters* **99**, 213901 (2007).
- 83 Jia, S., Vaughan, J. C. & Zhuang, X. Isotropic three-dimensional super-resolution imaging with a self-bending point spread function. *Nature photonics* **8**, 302 (2014).
- 84 Pegoraro, G. & Misteli, T. High-throughput imaging for the discovery of cellular mechanisms of disease. *Trends Genet.* **33**, 604-615 (2017).
- 85 Usaj, M. M. *et al.* High-content screening for quantitative cell biology. *Trends Cell Biol.* **26**, 598-611 (2016).
- 86 Muzzey, D. & van Oudenaarden, A. Quantitative time-lapse fluorescence microscopy in single cells. *Annu. Rev. Cell Dev. Biol.* **25**, 301-327 (2009).
- 87 Sigal, A. *et al.* Dynamic proteomics in individual human cells uncovers widespread cell-cycle dependence of nuclear proteins. *Nat. Methods* **3**, 525-531 (2006).
- 88 Lundberg, E. & Borner, G. H. H. Spatial proteomics: a powerful discovery tool for cell biology. *Nat. Rev. Mol. Cell Biol.* **20**, 285-302 (2019).
- 89 Thul, P. J. *et al.* A subcellular map of the human proteome. *Science* **356**, eaal3321 (2017).
- 90 Lein, E., Borm, L. E. & Linnarsson, S. The promise of spatial transcriptomics for neuroscience in the era of molecular cell typing. *Science* **358**, 64 (2017).

- 91 Rimón, N. & Schuldiner, M. Getting the whole picture: combining throughput with content in microscopy. *J. Cell Sci.* **124**, 3743-3751 (2011).
- 92 Ma, H. & Liu, Y. Super-resolution localization microscopy: Toward high throughput, high quality, and low cost. *APL Photonics* **5**, 060902 (2020).
- 93 Tanaka, N. *et al.* Whole-tissue biopsy phenotyping of three-dimensional tumours reveals patterns of cancer heterogeneity. *Nat. Biomed. Eng.* **1**, 796-806 (2017).
- 94 Femino, A., Fay, F. S., Fogarty, K. & Singer, R. H. Visualization of single RNA transcripts in situ. *Science* **280**, 585-590 (1998).
- 95 Barteneva, N. S., Fasler-Kan, E. & Vorobjev, I. A. Imaging flow cytometry: coping with heterogeneity in biological systems. *J. Histochem. Cytochem.* **60**, 723-733, (2012).
- 96 Fahrbach, F. O., Voigt, F. F., Schmid, B., Helmchen, F. & Huisken, J. Rapid 3D light-sheet microscopy with a tunable lens. *Opt. Express* **21**, 21010-21026 (2013).
- 97 Abrahamsson, S. *et al.* Fast multicolor 3D imaging using aberration-corrected multifocus microscopy. *Nat. Methods* **10**, 60-63 (2013).
- 98 Prevedel, R. *et al.* Simultaneous whole-animal 3D imaging of neuronal activity using light-field microscopy. *Nat. Methods* **11**, 727-730 (2014).
- 99 Padovan-Merhar, O. *et al.* Single mammalian cells compensate for differences in cellular volume and DNA copy number through independent global transcriptional mechanisms. *Mol. Cell* **58**, 339-352 (2015).
- 100 Tang, J., Sun, Y., Pang, S. & Han, K. Y. Spatially encoded fast single-molecule fluorescence spectroscopy with full field-of-view. *Scientific reports* **7**, 1-6 (2017).

- 101 Weigert, M. *et al.* Content-aware image restoration: pushing the limits of fluorescence microscopy. *Nat. Methods* **15**, 1090-1097 (2018).
- 102 Mandracchia, B. *et al.* Fast and accurate sCMOS noise correction for fluorescence microscopy. *Nat. Comm.* **11**, 94 (2020).
- 103 Levesque, M. J. & Raj, A. Single-chromosome transcriptional profiling reveals chromosomal gene expression regulation. *Nature methods* **10**, 246 (2013).
- 104 Xia, C., Fan, J., Emanuel, G., Hao, J. & Zhuang, X. Spatial transcriptome profiling by MERFISH reveals subcellular RNA compartmentalization and cell cycle-dependent gene expression. *Proceedings of the National Academy of Sciences* **116**, 19490-19499 (2019).
- 105 Hu, C.-D. & Kerppola, T. K. Simultaneous visualization of multiple protein interactions in living cells using multicolor fluorescence complementation analysis. *Nature biotechnology* **21**, 539-545 (2003).
- 106 Huang, B., Bates, M. & Zhuang, X. Super-resolution fluorescence microscopy. *Annual review of biochemistry* **78**, 993-1016 (2009).
- 107 Bates, M., Huang, B., Dempsey, G. T. & Zhuang, X. Multicolor super-resolution imaging with photo-switchable fluorescent probes. *Science* **317**, 1749-1753 (2007).
- 108 Huang, B., Jones, S. A., Brandenburg, B. & Zhuang, X. Whole-cell 3D STORM reveals interactions between cellular structures with nanometer-scale resolution. *Nature methods* **5**, 1047 (2008).
- 109 Markwirth, A. *et al.* Video-rate multi-color structured illumination microscopy with simultaneous real-time reconstruction. *Nature communications* **10**, 1-11 (2019).

- 110 Miller, D. M. & Shakes, D. C. Immunofluorescence microscopy. *Methods in cell biology* **48**, 365-395 (1995).
- 111 Shihavuddin, A. *et al.* Smooth 2D manifold extraction from 3D image stack. *Nat. Comm.* **8**, 15554 (2017).
- 112 Sarder, P. & Nehorai, A. Deconvolution methods for 3-D fluorescence microscopy images. *IEEE Signal Processing Magazine* **23**, 32-45 (2006).
- 113 Gustafsson, N. *et al.* Fast live-cell conventional fluorophore nanoscopy with ImageJ through super-resolution radial fluctuations. *Nature communications* **7**, 1-9 (2016).
- 114 Dertinger, T., Colyer, R., Iyer, G., Weiss, S. & Enderlein, J. Fast, background-free, 3D super-resolution optical fluctuation imaging (SOFI). *Proceedings of the National Academy of Sciences* **106**, 22287-22292 (2009).
- 115 Hain, R., Kähler, C. J. & Tropea, C. Comparison of CCD, CMOS and intensified cameras. *Experiments in fluids* **42**, 403-411 (2007).
- 116 Huang, F. *et al.* Video-rate nanoscopy using sCMOS camera-specific single-molecule localization algorithms. *Nature methods* **10**, 653-658 (2013).
- 117 Carlton, P. M. *et al.* Fast live simultaneous multiwavelength four-dimensional optical microscopy. *Proceedings of the National Academy of Sciences* **107**, 16016-16022 (2010).
- 118 Gustafsson, N. *et al.* Fast live-cell conventional fluorophore nanoscopy with ImageJ through super-resolution radial fluctuations. *Nat. Comm.* **7**, 12471, doi:10.1038/ncomms12471 (2016).
- 119 Schwertner, M., Booth, M. J., Neil, M. A. A. & Wilson, T. Measurement of specimen-induced aberrations of biological samples using phase stepping interferometry. *Journal of microscopy* **213**, 11-19 (2004).

- 120 Urban, N. T., Willig, K. I., Hell, S. W. & Nägerl, U. V. STED nanoscopy of actin dynamics in synapses deep inside living brain slices. *Biophysical journal* **101**, 1277-1284 (2011).
- 121 Heine, J. *et al.* Three dimensional live-cell STED microscopy at increased depth using a water immersion objective. *Review of Scientific Instruments* **89**, 053701 (2018).
- 122 Ren, J. & Han, K. Y. 2.5 D Microscopy: Fast, High-Throughput Imaging via Volumetric Projection for Quantitative Subcellular Analysis. *ACS Photonics* (2021).
- 123 Azucena, O. *et al.* Adaptive optics wide-field microscopy using direct wavefront sensing. *Optics letters* **36**, 825-827 (2011).
- 124 Vettenburg, T. *et al.* Light-sheet microscopy using an Airy beam. *Nature methods* **11**, 541-544 (2014).
- 125 Keller, P. J., Schmidt, A. D., Wittbrodt, J. & Stelzer, E. H. K. Reconstruction of zebrafish early embryonic development by scanned light sheet microscopy. *science* **322**, 1065-1069 (2008).
- 126 Huiskens, J., Swoger, J., Del Bene, F., Wittbrodt, J. & Stelzer, E. H. K. Optical sectioning deep inside live embryos by selective plane illumination microscopy. *Science* **305**, 1007-1009 (2004).
- 127 Chen, B.-C. *et al.* Lattice light-sheet microscopy: imaging molecules to embryos at high spatiotemporal resolution. *Science* **346** (2014).
- 128 Chang, B.-J. *et al.* Universal light-sheet generation with field synthesis. *Nature methods* **16**, 235-238 (2019).
- 129 Evanko, D. Hybridization chain reaction. *Nature Methods* **1**, 186 (2004).

- 130 Sigal, Y. M., Zhou, R. & Zhuang, X. Visualizing and discovering cellular structures with super-resolution microscopy. *Science* **361**, 880-887 (2018).
- 131 Kourkoutis, L. F., Plitzko, J. M. & Baumeister, W. Electron microscopy of biological materials at the nanometer scale. *Annual review of materials research* **42**, 33-58 (2012).
- 132 Thompson, R. F., Walker, M., Siebert, C. A., Muench, S. P. & Ranson, N. A. An introduction to sample preparation and imaging by cryo-electron microscopy for structural biology. *Methods* **100**, 3-15 (2016).
- 133 Hell, S. W. & Wichmann, J. Breaking the diffraction resolution limit by stimulated emission: stimulated-emission-depletion fluorescence microscopy. *Optics letters* **19**, 780-782 (1994).
- 134 Vicidomini, G., Bianchini, P. & Diaspro, A. STED super-resolved microscopy. *Nature methods* **15**, 173 (2018).
- 135 Gustafsson, M. G. L. Surpassing the lateral resolution limit by a factor of two using structured illumination microscopy. *Journal of microscopy* **198**, 82-87 (2000).
- 136 Gustafsson, M. G. L. Nonlinear structured-illumination microscopy: wide-field fluorescence imaging with theoretically unlimited resolution. *Proceedings of the National Academy of Sciences* **102**, 13081-13086 (2005).
- 137 Betzig, E. *et al.* Imaging intracellular fluorescent proteins at nanometer resolution. *Science* **313**, 1642-1645 (2006).
- 138 Hess, S. T., Girirajan, T. P. K. & Mason, M. D. Ultra-high resolution imaging by fluorescence photoactivation localization microscopy. *Biophysical journal* **91**, 4258-4272 (2006).
- 139 Rust, M. J., Bates, M. & Zhuang, X. Sub-diffraction-limit imaging by stochastic optical reconstruction microscopy (STORM). *Nature methods* **3**, 793-796 (2006).

- 140 Heilemann, M. *et al.* Subdiffraction - resolution fluorescence imaging with conventional fluorescent probes. *Angewandte Chemie International Edition* **47**, 6172-6176 (2008).
- 141 Thompson, R. E., Larson, D. R. & Webb, W. W. Precise nanometer localization analysis for individual fluorescent probes. *Biophysical journal* **82**, 2775-2783 (2002).
- 142 Shaner, N. C. *et al.* Improving the photostability of bright monomeric orange and red fluorescent proteins. *Nature methods* **5**, 545 (2008).
- 143 Gould, T. J., Verkhusha, V. V. & Hess, S. T. Imaging biological structures with fluorescence photoactivation localization microscopy. *Nature protocols* **4**, 291 (2009).
- 144 Shroff, H., Galbraith, C. G., Galbraith, J. A. & Betzig, E. Live-cell photoactivated localization microscopy of nanoscale adhesion dynamics. *Nature methods* **5**, 417-423 (2008).
- 145 Wolter, S. *et al.* Real-time computation of subdiffraction-resolution fluorescence images. *Journal of microscopy* **237**, 12-22 (2010).
- 146 Van de Linde, S. *et al.* Direct stochastic optical reconstruction microscopy with standard fluorescent probes. *Nature protocols* **6**, 991 (2011).
- 147 von Diezmann, A., Shechtman, Y. & Moerner, W. E. Three-dimensional localization of single molecules for super-resolution imaging and single-particle tracking. *Chemical reviews* **117**, 7244-7275 (2017).
- 148 Pavani, S. R. P. & Piestun, R. High-efficiency rotating point spread functions. *Optics express* **16**, 3484-3489 (2008).
- 149 Prasad, S. Rotating point spread function via pupil-phase engineering. *Optics letters* **38**, 585-587 (2013).

- 150 Wang, Z. *et al.* Single shot, three-dimensional fluorescence microscopy with a spatially rotating point spread function. *Biomedical optics express* **8**, 5493-5506 (2017).
- 151 Lee, H.-l. D., Sahl, S. J., Lew, M. D. & Moerner, W. E. The double-helix microscope super-resolves extended biological structures by localizing single blinking molecules in three dimensions with nanoscale precision. *Applied physics letters* **100**, 153701 (2012).
- 152 Heilemann, M., van de Linde, S., Mukherjee, A. & Sauer, M. Super-resolution imaging with small organic fluorophores. *Angewandte Chemie International Edition* **48**, 6903-6908 (2009).
- 153 van de Linde, S., Sauer, M. & Heilemann, M. Subdiffraction-resolution fluorescence imaging of proteins in the mitochondrial inner membrane with photoswitchable fluorophores. *Journal of structural biology* **164**, 250-254 (2008).
- 154 Vogelsang, J., Cordes, T., Forthmann, C., Steinhauer, C. & Tinnefeld, P. Controlling the fluorescence of ordinary oxazine dyes for single-molecule switching and superresolution microscopy. *Proceedings of the National Academy of Sciences* **106**, 8107-8112 (2009).
- 155 Tang, J., Sun, Y., Pang, S. & Han, K. Y. Spatially encoded fast single-molecule fluorescence spectroscopy with full field-of-view. *Sci. Rep.* **7**, 10945, doi:10.1038/s41598-017-10837-6 (2017).